TÉCNICO LISBOA

Experimental and computational evaluation of the thermohydraulic performance of compact, gravity-driven, closed-loop thermosyphon cooling systems

Guilherme da Silveira Ribeiro Bruges Armas

Thesis to obtain the Master of Science Degree in

Chemical Engineering

Supervisors: Prof. John Richard Thome
Prof. António Luís Nobre Moreira

Examination Committee

Chairperson: Prof. Francisco Manuel da Silva Lemos

Supervisor: Prof. António Luís Nobre Moreira

Members of the committee: Prof. Miguel Abreu de Almeida Mendes

January 2021

Declaration

I declare that this document is an original work of my own authorship and that it fulfils all the requirements of the Code of Conduct and Good Practices of the Universidade de Lisboa.

Acknowledgements

I would like to thank Prof. John Thome and Dr. Jackson Marcinichen for this excellent learning, research and development opportunity, as well as all for all the support, flexibility and comprehension during the whole timeline of this work and during a time of heavy restrictions. I would also like to thank all the staff at JJ Cooling Innovation: Eng. Rémy Haynau, Eng. André Seuret and in particular Eng. Gautier Rouaze, for all the support in assembling the experimental facility and all the provided knowledge. I am also grateful for the support of Dr. Ana Moita, for all the help throughout the work and all the support during the covid-19 restrictions. A special thanks also to the PIXE lab and Dr. Gary Perrenoud for the access to the X-ray microtomography facilities.

Although not directly related to this work, I would also like to thank Prof. Carlos Henriques, Prof. Vítor Geraldes, Prof. Francisco Lemos, Prof. João Fareleira and Prof. Eduardo Filipe, for bringing me into contact with the topics of energy conversion, thermodynamics, catalysis, heat transfer and fluid flow over the last five years. I would also like to thank Prof. Dulce Simão for her support, especially in the first years of integration into university.

And finally, I would like to thank my family, as well as Catarina, Lamúria, Inês Isabel, Jarroca, Diana and Dr. Jara, people without whom it would not have been possible to get this far.

Abstract

A passive loop thermosyphon cooling system, developed by JJ Cooling Innovation, was tested at different heat loads, filling ratios and air volumetric flow rates for two low global warming potential working fluids: R1233zd(E) and R1234ze(E). The prototype, with a height of 66 mm and a 61 mm x 56 mm microchannel evaporator, was tested on a 40 mm x 40 mm copper block heated surface. The optimum charge of working fluid was found to be in the 40-60% filling ratio range. The thermosyphon was tested for R1233zd(E) and a filling ratio of 46% at heat loads from 100 W to 700 W and air volumetric flow rates from 40 CFM to 178 CFM, yielding junction temperatures between 34°C and 92°C. Another set of tests, comparing the performance of R1234ze(E), at 51% filling ratio, with R1233zd(E), at 41% filling ratio, for heat loads from 50 W to 500 W, and air volumetric flow rates from 40 CFM to 118 CFM, yielded similar junction temperatures for both fluids, between 32°C and 92°C. Thermal resistance values as low as 0.081°C/W were reached.

For several tests, a drop in performance in the left side of the device was observed, and this was confirmed by an X-ray microtomography scan to be related to partial internal blockages on that side of the device.

The cold start-up and transient behaviour of the device was also analysed, showing the overall stability of the system, except for some minor disturbances at high filling ratios and low heat loads.

Keywords: loop thermosyphon, cooling system, heat recovery, two-phase flow

Resumo

Um termossifão passivo, desenvolvido pela JJ Cooling Innovation, foi testado para diferentes cargas térmicas, cargas de fluido refrigerante e caudais volumétricos de ar, para dois fluidos com baixo potencial de aquecimento global: R1233zd(E) e R1234ze(E). O protótipo, com uma altura de 66 mm e um microevaporador com dimensões 61 mm x 56 mm, foi testado numa superfície de cobre aquecida com dimensões 40 mm x 40 mm. Várias cargas de fluido refrigerante foram testadas, com um valor óptimo na gama de 40-60%. O termossifão foi testado com R1233zd(E) e uma carga de 46%, potências entre 100 W e 700 W e caudais volumétricos de ar entre 40 CFM e 178 CFM, resultando em temperaturas de junção entre 34°C e 92°C. Testes comparando o R1234ze(E), para uma carga de 51%, com o R1233zd(E), para uma carga de 41%, para potências entre 50 W e 500 W, e caudais volumétricos de ar entre 40 CFM e 118 CFM resultaram em temperaturas de junção semelhantes, entre 32°C e 92°C. Resistências térmicas de 0.081°C/W foram atingidas..

Em vários testes, uma quebra de desempenho do lado esquerdo do protótipo foi observada, e uma microtomografia por raios-X confirmou a existência de bloqueios parciais nesse lado do termossifão.

O arranque e o comportamento transiente também foram estudados, mostrando uma elevada estabilidade, à excepção de algumas instabilidades a elevadas cargas de fluido refrigerante e baixas potências.

Palavras-chave: termossifão, sistema de arrefecimento, recuperação de calor, escoamento bifásico

Table of contents

List of tables

List of figures

List of abbreviations

CPU – central processing unit

LTS – loop thermosyphon

GDR – gravity dominant regime

FDR – friction dominant regime

CHF – critical heat flux

FR – filling ratio

MPT – multiport tube

TIM – thermal interface material

VI – virtual instrument

CFM – cubic feet per minute

DAQ – data acquisition system

TBE – evaporator base temperature

TR – thermal resistance

FS – full scale

Nomenclature

List of symbols

q – heat flow (W)

U – power supply voltage (Volt)

I – power supply current (Ampère)

$\dot{m}$ – mass flow rate (kg/s)

Q – air volumetric flow rate (m^3/s, m^3/h, CFM)

V – volume (cm^3)

m – mass (g)

A_{block} – copper block surface area (16 cm^2)

$A_{anem.}$ – anemometer cross-section area (78.5 cm^2)

k_{Cu} – copper thermal conductivity (398 $Wm^{-1}K^{-1}$)

p_{atm} – atmospheric pressure (101325 Pa)

$T_{air,in}$ – average inlet air temperature (°C)

x – vapour quality

C_p – isobaric heat capacity ($Jkg^{-1}K^{-1}$)

h_e – external heat transfer coefficient ($Wm^{-2}K^{-1}$)

h_i – internal heat transfer coefficient ($Wm^{-2}K^{-1}$)

P_{fan} – fan power (W)

v_{air} – air speed, measured by the anemometer (m/s)

h – thermosyphon height (m)

g – gravity acceleration (9.81 ms^{-2})

T – temperature (°C)

Greek letters

$\delta(t)$ – linear derivative between two points (°C/s)

ε – error, uncertainty

ΔT – temperature difference (°C)

ΔΔT – difference between temperature differences (°C)

Δt – time interval (s)

Δh_{vap} – enthalpy of vaporisation (J/kg)

ρ – density (kg/m^3)

ΔP – pressure difference, pressure drop (Pa, bar)

ΔP_{driver} – thermosyphon driving force (Pa)

Subscripts

in – inlet

out – outlet

l – liquid

g – gas

sat – saturation

mom. – momentum

cond – conduction

1. Introduction and research objectives

The use of two-phase cooling technologies, because of the high heat transfer coefficient associated with boiling/condensing flow, has been increasingly researched for high heat flux applications, such as the cooling of servers in data centres [1], fuel cells [2] or electronics on commercial aircraft [3]. These applications require the removal of large amounts of heat in an often limited space, for which two-phase cooling can be an advantage. Additionally, sustainable development goals for the next decade are an incentive for waste heat recovery, through the integration of these technologies into existing power plants and district heating networks [4]. In the case of data centres/servers, the conventional approach is direct air-cooling using fans. Due to the low heat transfer coefficient for air cooling, this approach implies high air volumetric flow rates and pressure drops, and consequently high-power consumption due to the fans. In this scope, the development of passive two-phase cooling technologies by introducing a gravity-driven thermosyphon loop together with high performance air-cooling (multiport louvered fin coil) can help mitigate these problems, by increasing the fluid-side heat transfer coefficient and hence reducing the overall footprint of the system. In the present thesis, such a new patent pending cooling unit already fabricated prior to the start of the thesis is tested.

In this context, the research objectives of the thesis are to analyse the thermal behaviour of a passive, gravity-driven loop thermosyphon (LTS) prototype over a wide range of test conditions. The post-processing and analysis of these results allowed to troubleshoot problems in the performance of the LTS, as well as to characterise the behaviour of the system in terms of response to heat load, air volumetric flow and filling ratio.

This work is organised in the following manner: a brief state-of-the-art review is presented in Chapter 2; Chapter 3 contains the description of the prototype to be tested; Chapter 4 describes the experimental procedure, assembly and post-processing; Chapter 5 shows the detailed results of the experimental campaign; Chapter 6 presents the results of a microtomography scan of the LTS, with the internal features/defects of the device; Chapter 7 concludes the thesis; Chapter 8 contains the bibliographic references; and finally, Chapter 9 contains the Appendices, including experimental data, derivations and calibration procedures.

2. State of the art review on micro two-phase cooling

The technologies that are comparable to the prototype tested in this work use closed-loop thermosyphons with heights in order of centimetres and temperatures below 100°C, specially designed for specific applications that require compact, passive cooling systems as mentioned before. These systems rely on the boiling of a fluid in an evaporator in contact with a heat source, which then rises to a condenser section where it condenses by rejecting the latent heat into a heat sink (Figure 1).

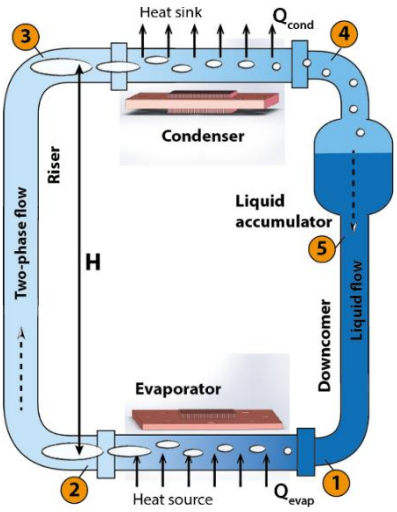

Figure 1 - Scheme of a thermosyphon closed loop (from Lamaison *et al.* (2017) *[1]*). The accumulator may or may not be necessary.

The two/phase flow inside a micro-scale system can exhibit several patterns. With increasing vapour flow rates, it starts with isolated vapour bubbles within a liquid (bubble flow), eventually coalescing into slug flow, transitioning to churn (or semi-annular) flow and, finally, annular flow, where vapour flows continuously while liquid wets the surface of the channel [2]. For (horizontal) macro-scale flow, there is an additional regime, stratified flow, that happens at low vapour and liquid flow rates [3]. Figure 2 shows the different flow regimes in micro-scale flow, as well as a map of the transitions between regimes, for different regions of mass flux (proportional to liquid flux) and vapour quality (proportional to gas flux).

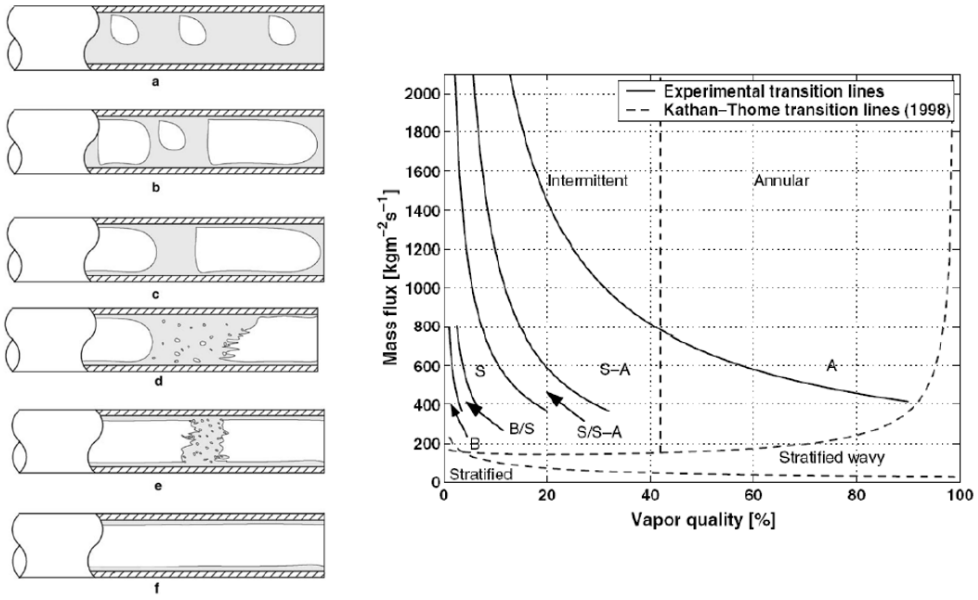

Figure 2 - Left: flow regimes for increasing gas flux: a – bubbly flow (B); b – bubbly/slug flow (B/S); c – slug flow (S); d – slug/churn flow (S/S-A); e – churn flow (S-A); f – annular flow (A). Right: map of transition lines for micro-scale (full line, Revellin *et al.* (2006) *[4]*) and macro-scale (dashed, Kattan *et al.* (1998) *[5]*) two-phase flow, for different gas and liquid velocities (vapour quality and mass flux). Adapted from Costa-Patry (2011) *[2]*.

In micro-channel boiling, if there is enough heat flux, and hence vapour flow, the liquid film in annular flow may dry-out locally, reducing the heat transfer efficiency. This means the critical heat flux (CHF) has been reached. This value can be experimentally determined, and several prediction methods have been developed for it [2].

In microchannel evaporators, the heat transfer improves with increasing heat flux for bubble/slug flow, with less influence of the mass flow rate; in the annular flow region (at higher heat loads, causing higher vapour flow rates), higher mass flow rates increase the heat transfer [6]. At the same time, Bieliński *et al.* (2011) [7] have concluded that there are two dependences of the mass flow rate on the heat flux in a loop thermosyphon: at lower heat loads, the gravity dominant regime (GDR) controls, where the mass flow rate increases with increasing heat load, because, in this region, buoyancy forces dominate and the increase in heat load vaporises more fluid and reduces the average density in the riser (*viz*. Figure 1); and the friction dominant regime (FDR) controls, where friction forces dominate and the increase in heat flux decreases the mass flow rate (Figure 3). This happens because for the GDR, where vapour quality is lower (lower heat loads), an increase in heat flux, and consequently vapour quality, causes a large increase in the void fraction, increasing buoyance at a larger pace than the increase in friction; for increases of heat flux at higher vapour qualities (FDR), the void fraction does not increase much further, and the predominant increase is the one in friction [1].

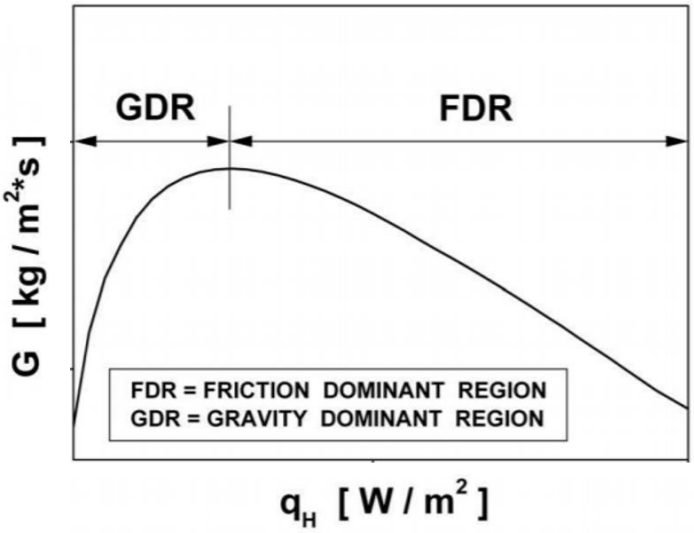

Figure 3 - Operating behaviour of a loop thermosyphon: gravity dominant regime and friction dominant regime. Adapted from Bieliński *et al.* (2011) *[7]*.

In addition, very low filling ratios can cause partial or intermittent dry-out of the evaporator (lower CHF), and very high filling ratios can cause flooding of the thermosyphon, both of which decrease heat transfer performance [6].

Work on several thermosyphon technologies has been performed over the last two decades. Manova *et al.* (2020) [8] who tested a water-cooled coaxial thermosyphon designed for the cooling of high-power electronics, consisting of a vertical 200 mm long multiport tube (MPTs) with 10 microchannels (each 0.1 mm in diameter), for filling ratios between 40 and 60% and heat flux up to 15 W/cm^2, using acetone as the working fluid. Coaxial thermosyphons, unlike the one studied in this work, consist of a single tube, with the evaporation occurring in the bottom section, the condensation in the top section, and the area between the two being adiabatic. The boiling fluid rises through the centre of the tube, with the condensate descending as a film on the walls. An evaporator wall temperature of 58.9°C was achieved for an optimum filling ratio of 50%.

Junior *et al.* (2019) [9] tested a vertical, 200 mm high, flat thermosyphon for avionics cooling that draws liquid to a lateral evaporator by capillarity using a wick (Figure 4), using water as the working fluid for heat fluxes between 0.12-2.4 W/cm^2 and filling ratios between 7.5-50%. The system had the best performance for 7.5% FR, achieving thermal resistances below 0.08°C/W and wall temperatures between 80-90°C for the higher end of heat fluxes. The low optimum FR is probably due to the capillarity-induced circulation through the wick; this device operates, to a certain degree, as a heat pipe.

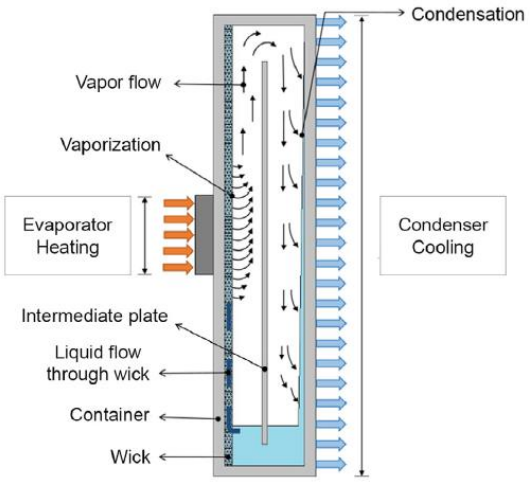

Figure 4 - Flat vertical thermosyphon for avionics cooling, laterally heated through a wick. Adapted from Junior *et al.* (2019) *[9]*.

Tests with R134a at filling ratios between 38-87% and heat fluxes between 35-400 W/cm^2 in a loop thermosyphon with a total length of 2.04 m were performed by Liu *et al.* (2018) [10]. A section of the loop was used as the evaporator. They concluded that the lowest thermal resistances (below 0.2°C/W) were observed for filling ratios between 40-60% and higher heat loads. A peak in thermal resistance was observed around 70% FR: the lower values for lower filling ratios are caused by the enhanced heat transfer resulting from the increased relevance of latent heat transfer; the decreasing values at higher filling ratios are explained by the formation of a two-phase flow continuum between the riser and evaporator. The thermal resistance also decreased with increasing heat load: due to both the mass flow and latent heat transfer increase. They also did a detailed study on the types of instabilities and performance issues for different conditions: low filling ratios, despite increased thermal performance, might exhibit transient instabilities due to localised near dry-outs in the evaporator; intermediate filling ratios, at heat fluxes high enough to generate bubbles of comparable size to the riser, but not high enough to generate a driving force to compensate the riser liquid column, cause an intermittent bubble coalescence and liquid propelling known as geyser boiling; high filling ratios, due to the low compressibility of the liquid phase, allow an increase in pressure at higher heat loads, leading to a high subcooling and dangerously high pressures. Tecchio *et al.* (2017) [11] also experimentally evaluated the phenomenon of geyser boiling in loop thermosyphons. These authors performed tests on a submerged coil evaporator and used water as a working fluid.

Garrity *et al.* (2009) [12] studied a loop thermosyphon, for use in fuel cell cooling, with heights between 0.79 and 1.33 m, using a microchannel evaporator, heat fluxes up to 7 W/cm^2 and HFE-7100 as the working fluid. They proposed an explanation for instabilities, by defining two regions: one, for low pressure drops and low vapour quality in the evaporator, where the pressure drop increases with increasing flow rate and the gravitational driving force decreases with increasing flow rate (higher mass flow implies a lower vapour quality, for the same heat load), leading to a negative feedback loop and stabilising the system; and another region, at higher evaporator pressure drops and vapour qualities, where increasing the flow rate decreases the pressure drop, causing a positive feedback either until the mass flow rate is high enough and the vapour quality low enough, and the system goes

into the stable zone again, or until circulation ceases. This difference in behaviour is mostly explained by the fact that pressure drop increases with increasing vapour quality until it reaches 60-90%, and then decreases for higher values [1].

Chauhan et al. (2019) [13] tested a microchannel evaporator thermosyphon using HFE7000 as the working fluid for the cooling of a 34.5mm x 32mm CPU surface, comparing it to commercial air-cooled and water-cooled systems. The thermosyphon was able to dissipate up to 25W/cm^2, with 36.5°C of difference between the CPU and the heat sink; the water cooler was able to cool 19W/cm^2 for a 50°C difference; and the air cooler was only able to cool 9W/cm^2 for a 52°C difference. This shows that this two-phase system has a thermal resistance an order of magnitude lower than the air-cooled system, and significantly lower than the water-cooled system.

Ohadi et al. (2012) [14] numerically simulated the cooling of 85W of power on a CPU surface using: an air-cooled system; water-cooling; single-phase (liquid) cooling using FC-72 (dielectric refrigerant); and a two-phase microchannel evaporator, using R-245fa as the working fluid. The calculated thermal resistance was again an order of magnitude lower for the two-phase microchannel evaporator when compared with air cooling (0.04°C/W vs 0.4-0.7°C/W). Liquid cooling showed intermediate values (0.1-0.2°C). For air-cooling, the air would need to enter at 5°C for appropriate cooling of the system; for water-cooling, the water would need to enter 62.4°C; for FC-72, at -4°C, due to the much lower specific heat, compared to water; the two-phase system was able to use the fluid at 76.5°C. For the two-phase system, the pumping power was 2.3mW; for the other systems, it was always above 30mW. In addition to all these advantages, this type of system also results in a much smaller footprint.

Lamaison *et al.* (2017) [1], on the other hand, have experimentally validated a simulator for a microchannel evaporator-thermosyphon system, with a height of 15 cm, for application to on-chip cooling of servers. The water-cooled system was tested at heat fluxes of 15-33 W/cm^2, a filling ratio of 67% and using R134a as the working fluid. They concluded, from simulation results, that there is a multiplicity of stationary states (mass flow rates) for the operation of the thermosyphon; this is typical of systems for which simultaneous complex energy and mass balances need to be solved, like polytropic reactors. And like in that case, only one of the stationary states is usually stable: for the ones at higher vapour qualities/lower mass flow rates, disturbances cause them to progress to a stable stationary state, as explained by Garrity *et al.* (2009) [12].

Amalfi *et al.* (2020) [15] characterized the thermal performance of a water-cooled loop thermosyphon with a total height of 70 mm and a 60 x 60 mm^2 microchannel evaporator. The device was tested on a 40 x 40 mm^2 pseudo-chip surface, for heat loads up to 200 W and using R1234ze(E) as the working fluid. It reached a maximum heater temperature of 46°C for 200 W of heat load. The thermal resistance generally decreased with increasing heat load, due to the enhanced boiling heat transfer from the increase in mass flux, vapour quality and heat flux. A minimum thermal resistance value of 0.113°C/W was reached for a heat load of 120 W. Further simulation studies were performed, and found that, in the range of tested heat loads, the mass flow rate and vapor quality increased with increasing heat load, indicating the thermosyphon was in the gravity dominant regime. They also developed a concept of several evaporators in parallel, for the cooling of multi-stage servers, with a

common riser and downcomer and a centralised condenser at the top.

3. Prototype description

The tested device is a thermosyphon, built in aluminium, with approximate external dimensions of 213 x 56 x 65 mm (Figure 5) and an internal volume of 90 cm^3. The thermosyphon was previously designed and fabricated (patent pending) by JJ Cooling Innovation for the cooling of a CPU in a data centre server.

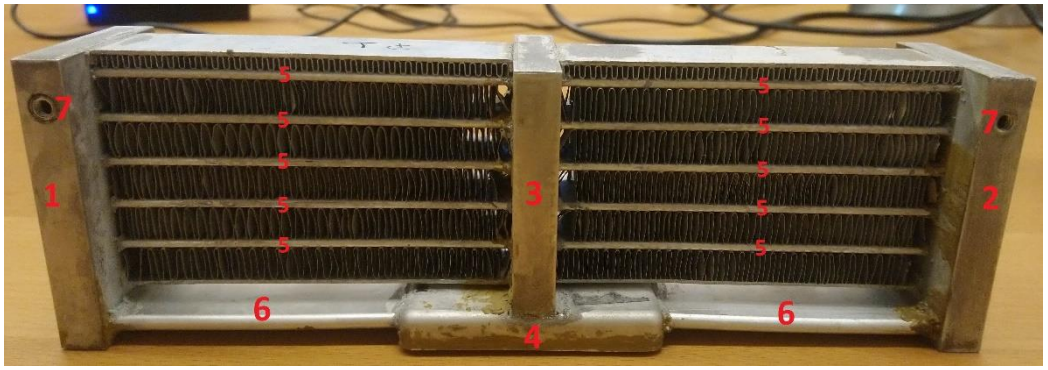

Figure 5 - Tested loop thermosyphon. 1 - Left side riser. 2 - Right side riser. 3 - Downcomer. 4 - Evaporator. 5 - Condenser multiport tubes. 6 - Horizontal multiport tube riser. 7 - Filling orifices.

The device was initially filled with a known charge of the working fluid, through one of the filling orifices (Figure 5-7). After placing the evaporator (Figure 5-4) on top of a heat source, the fluid starts to circulate in the manner shown in Figure 6.

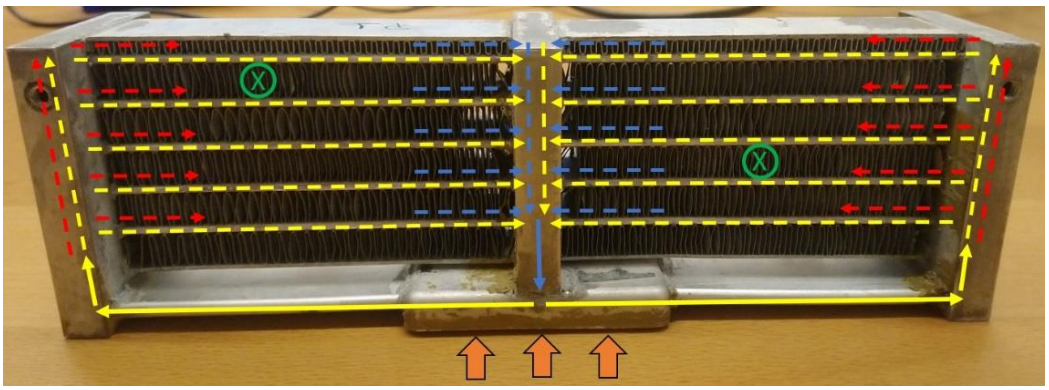

Figure 6 - Fluid flows inside the LTS. Blue - liquid flow; Yellow - two-phase flow; Red - gas flow; Green - air flow direction; Orange - heat source. Full lines correspond to certainty of the type of regime, and dashed lines correspond to the possible regimes in each zone

The fluid is partially vapourised in the evaporator, creating a two-phase flow into the risers, where it flows upwards and into the multiport tubes (MPTs) of the condenser, which are connected to louvered fins, through which the air flows to remove the latent heat generated in the evaporator. After cooling, the fluid flows into the downcomer, from where it returns, completely liquid, into the evaporator. As shown in Figure 6, there are several instances where there might either be superheated vapour or subcooled liquid. This has been experimentally demonstrated and will be shown in the next chapters.

The evaporator is comprised of 49 microchannels. This is shown in a computerised microtomography image taken from a section of the LTS containing the evaporator and the multiport tubes (Figure 7). The overall evaporator cooling zone is approximately 50 x 50 mm^2, while the total base is approximately 61 x 56 mm^2. Above, six flat condenser tubes with internal microchannels are located, separated by the louvered fins for cooling through air flow and above that a cover plate.

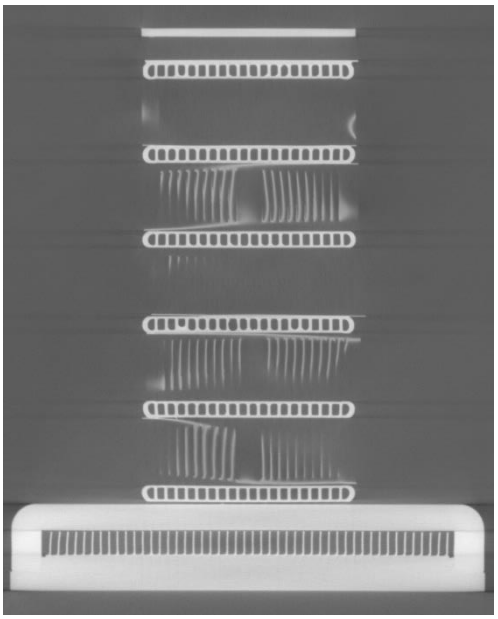

Figure 7 - Computerised microtomography image of an LTS section containing the evaporator (in the bottom) and MPTs.

4. Experimental set-up

A diagram of the experimental facility is shown in Figure 8.

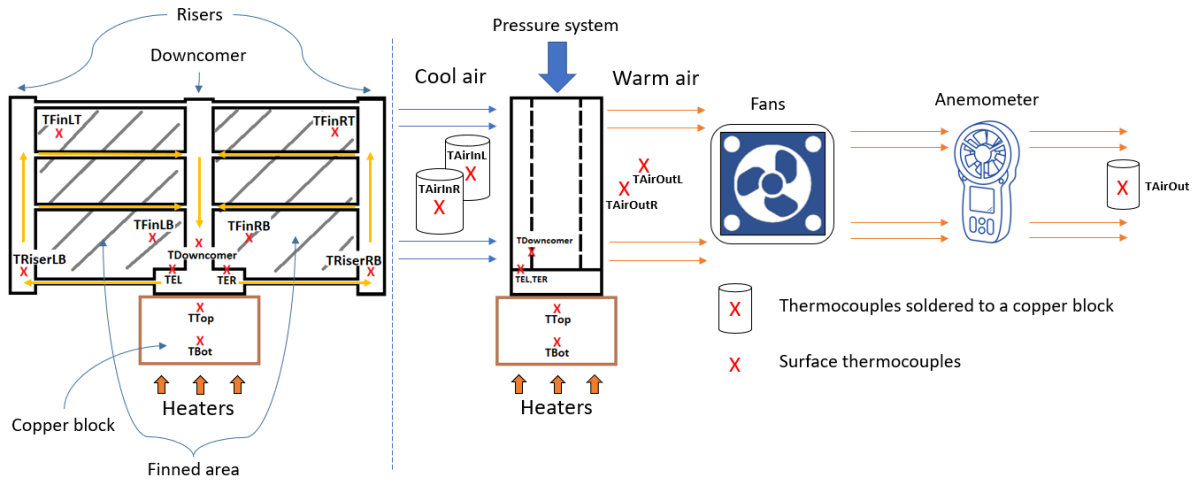

Figure 8 - Scheme of the experimental facility, showing the thermocouple locations and the fluid circulation inside the LTS.

The cooling zone base of the LTS is pressed against the copper block serving as a heat source, and the cool air flows through the louvered fins and removes the heat. The air flow is drafted through a set of fans and its mean velocity is measured by an anemometer. On top of the LTS, a pressure system applies a known imposed vertical pressure to the LTS to firmly set the thermal interface material (TIM) between the copper heating block and the evaporator of the test section.

Figure 9 shows the front view photo of the LTS, with the positions of each thermocouple and their respective label; Figure 10 shows the ducts and fans used to induce air circulation, as well as the respective thermocouple labels; Figure 11 shows the position of the anemometer at the outlet. The are thermocouples are K type: 0.5 mm thermocouples for fin temperature measurement; probe type thermocouples soldered to cylindrical copper blocks for air temperature measurement (*viz.* Figure 8); 1 mm thermocouples inserted into the heater copper block and held in place with thermal grease, as well as for the air temperature measurement in the immediate outlet of the LTS (*viz.* Figure 8); and thermocouples with adhesive tape in the remaining points of the LTS.

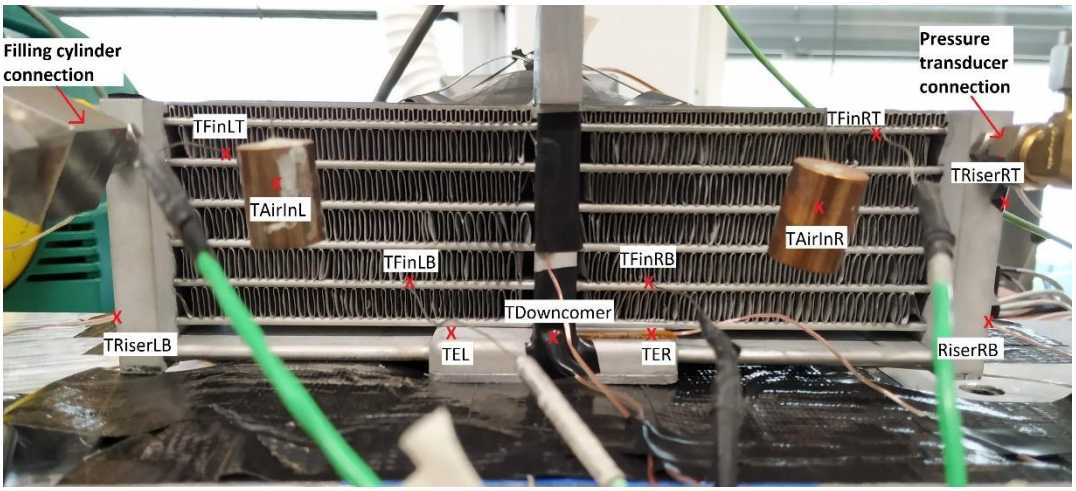

Figure 9 - Front view of the LTS, showing the thermocouple locations.

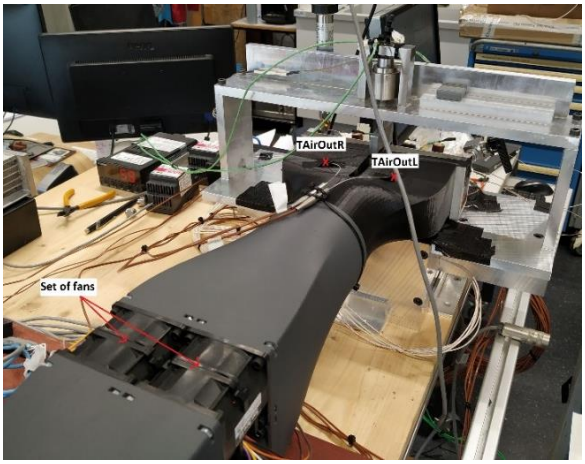

Figure 10 - Fans and duct to remove the heated air from the LTS, showing the thermocouple positions.

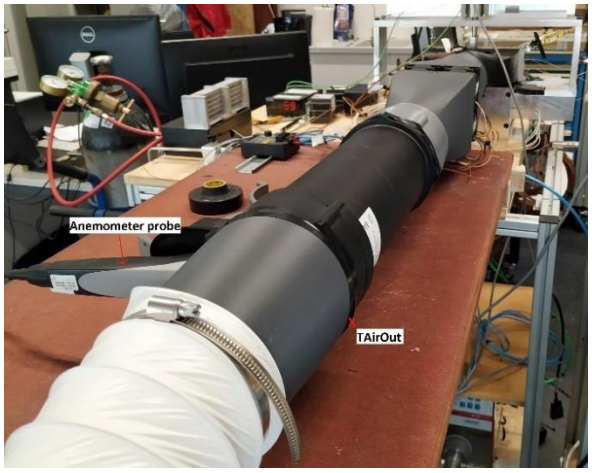

Figure 11 - Anemometer and air outlet thermocouple locations.

Table 1 lists the experimental equipment used in the measurements and testing.

Table 1 - Devices used in the experimental facility.

Power supply	Keysight N5749A
Fans	SanAce 9CRA0612P6K001
Fans' controller	SanAce 9PC8666X Series
Anemometer	Testo T480
Pressure transducers	Keller PA-33X Series

4.1 Calibration

In order to ensure accurate measurements of pressure and temperature, the thermocouples and pressure transducers were calibrated against known references. Known temperature and pressure references were plotted as a function of the output signals of the sensors, and a linear relationship between the reference and the output signal of the thermocouples/transducers was derived.

The experimental set-up, standard procedures, post-processing and results for the calibrations are described in *Appendix A – Thermocouples calibration* and *Appendix B – Pressure transducer calibration*.

4.2 Assembly

The first step in assembling the experimental facility was to prepare the copper block that serves as a base for the evaporator and mimics the CPU surface to be cooled. The copper block was inserted in a support with its base properly insulated (Figure 12-1). Six cartridge heaters were inserted into the block, in the positions shown in Figure 13. In addition, several thermocouples were inserted near the surface of the exposed section of the copper block (energy balance and temperature uniformity evaluation). Next, the remainder of the copper block was insulated (Figure 12-2), its surface covered with thermal paste (Figure 12-3), and the evaporator placed on top of it (Figure 12-4).

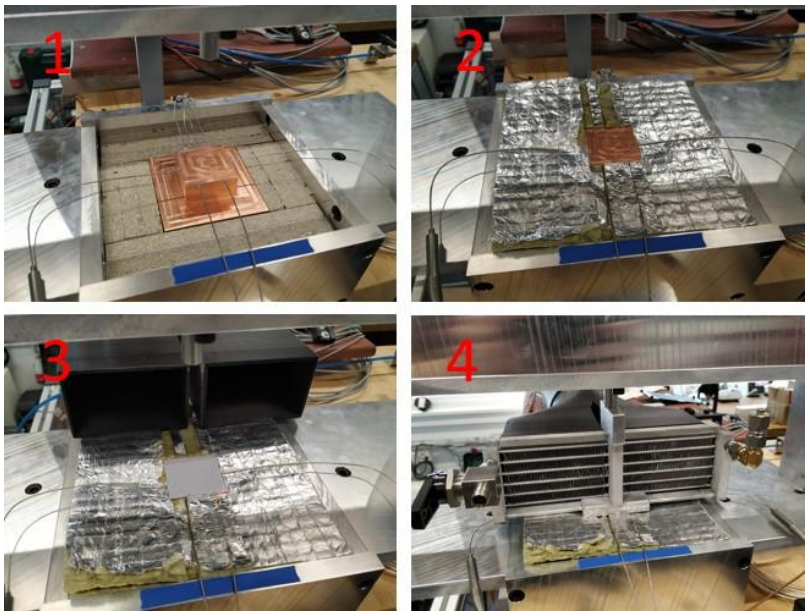

Figure 12 - Steps of the assembly of the testing facility.

Six cartridge heaters are inserted (three on each side) into the base of the copper block. On the exposed heating face (which will be in contact with the evaporator), one thermocouple is inserted on a lower level (10 mm below the surface), while the remaining are distributed closer to the surface (2 mm below it). The location of these last thermocouples in the surface of the copper block is shown in Figure 14.

The final result is a facility that consisted of the LTS sitting on the copper block, with two ducts at the outlet of the device, which are then merged into one and connected to a set of fans that supply and evacuate the heated air to/from the LTS.

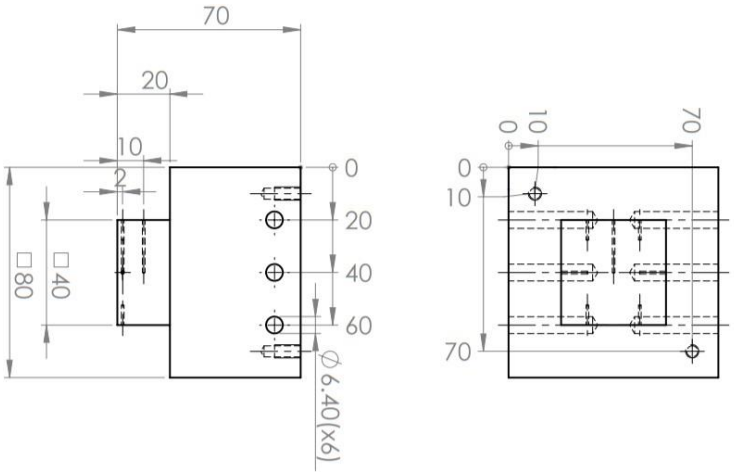

Figure 13 - Technical drawing of the copper block used for heating the LTS. Sizes are in *mm*.

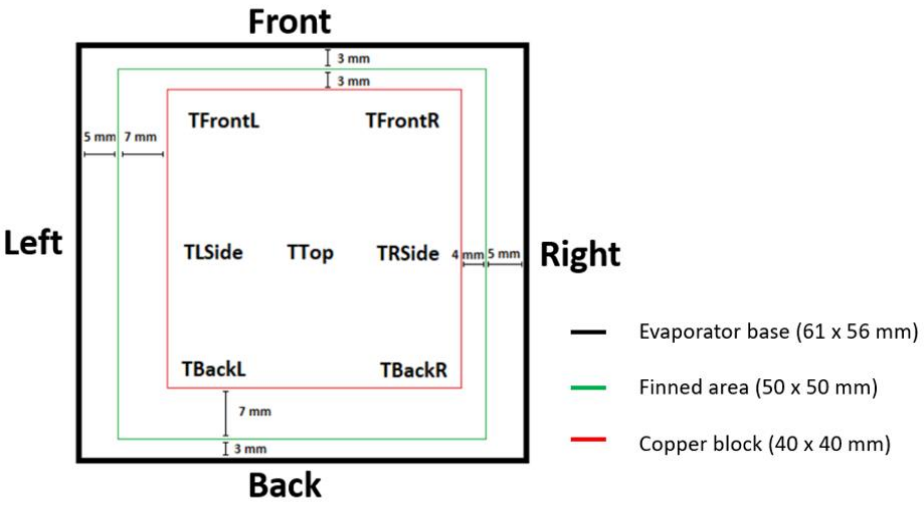

Figure 14 - Footprint of the heater copper block and internal evaporator fins on the surface of the evaporator base. The Front corresponds to the side of the copper block facing the observer in Figure 9.

4.3 Testing procedure

For each set of tests, a plan of the sequential testing conditions (air volumetric flow rate, heat load, time to reach steady-state) was defined. A plan would consist of, for example, testing heat loads from 100-500 W in increments of 100 W, for three air volumetric flow rates and running for 30 minutes for each heat load. The LabVIEW virtual instrument (VI) was programmed to automatically execute the plan remotely (by computer-control run by the experimentalist off-site or on-site) and saved all the thermocouple, pressure transducer and anemometer signals into a *csv* output file. In the case of the filling ratio analysis, the LTS was manually filled with a specific charge for each filling ratio test, and the previous procedure for the automated testing and data saving was implemented as well.

During the tests, the LabVIEW VI automatically sets the power supply voltage and current to the desired power level which controls the inlet air volumetric flow rate through real time monitoring of the outlet air volumetric flow rate and performs the back-calculation of the inlet air volumetric flow rate through the difference in air density caused by the temperature difference. The control is done by using the fans' electronic board, manipulating the output voltage.

4.4 Post-processing

The thermocouples' signals were not directly saved into the *csv* file. They were instead first automatically converted into the actual temperature values by applying the previously done thermocouples calibrations. The same was not done for the pressure transducer signal, since due to unforeseen circumstances, the pressure transducers' calibration could only be done after the full LTS testing. The real pressure values were later back-calculated. The previously described data acquisition also saved user-specified labels for each of the signals. For example, *TRiserLB* corresponded to the bottom left riser temperature (Figure 9).

After each set of tests, the saved data included all of the signals measured during the whole set of tests, as shown in Figure 15-1, for the temperature on the bottom of the downcomer (*TDowncomer*).

4.4.1 Steady state selection and refining

Since, for the most part, the relevant results correspond to the stationary states at a specified heat load and air volumetric flow rate (the "steps" shown in Figure 15-1), an automated procedure for the selection of these stationary states, as well as further post-processing calculations, was developed. This was materialised in the form of a Python script that, given a set of user parameters, automatically selected and calculated the average value of the stationary states for each recorded variable. For each of them, for example *TDowncomer* in Figure 15-1, it was done by discretising the time domain and calculating the average of said variable in each time interval. The derivative corresponding to two consecutive points was then calculated:

$$\delta(t) = \frac{T(t + \Delta t) - T(t)}{\Delta t} \quad (1)$$

The result was a set of derivative values, one for each time interval. These values were normalised to a scale of 0-100%. The derivative values as a function of time are shown in Figure 15-2. The Python script selects only the temperature values whose derivatives fall below a given threshold (in this case 5%), shown in Figure 15-3 by the red line. For the values in each stationary state, which fall below the red line threshold, only the ones marked in yellow in Figure 15-3 (the ones farthest from the edges) were considered. For each steady-state, these values were averaged and recorded in an output *csv* file.

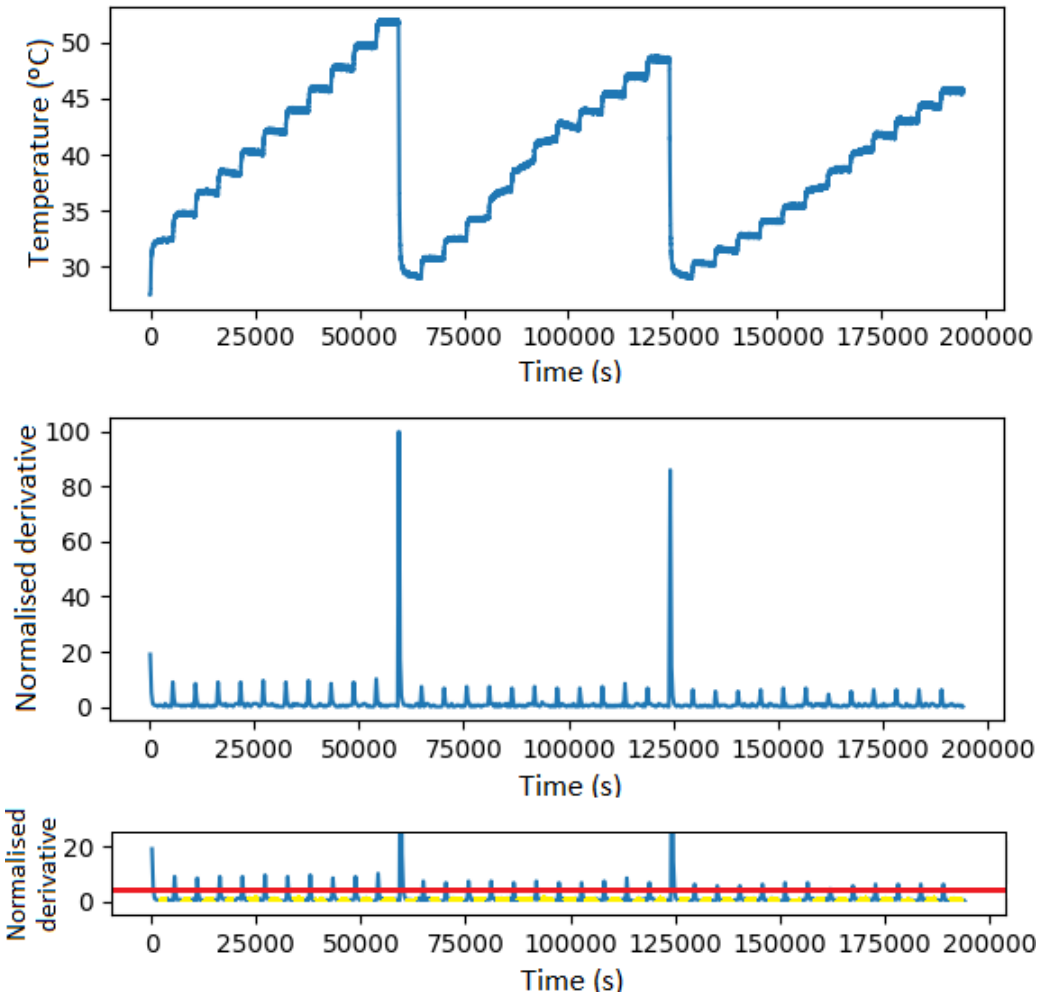

Figure 15 - (From top to bottom) 1. *TDowncomer* temperature values for the test at 46% FR with R1233zd(E). 2. Normalised derivative of said data. 3. Selection of steady states. A discretisation interval of 300 s was used.

The results shown in Figure 15 correspond to a discretisation interval of 300 s. If an interval of 50 s had been used, the result would have been the one shown in Figure 16.

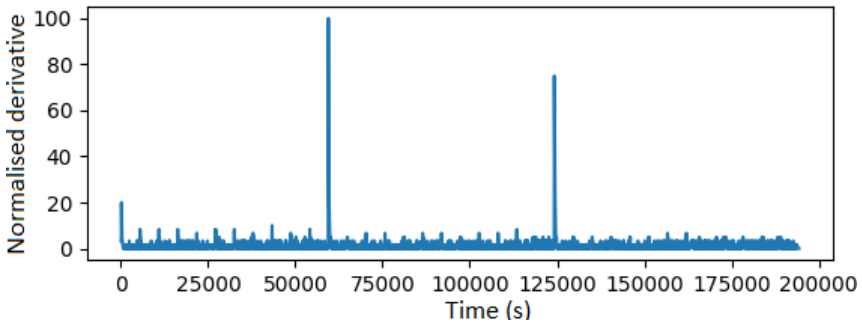

Figure 16 - *TER* temperature values for the test at 46% FR with R1233zd(E) (top). Normalised derivative of said data (bottom). A discretisation interval of 50 s was used.

In this case, it would not have been possible to select the stationary states. In order to overcome this, before running the script, the user inserts four parameters: the number of stationary states, minimum duration of each stationary state, initial value for the threshold and initial value for the

discretisation. For each variable (temperature, air speed, for example), the program tries to find the number of stationary steady-states defined by the user, lasting the minimum time defined by the user. If it is not able to do so, it updates the threshold and discretisation interval, and repeats the process until it finds the aforementioned stationary steady-states.

If in total there are 36 stationary steady-states (as in Figure 15-1), this does not mean that all processed variables will have 36 stationary states. For example, the air speed (and hence air volumetric flow rate) has only three values, and the inlet air temperature does not follow a pre-defined pattern. In this case, even after many iterations, the program is not able to find 36 distinct stationary steady-states. Instead, it selects the values occurring at the same time as the stationary steady-states found for other variables for which it was possible to find the 36 stationary steady-states. In practice, for the inlet air temperature, for example, the program would select and save 36 values, occurring at the same time as the 36 stationary steady-states already found for other previously processed variables.

In summary, in this example, the program would save 36 values for each measured variable, corresponding to the occurrence of the 36 stationary steady-states of the system. The stationary steady-state values were manually checked for several variables in each test, to ensure that the program was working correctly.

In each steady-state, there was usually a maximum oscillation of around ±0.35°C in the case of temperatures, which will be taken into account in uncertainty calculations.

4.4.2 Further calculations

In addition to automatically selecting the steady state values for all measured variables, the program also calculated other properties and results of interest, such as air volumetric flow rates, thermal resistances, heat fluxes and uncertainties, for example.

As a starting point for all the other post-processing results that will be shown throughout this work, the power supply heat load, its corresponding uncertainty, the outlet air volumetric flow rate, the inlet air volumetric flow rate and the air mass flow rate were calculated as shown below:

$$q = UI \tag{2}$$

$$\varepsilon_q^2 = U^2\varepsilon_I^2 + I^2\varepsilon_U^2 \tag{3}$$

$$Q_{out} = v_{air}A \tag{4}$$

$$Q_{in} = Q_{out}\frac{\rho_{out}(TAirOut, p_{atm})}{\rho_{in}(T_{air,in}, p_{atm})} \tag{5}$$

$$\dot{m} = Q_{out} * \rho_{out} \tag{6}$$

The accuracy for the voltage and current of the power supply are [16]:

$$\varepsilon_I = 28.5\ mA \qquad \varepsilon_U = 80\ mV$$

The inlet and outlet air densities ($\rho_{in}\ and\ \rho_{out}$) are obtained from the CoolProp database [17] assuming atmospheric pressure and the measured inlet and outlet air temperatures.

5. Results

5.1 Filling ratio analysis

The first step in the evaluation of LTS performance was to assess the influence of the filling ratio of the working fluid filling ratio. The filling ratio is defined as the ratio between the volume of fluid (in the liquid phase) and the internal volume of the LTS at 25°C:

$$FR = \frac{V_{liquid}}{V} = \frac{m}{\rho_l V} = \frac{m_l + m_g}{\rho_l V} \tag{7}$$

The LTS was filled considering a stainless steel cylinder filled properly cleaned. First, the cylinder and the LTS were emptied using a vacuum pump. Then, the cylinder was charged with the working fluid from the storage bottle. The cylinder was then connected to the LTS in order to charge it with the working fluid. In order to know the exact mass charged into the LTS, the cylinder's mass was measured before and after the charging. The measured masses for each test are listed in *Appendix E – Charges and filling ratios*.

The LTS performance was evaluated for several working fluid charges were and considering: i) constant air volumetric flow rate and varying heat loads, and ii) constant heat load and varying air volumetric flow rates. For the latter, two fluids were tested: R1233zd(E) and R1234ze(E).

5.1.1 R1233zd(E) charge determination under constant air volumetric flow rate

For the first set of tests, the LTS was charged with the R1233zd(E). Tests were for six different charges, corresponding to filling ratios of 30%, 41%, 50%, 62%, 71% and 81%. For each charge, the LTS was tested considering heat loads of 150, 300 and 500 W (heat fluxes of 9.4, 18.8 and 31.3 W/cm^2) at a constant inlet air volumetric flow rate of around 95 CFM (160 m^3/h).

At 30% FR, only a heat load of 150 W was tested. At 80% FR, the 500 W heat load was not tested. Such limitation was because the copper block temperature would exceed 100ºC, the safety limit.

The following points describe the main results obtained from this set of tests. The main test parameters are listed in Table 2.

Table 2 - Main parameters for the FR analysis for R1233zd(E) at constant inlet air volumetric flow rate.

Copper block cross-section (cm^2)	16
Filling ratio (%)	30-81
Working fluid	R1233zd(E)
Applied pressure (bar/psi)	2.4/34
Heat loads (W)	150-500
Air flow (CFM)	95
Thermal grease resistance (°C/W) [18]	0.00325
k_{Paste} (W/mK)	11
k_{Cu} (W/mK)	398
L_{Block} (mm)	2
TIM resistance (>30 psi) (°C/W)	0.00375

In the Table 2, the *Applied pressure* corresponds to the vertical applied mechanical pressure on the LTS in order to ensure proper contact of the evaporator base to the copper block, through the thermal paste.

5.1.1.1 Inlet temperature

The inlet air temperature passing through the thermosyphon fins for each filling ratio (FR), as well as the location of the thermocouples in the system, are shown in Figure 17.

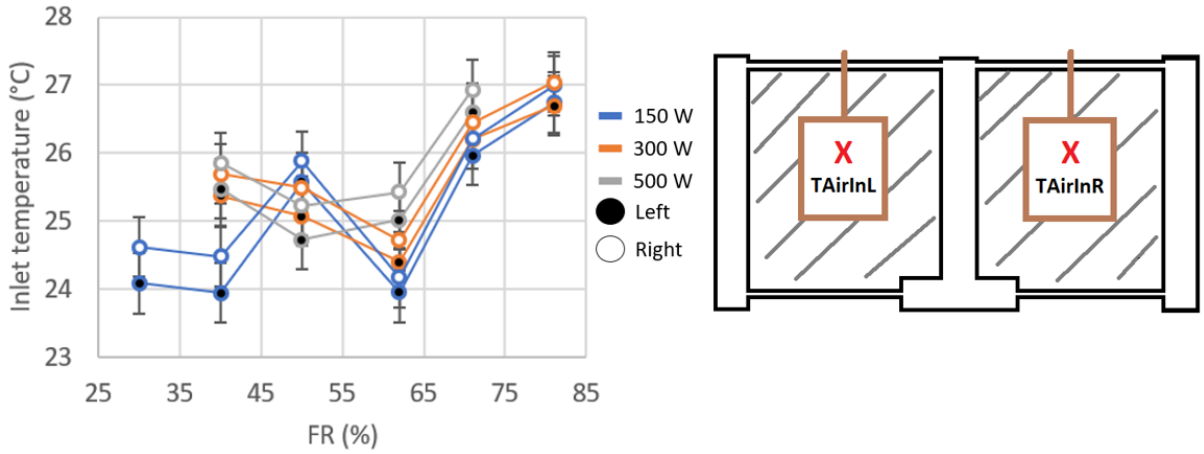

Figure 17 - Inlet air temperature for the R1233zd(E) FR analysis at 95 CFM air flow (left). Schematic of the front of the LTS showing the thermocouple locations (right).

5.1.1.2 Pressure and saturation temperature

The measured pressure, as well as the corresponding saturation temperature, are shown in Figure 18. The saturation temperature is obtained from the pressure through the working fluid vapour pressure curve in the CoolProp database [17].

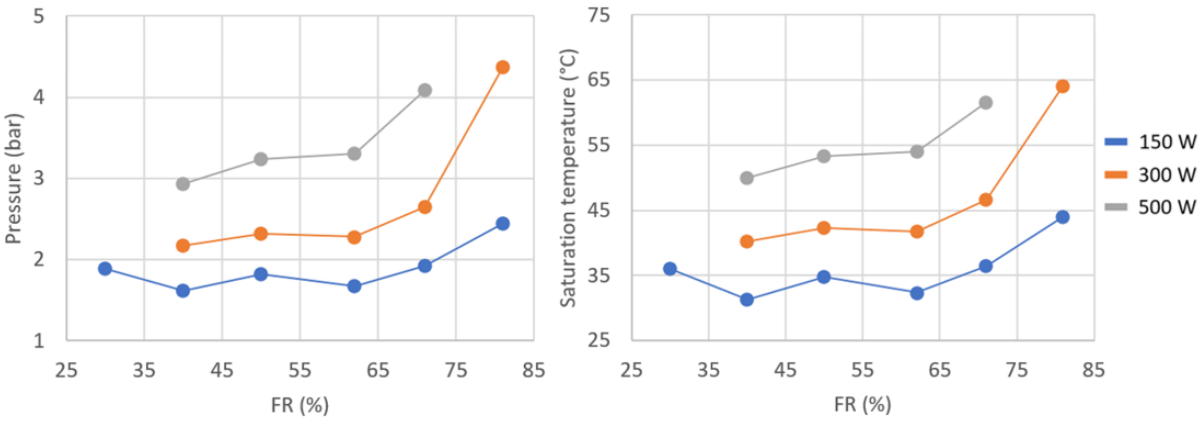

Figure 18 - Pressure and saturation temperature for the R1233zd(E) FR analysis at 95 CFM air flow.

5.1.1.3 Junction temperature

One of the most important indicators of the LTS's cooling performance is the junction temperature. This corresponds to the temperature at the interface of the heated copper block with the thermal grease used to bind the evaporator plate to it (Figure 19).

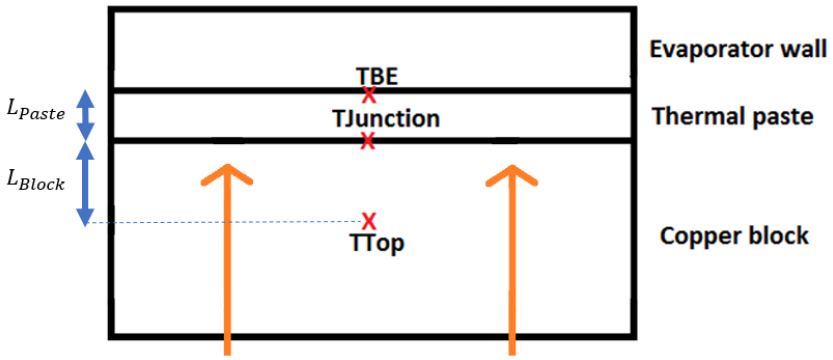

Figure 19 - Scheme of the junction between the evaporator and the copper block.

In Figure 19, *TTop* is the temperature measured in the centre of the copper block, 2 mm below the surface (*viz.* Figure 13 and Figure 14). The distance L_{Block} is 2 mm. Assuming a uniform width-wise temperature distribution in the copper block, implying unidirectional heat conduction as shown by the orange arrows, the junction temperature can be estimated from:

$$T_{Junction} = TTop - q_{cond}\frac{L_{Block}}{k_{Cu}A_{block}} \quad (8)$$

Likewise, the uncertainty propagation, from the errors in *TTop* and q_{cond}, is given by:

$$\varepsilon_{T_{Junction}}^2 = \varepsilon_{TTop}^2 + \left(\frac{L_{Block}}{k_{Cu}A_{block}}\right)^2 \varepsilon_{q_{cond}}^2 \quad (9)$$

There is an uncertainty of ±0.25°C associated with the thermocouple calibration (*Appendix A – Thermocouples calibration*), and a further ±0.35°C associated with the post-processing (Subsection 4.4.1). This results in an overall uncertainty of ±0.44°C. The uncertainty associated with the power supply is explained in Subsection 4.4.2. In practice, the uncertainty associated with the junction temperature is very similar to the measured temperature uncertainty.

The junction temperature results, as a function of the filling ratio, are shown in Figure 20.

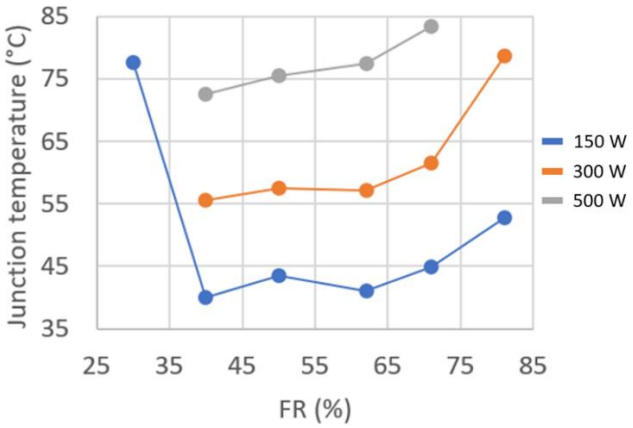

Figure 20 - Measured junction temperatures for the R1233zd(E) FR analysis at 95 CFM air flow.

The lowest junction temperatures seem to show that 40% is the best filling ratio. However, a range of optimum charge can be observed, *i.e.* between 40% and 60% (more for heat loads of 150 W and 300 W). At 30% FR, the junction temperature is considerably higher, which might indicate the beginning of dry-out of the evaporator due to lower amounts of liquid in the system.

5.1.1.4 Thermal resistance

The thermal resistance between junction and inlet air is given by:

$$TR_{LTS+TIM} = \frac{T_{Junction} - \frac{(TAirInL + TAirInR)}{2}}{q_{cond}} = \frac{T_{Junction} - T_{Air,in}}{q_{cond}} \quad (10)$$

Since the $T_{Junction}$ and $T_{Air,in}$ uncertainties are similar to the temperature measurement uncertainty (the uncertainty propagation calculations yielded values very similar to the ±0.44°C in the previous point about the junction temperature), the uncertainty associated to the thermal resistance

can be given approximately by:

$$\varepsilon_{TR}^2 = \left(\frac{\sqrt{2}\varepsilon_T}{q_{cond}}\right)^2 + \frac{\left(T_{Junction} - T_{Air,in}\right)^2}{q_{cond}^4}\varepsilon_{q_{cond}}^2 \quad (11)$$

The thermal resistance values from the filling ratio analysis of R1233zd(E) at 95 CFM air flow are shown in Figure 21.

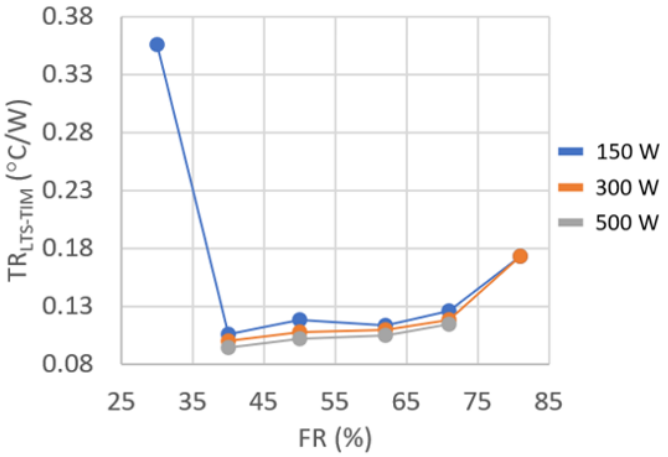

Figure 21 - Thermal resistance for the R1233zd(E) FR analysis at 95 CFM air flow.

It can be observed an optimum range of charge between 40-60% FR. This is a good outcome as this means the system is not very sensitive to the filling ratio over this range and hence this makes eventual applications easier to implement since a very accurate charge is *not* necessary.

5.1.1.5 LTS air side (left and right side increase in temperatures)

In order to verify the symmetry of the LTS performance, the increase in air temperature on each side of the LTS was determined, as well as the difference between the two sides. The thermocouples location is shown in Figure 22.

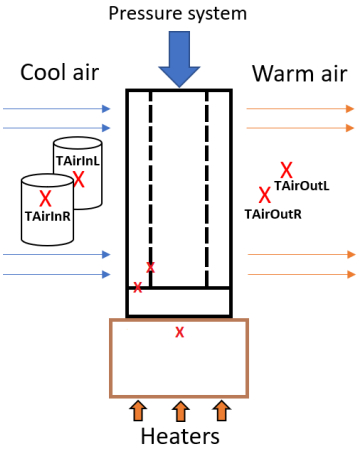

Figure 22 - Side view of the LTS, showing the location of the thermocouples for air temperature measurement.

The temperature differences plotted in Figure 23 are defined as:

$$\Delta T_{Right} = TAirOutR - TAirInR \tag{12}$$

$$\Delta T_{Left} = TAirOutL - TAirInL \tag{13}$$

$$\Delta\Delta T = \Delta T_{Right} - \Delta T_{Left} \tag{14}$$

The uncertainty associated with these temperature differences can be estimated by:

$$\varepsilon_{\Delta T} = \sqrt{\varepsilon_T^2 + \varepsilon_T^2} = \sqrt{2}\varepsilon_T = \pm 0.62°C \tag{15}$$

$$\varepsilon_{\Delta\Delta T} = \sqrt{\varepsilon_{\Delta T}^2 + \varepsilon_{\Delta T}^2} = 2\varepsilon_T = \pm 0.88°C \tag{16}$$

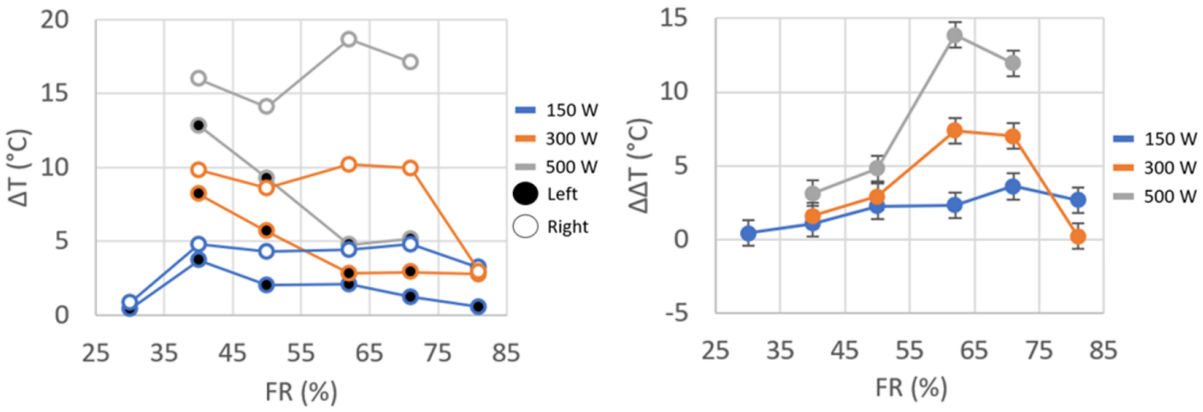

Figure 23 - Right and left side temperature increase (left plot), and right minus left side difference of the temperature increase (right plot), for the R1233zd(E) FR analysis at 95 CFM air flow.

Clearly, it can be observed that the outlet air temperature is higher on the right side for the big majority of the data points. It means the right side of the LTS seems to transfer significantly more heat

than the left side, especially for 60-70% filling ratio and high heat loads (300-500 W).

5.1.1.6 Risers

Figure 24 and Figure 25 show the thermocouples' location and the measured temperatures, respectively.

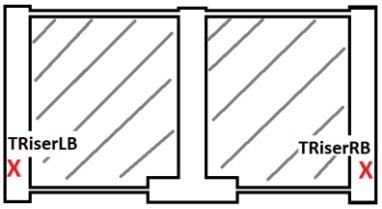

Figure 24 - Bottom riser thermocouples' locations.

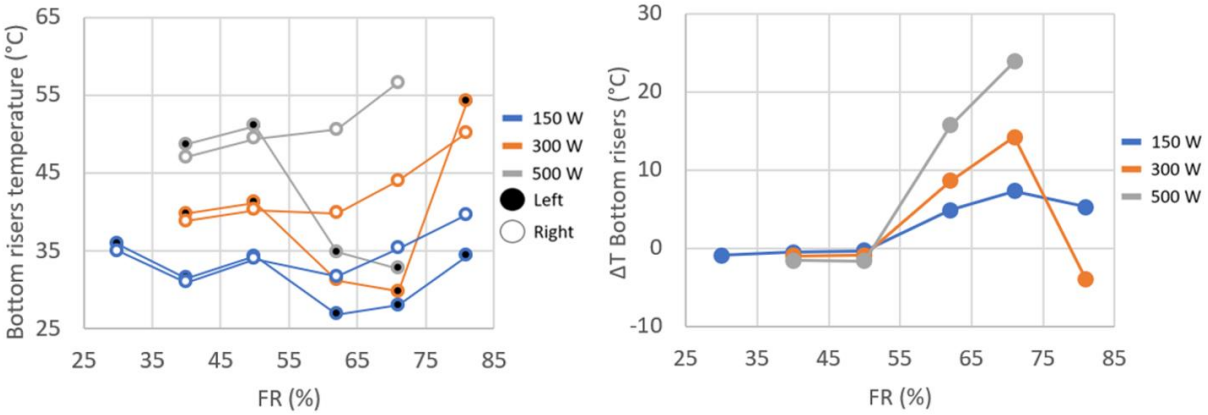

Figure 25 - Right and left side bottom riser temperatures (left plot), and right minus left side bottom riser temperatures (right plot), for the R1233zd(E) FR analysis at 95 CFM air flow.

As it was observed for the air side temperature increase, for filling ratios around 60-70%, there is a considerable decrease in temperature for the left riser (temperature drops by 10-15°C). However, for 80% FR (300 W of heat load), there is a trend reversal: the left riser temperature rises back to levels similar to the right riser. It suggests that circulation in the left side is somehow restored. However, it does not result in a lower thermal resistance: this value increases for this FR.

5.1.1.7 Bottom fins

Figure 26 and Figure 27 show the thermocouples' location and the measured temperatures, respectively.

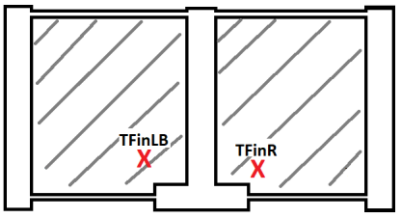

Figure 26 - Bottom fins thermocouples' locations.

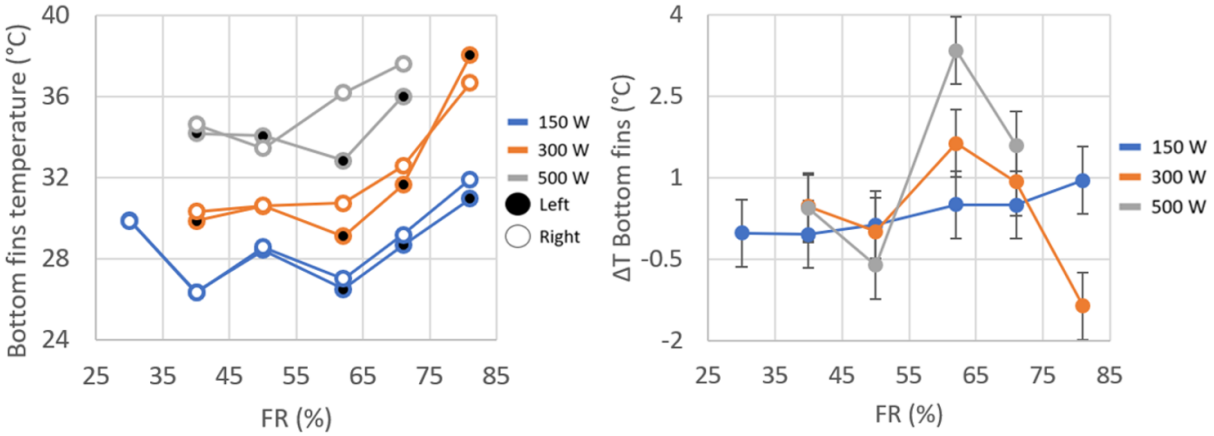

Figure 27 - Right and left side bottom fin temperatures (left plot), and right minus left side bottom fin temperatures (right plot), for the R1233zd(E) FR analysis at 95 CFM air flow.

It can be seen that the temperatures at the left and right sides of the LTS are similar (apart of 60% and 70% of FR, as it was observed in the previous item). The temperatures are also low, within 25-40°C, which might indicate some level of subcooling (saturation temperatures are within 35-65°C).

5.1.1.8 Top fins

The thermocouple locations and the measured temperatures are shown in Figure 28 and Figure 29, respectively.

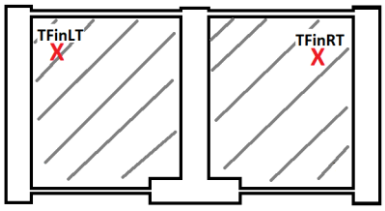

Figure 28 - Top fins thermocouples' locations.

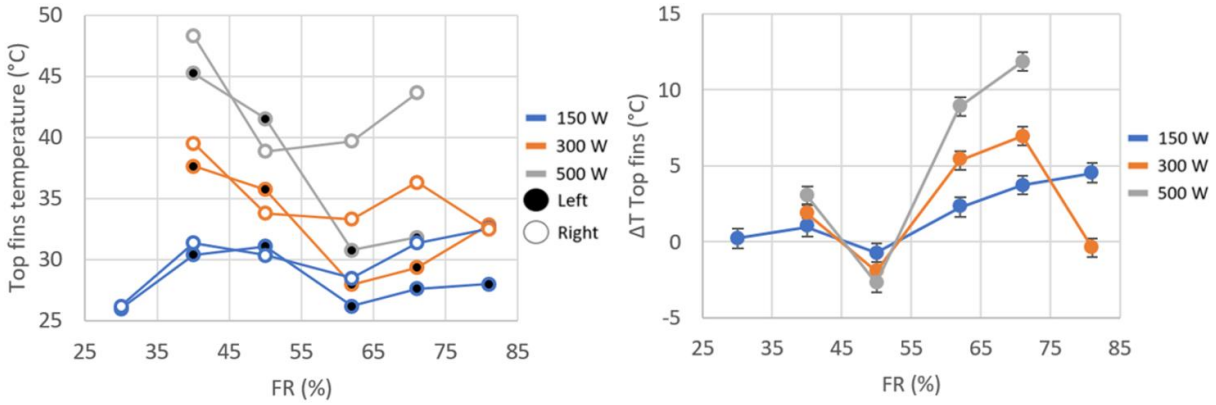

Figure 29 - Right and left side top fin temperatures (left plot), and right minus left side top fin temperatures (right plot), for the R1233zd(E) FR analysis at 95 CFM air flow.

It can be seen that, excluding the 60-70% filling ratio range, there is an overall trend for the decrease of both left and right-side fin temperatures with increasing FR. As observed for the risers' bottom, for filling ratios of around 60-70%, there is an abrupt decrease in the temperature of the left-side top fins: temperature drops by 10-15°C, when compared with a 40-50% filling ratio.

5.1.1.9 Downcomer

The downcomer temperatures and corresponding saturated temperatures (determined from the measured pressure) are plotted in Figure 30. The location of the thermocouple used for measurement is also shown.

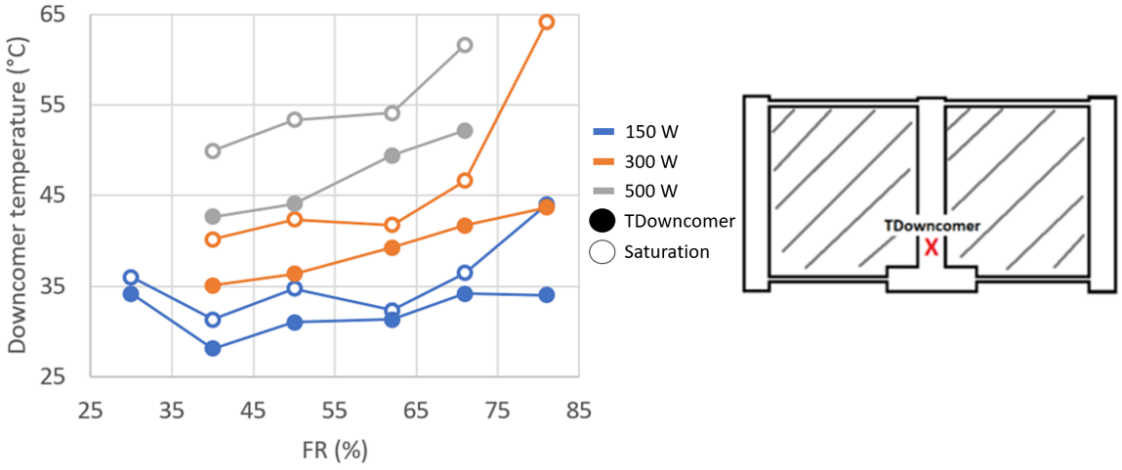

Figure 30 - Downcomer and saturation temperatures for the R1233zd(E) FR analysis at 95 CFM air flow (left). Schematic of the front of the LTS showing the thermocouple location (right).

As expected, the bottom part of the downcomer is subcooled. A higher subcooling is observed for higher heat loads, which is associated with the flooding of the condenser to accumulate the excess of mass in the cooling loop. There is also a much more pronounced subcooling at a filling ratio of 80%, which is due to the higher system pressure and even more condenser flooding.

5.1.1.10 Evaporator

Figure 31 shows the thermocouples' location, the measured evaporator temperatures and corresponding saturation temperatures. The thermocouples were attached with tape to the cover plate of the evaporator.

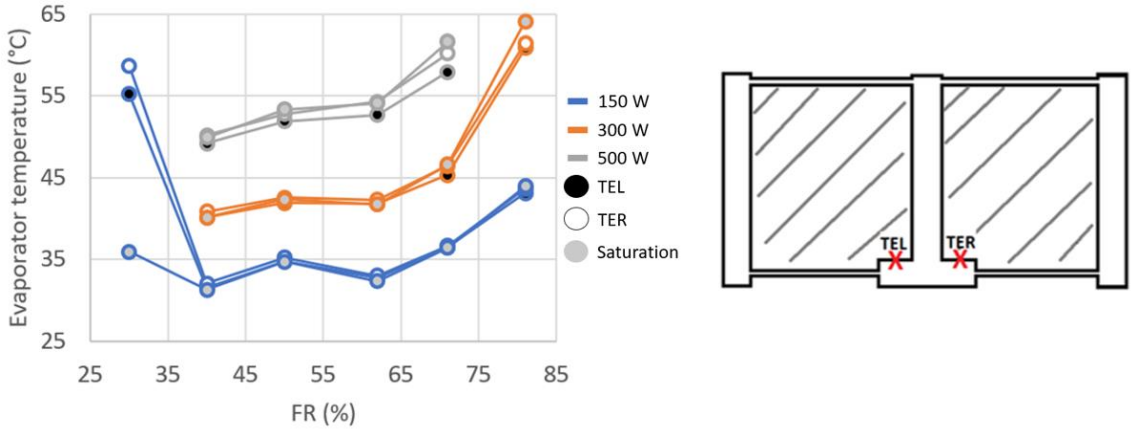

Figure 31 - Evaporator and saturation temperatures for the R1233zd(E) FR analysis at 95 CFM air flow (left). Schematic of the front of the LTS showing the thermocouple locations (right).

The evaporator temperature is generally uniform and close to the saturation temperature. However, at 70-80% FR there is a slight subcooling (2-3°C), as expected from the analysis presented in the previous item.

At 30% FR, it seems a very high superheating is observed (20-25°C). However, the riser temperatures showed in Figure 25 are not above saturation. This might be because there is a partial dry out of the evaporator, causing an increase in temperature of the boiling surface (the internal evaporator fins, *viz*. Figure 7) which heats the evaporator cover plate by conduction.

5.1.2 R1233zd(E) and R1234ze(E) charge determination under constant heat load

In addition to the optimum charge determination at constant air flow and varying heat load, a charge determination at a constant heat load and varying air volumetric flow rate was also performed. In this case, two fluids were tested: R123zd(E) and R1234ze(E). For R1233zd(E), tests were performed for five different charges of fluid, corresponding to filling ratios of 29%, 40%, 51%, 60% and 71%. For each of these fluid charges, the LTS was tested for air volumetric flow rates of 59, 118 and 178 CFM (100, 200 and 300 m^3/h). For R1234ze(E), the LTS was charged with the R1234ze(E), for five charges of fluid, corresponding to filling ratios of 41%, 50%, 60%, 70% and 80%. For each of these fluid charges, the LTS was tested for air volumetric flow rates of 40, 59 and 118 CFM (67, 100 and 200 m^3/h). Both fluids were tested under a constant heat load of around 500 W (31.3 W/cm^2). The goal was to assess the influence of a wider range of air volumetric flow rates, for a high heat load, on the determination of the optimum filling ratio range, for two different working fluids.

The following points describe the main results obtained from this set of tests. The main test parameters are listed in Table 3.

Table 3 - Main parameters for testing with the R2133zd(E) and R1234ze(E) charges for filling ratio analysis.

Working fluid	R1233zd(E)	R1234ze(E)
Copper block cross-section (cm^2)	16	
Filling ratio (%)	29-71	41-80
Applied pressure (bar/psi)	2.4/34	
Heat load (W)	500	
Air volumetric flow rates (CFM)	59-178	40-118
Thermal grease resistance (°C/W) [18]	0.00325	
k_{Paste} (W/mK)	11	
k_{Cu} (W/mK)	398	
L_{Block} (mm)	2	
TIM resistance (>30 psi) (°C/W)	0.00375	

5.1.2.1 Inlet air temperature

The temperature of the inlet air passing through the thermosyphon fins for each filling ratio (FR), as well as the location of the thermocouples in the system, are shown in Figure 32.

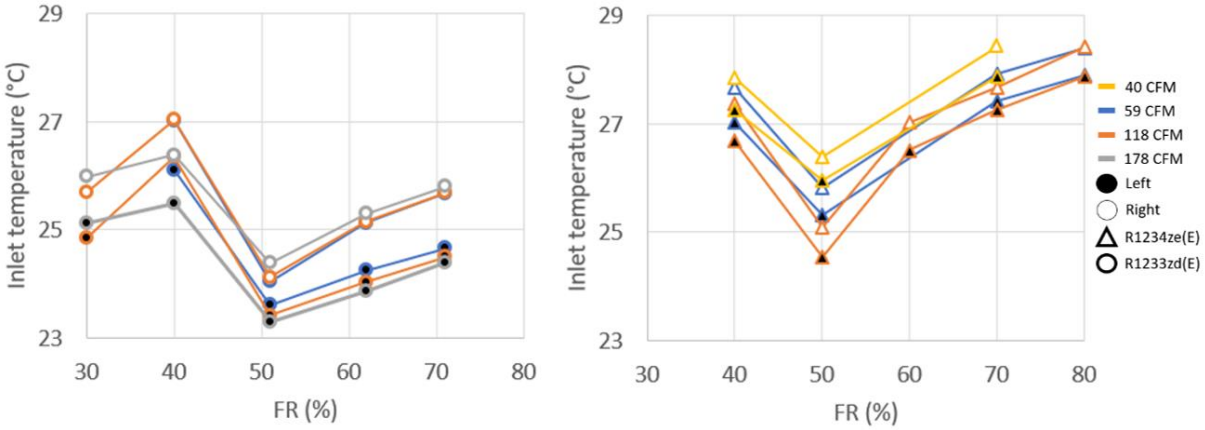

Figure 32 - Inlet air temperature for the FR analysis at 500 W of heat load, for the two working fluids.

5.1.2.2 Pressure and saturation temperature

The measured pressure, as well as the corresponding saturation temperature for each of the fluids, are shown in Figure 33. The saturation temperature is obtained from the pressure through the working fluids' vapour pressure curve in the CoolProp database [17].

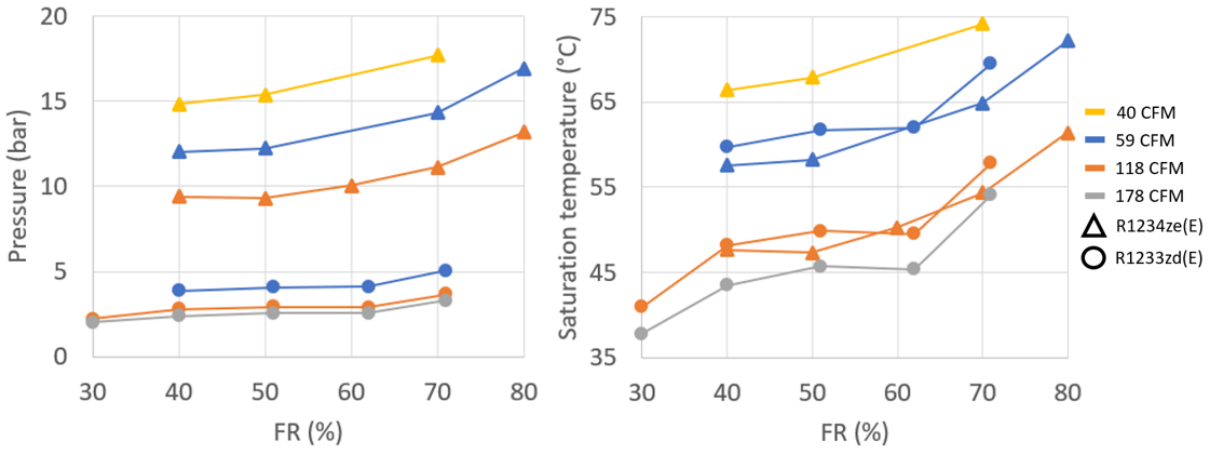

Figure 33 - Comparison of the pressure and saturation temperature values for the filling ratio analyses with the R2133zd(E) and R1234ze(E) charges.

The saturation temperature is similar, but slightly lower for R1234ze(E). This is a consequence of the overall similar, but slightly lower temperatures for this fluid in the LTS. As a consequence, given the thermodynamic properties of the fluids, the corresponding pressure is much higher for R1234ze(E).

5.1.2.3 Junction temperature

The junction temperature, whose calculation procedure and concept are described in point 5.1.1.3, is plotted, for each of the working fluids, as a function of the filling ratio in Figure 34.

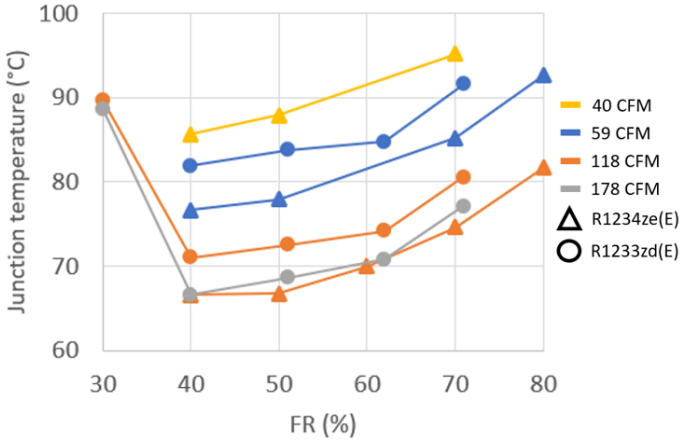

Figure 34 - Comparison of the junction temperature values for the filling ratio analyses with the R2133zd(E) and R1234ze(E) charges.

In the previous subsection (5.1.1), for filling ratios of 30 and 80%, it had not been possible to test the system at a heat load of 500 W without exceeding the safety temperature, due to the lower air volumetric flow rate. In this case, at higher air volumetric flow rates, it was possible to do so for 30% FR for both working fluids, and for 80% FR for R1234ze(E).

The junction temperature is generally 4-6°C lower for R1234ze(E). Also, this fluid seems to

have a better performance at very high filling ratios: at 80% FR, it was not possible to test R1233zd(E), because it would reach temperatures over 100°C. This is not the case for R1234ze(E).

The optimum filling ratio range is 40-60%. The junction temperature is particularly high for 30% FR. This is probably caused by a localised, partial dry-out in the evaporator.

5.1.2.4 Thermal resistance

The concept and calculation process of the thermal resistance are described in point 5.1.1.4. The thermal resistance values are shown, for both working fluids, in Figure 35.

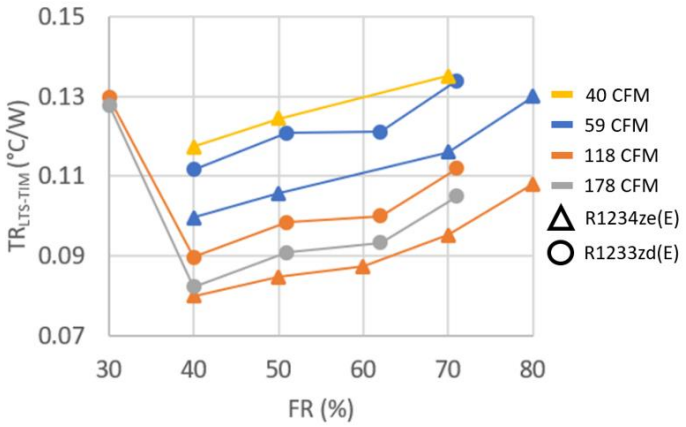

Figure 35 - Comparison of the thermal resistance values for the filling ratio analyses with the R2133zd(E) and R1234ze(E) charges.

The thermal resistance is about 5-10% lower for R1234ze(E), for all comparable filling ratios and air flows. An optimum range of charge can also be observed between 40-60% FR. As inferred from the temperature junction data, there is a clearly worse performance at 30% and 80% filling ratio. For filling ratios higher than 30%, the thermal resistance increases with increasing FR.

From the junction temperature and thermal resistance values, it can be concluded that 40-60% is the ideal filling ratio range, in line with previous results.

5.1.2.5 LTS air side (left and right side increase in temperatures)

The increase in air temperature on each side of the LTS, as well as the difference between these two, as mentioned in point 5.1.1.5, are shown in Figure 36 for both working fluids. The thermocouples' location is shown in Figure 22.

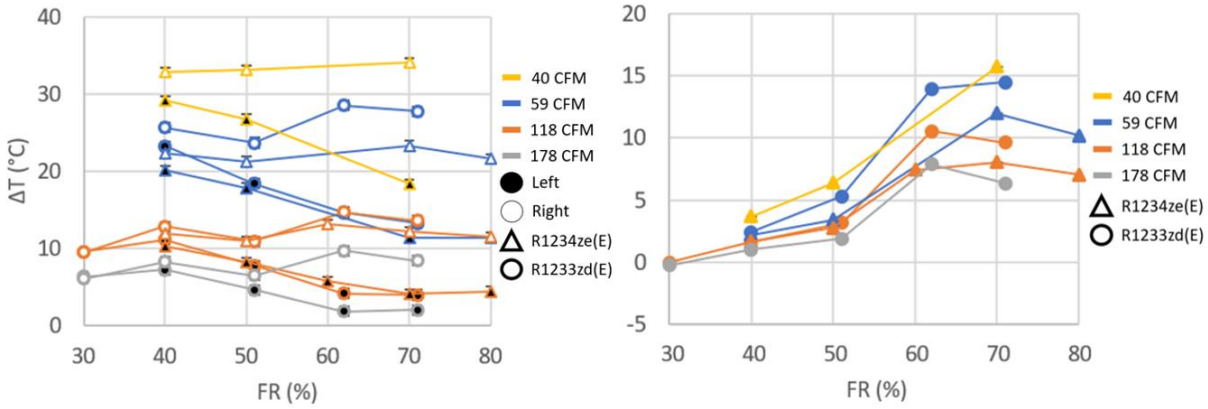

Figure 36 - Comparison of the right and left side temperature increase (left plot), and right minus left side difference of the temperature increase (right plot), for the filling ratio analyses with the R2133zd(E) and R1234ze(E) charges.

There is a clear asymmetrical behaviour between the two sides of the LTS, for filling ratios around 60-70%. For these filling ratios, there is an increase in the right-side heating of the air, and a decrease in the left side. As a result, the right side of the LTS seems to transfer significantly more heat than the left side for this filling ratio range. The asymmetry seems to be slightly smaller for R1234ze(E).

The right side increase in air temperature is fairly constant for all filling ratios, for each air volumetric flow rate. What causes the increase in the asymmetrical heating is the decrease of the left side heating with increasing filling ratio.

5.1.2.6 Risers

The thermocouples' location and the measured temperatures for the two working fluids are shown in Figure 25 and Figure 37, respectively.

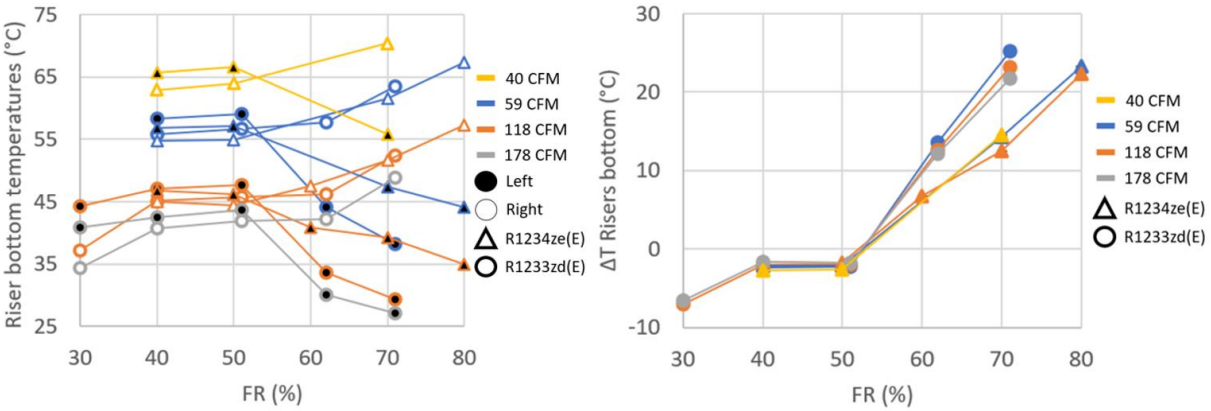

Figure 37 - Comparison of the right and left side bottom riser temperatures (left plot), and right minus left side bottom riser temperatures (right plot), for the filling ratio analyses with the R2133zd(E) and R1234ze(E) charges.

For filling ratios of around 60-70%, there is a considerable decrease in the temperature of the

left riser; temperature drops by 10-15°C, when compared with a 40-50% filling ratio. For filling ratios above 50%, the left riser temperature decreases and the right riser temperature increases.

The asymmetrical behaviour does not seem to be affected by the air volumetric flow rate.

5.1.2.7 Bottom fins

The thermocouples' location and the measured temperatures of the bottom fins, for each of the working fluids, are shown in Figure 26 and Figure 38, respectively.

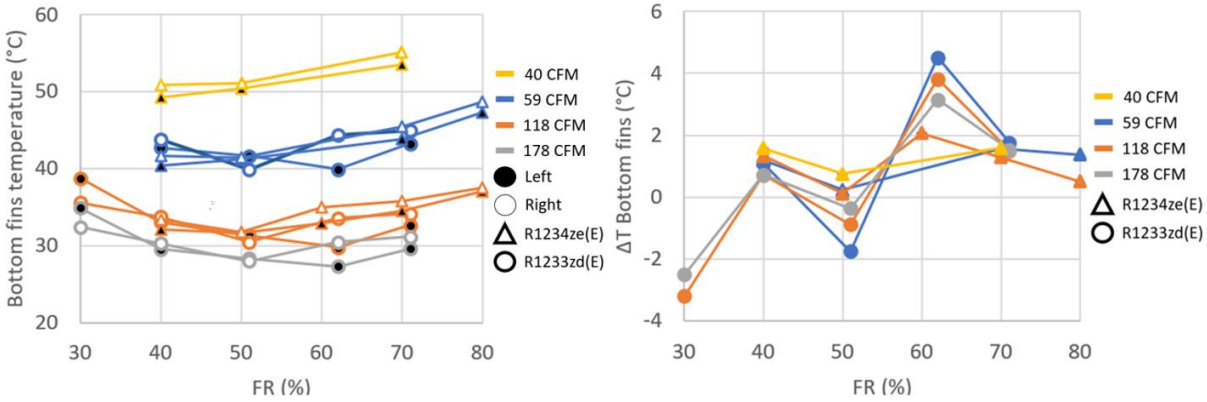

Figure 38 - Comparison of the right and left side bottom fin temperatures (left plot), and right minus left side bottom fin temperatures (right plot), for the filling ratio analyses with the R2133zd(E) and R1234ze(E) charges.

There does not seem to be a significant difference between the two fluids. The temperature of the bottom fins is similar in both the left and right sides of the LTS. The temperature values are also relatively low, within 25-45°C, which is consistent with the thermocouples being closer to the downcomer than to the risers.

The temperatures are similar for both working fluids, and the asymmetry is slightly less pronounced for R1234ze(E).

5.1.2.8 Top fins

The thermocouples' location and the measured temperatures of the top fins of the LTS, for the two working fluids, are shown in Figure 28 and Figure 39, respectively.

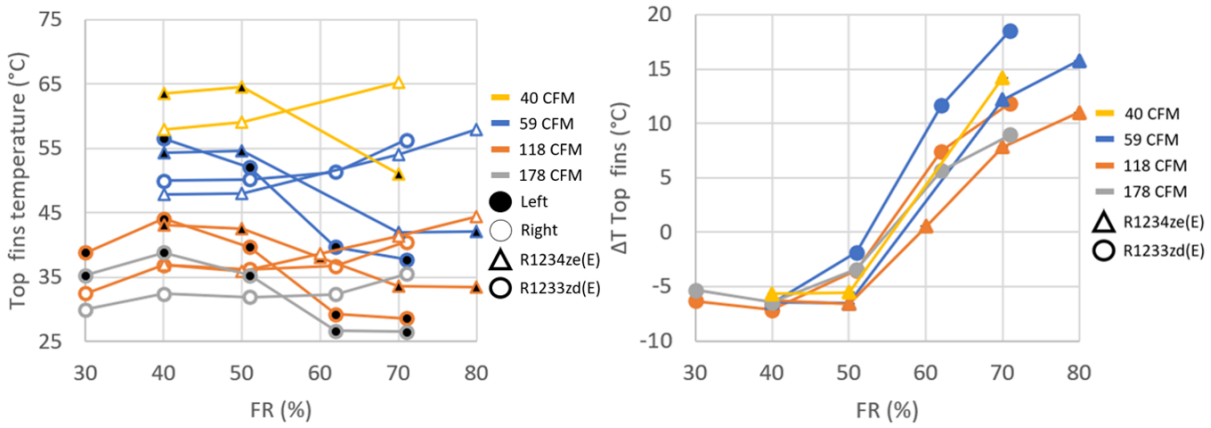

Figure 39 - Comparison of the right and left side top fin temperatures (left plot), and right minus left side top fin temperatures (right plot), for the filling ratio analyses with the R2133zd(E) and R1234ze(E) charges.

The thermal behaviour of the top fins is the same as the one of the risers (point 5.1.2.6): uniformity below 50% and an abrupt decrease in the temperature of the left-side top fins, with the temperature dropping by 10-15°C; there is also a smaller increase (5-10°C) of the right-side fins' temperature when compared with 40-50% FR. The fluid R1234ze(E) seems to perform better, with a smaller asymmetry than for R1233zd(E) (for 60-70% FR).

5.1.2.9 Downcomer

The downcomer temperature values and the corresponding saturated temperature values (calculated from the pressure) are plotted in Figure 40, for the two working fluids. The location of the thermocouple used for measurement is shown in Figure 30.

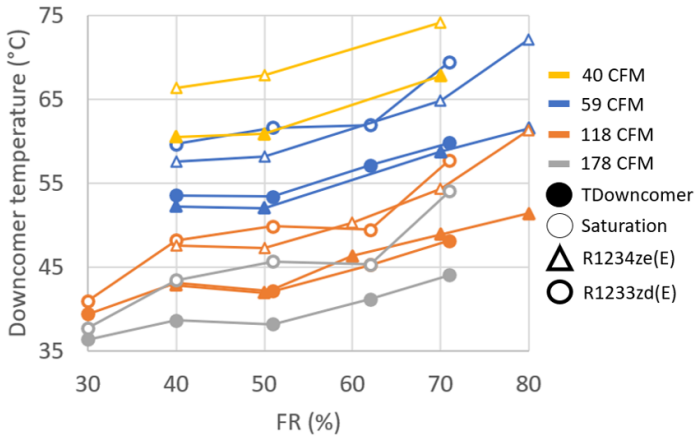

Figure 40 - Comparison of the downcomer and saturation temperature values for the filling ratio analyses with the R2133zd(E) and R1234ze(E) charges.

The overall trend is for the temperature to increase with increasing filling ratio. It is very similar for both fluids, while the saturation temperature is slightly smaller for R1234ze(E).

As expected, the bottom part of the downcomer is subcooled by about 3-5°C for most filling ratios. This results from the subcooling of the condensed liquid in the condenser section. There seems to be no impact of the air volumetric flow rate on the level of subcooling. There is a much more pronounced subcooling (around 10°C) at a filling ratio of 80% than at other filling ratios (for R1234ze(E)), due to the much higher pressure and consequently higher saturation temperature.

5.1.2.10 Evaporator

The thermocouples' location is shown in Figure 31 and the measured evaporator temperatures and corresponding saturation temperatures, for each working fluid, are shown in Figure 41. The thermocouples are attached with tape to the cover plate of the evaporator.

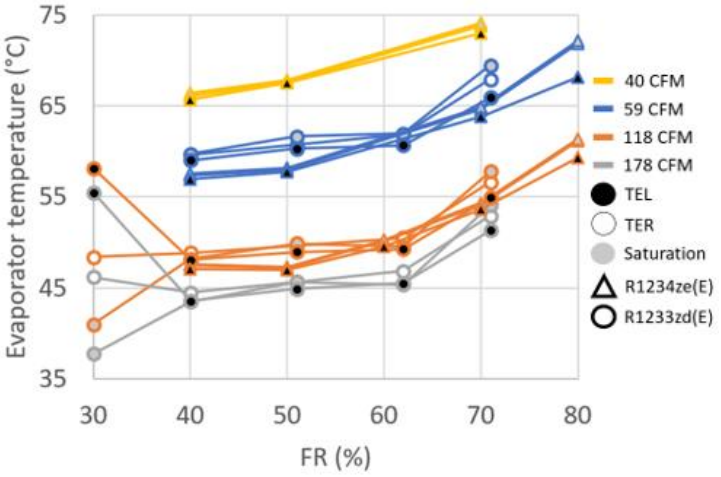

Figure 41 - Comparison of the evaporator and saturation temperature values for the filling ratio analyses with the R2133zd(E) and R1234ze(E) charges.

The evaporator temperature is very similar to saturation temperature for both fluids. Therefore, it is slightly lower for R1234ze(E) than for R1233zd(E). The evaporator temperature is generally uniform, and close to the saturation temperature.

For the R1234ze(E) charge at 80% FR there is, however, some subcooling (5-6°C), probably due to the greater subcooling of the column of liquid in the downcomer at these filling ratios as discussed in the previous point.

For the R1233zd(E) charge at 30% FR there is apparently a very significant superheating (10-20°C), which is probably caused by partial dry-out of the evaporator. Since the risers are near saturation, what is happening is that the metallic surface temperatures of the evaporator are overheating. There is also a large asymmetry for this FR, with the left side of the evaporator about 9°C warmer than the right side. This asymmetry did not happen in the previous filling ratio analysis (point 5.1.1.10), which was performed at much lower heat loads (150-300 W).

5.1.3 Results summary

The determination of the optimum filling ratio range yielded the same results, both for tests at constant heat load, and for tests at constant air volumetric flow rate: the junction temperature and thermal resistance are minimised for the 40-60% filling ratio range. This analysis also showed, in parallel, the results for a similar analysis performed with R1234ze(E). And while the optimum filling ratio range was similar (40-60%) for both fluids, and the best thermal performance seemed to be for 40% FR, it is worth noting that it was possible to test R1233zd(E) down to 30%, while for R1234ze(E) this was not possible due to overheating of the copper block. Therefore, for subsequent tests at optimum filling ratio, a value of 40% was chosen for R1233zd(E), while a value of 50% was chosen for R1234ze(E).

For the filling ratio analyses at constant heat load (Subsection 5.1.2), R1234ze(E) shows lower values of junction temperature (5-10°C) and thermal resistance (5-10% less) than R1233zd(E), for all filling ratios and air volumetric flow rates. For the most problematic filling ratios (60-70%), where circulation decreases or even stops in the left side of the LTS, as shown by the drop in the left riser temperature (Figure 37), R1234ze(E) also appears to have a better performance, with the difference between the right and left side being smaller.

On the one hand, the lower viscosity of R1234ze(E) would allow for a lower flow resistance in the left side, increasing the mass flow. However, the liquid density of this fluid is also lower, which would reduce the driving force (Eq. 17), reducing the mass flow. A more detailed, quantitative analysis would be required to analyse the influence of these parameters.

$$\Delta P_{driver} = (\rho_{downcomer} - \rho_{riser})gh = \Delta P_{friction} + \Delta P_{mom.} \quad (17)$$

However, this equation also allows an explanation for the fact that the thermal performance seems to decrease in the left side of the LTS, for certain conditions (higher heat loads and 60-70% FR). If there are partial blockages in the left side condenser MPTs, particularly the ones in the top, this

can both reduce the effective height, *h*, and increase the frictional pressure drop, $\Delta P_{friction}$. If, for unrelated reasons, filling ratios of 60-70% would result in a higher internal pressure drop anyway, this increase could be enough to stop circulation in the left side, but not in the right side, due to the partial blockages and reduced effective height.

For both fluids, the top fins are generally warmer than the bottom fins. This is probably because the thermocouples in the former are closer to the riser, while the thermocouples in the latter are closer to the downcomer. The bottom fins are generally uniform in temperature, while the top fins show an asymmetry similar to the risers'.

For 80% FR, the downcomer subcooling is the most pronounced, being 10°C for R1234ze(E) and 500 W (Figure 40) and 20°C for R1233zd(E) at 300 W and 95 CFM (Figure 30). This is caused by the increase in pressure at this high filling ratio, greatly increasing the saturation temperature. There is also a slight subcooling of the evaporator at 80% FR, for the same reason, as well as an apparent superheating and asymmetry at 30% FR (for R1233zd(E)), with the left side much warmer than the right side; however, the risers' temperatures seem to be close to saturation. This is probably due to localised dry-outs in the evaporator, increasing the internal fin temperatures of the evaporator, and consequently the evaporator cover temperatures (by conduction). The air volumetric flow rate does not seem to have an impact on subcooling.

The determination of the optimum charge was therefore the same, regardless of whether the analysis was performed at a constant heat load and changing air volumetric flow rate, or at a constant air volumetric flow rate and changing heat load. There was a clearly decreased performance in the left side of the LTS for filling ratios around 60-70%, which is likely explained by partial blockages of the MPTs in that side (see Chapter 6). At these air volumetric flow rates, heat loads and filling ratios, R1234ze(E) seems to perform slightly better than R1233zd(E). The only disadvantage of R1234ze(E) seems to be the much higher pressure values involved (maximum of 17 bar compared with 5 bar for R1233zd(E)).

5.2 Testing at optimum filling ratio

Having performed three sets of tests for the determination of the optimum filling ratio, it was concluded that there is an optimum range between 40 and 60%. After the tests described in Subsection 5.1.1, a charge corresponding to 46% FR was tested; after the ones in Subsection 5.1.2, the LTS was charged at 41% FR for R1233zd(E) and 51% for R1234ze(E). The reasons for this choice of filling ratios are explained in Subsection 5.1.3. Testing was performed for varying heat loads and air volumetric flow rates.

5.2.1 R1233zd(E) charge at 46% filling ratio

This set of tests followed the filling ratio analysis described in Subsection 5.1.1. The LTS was charged with R1233zd(E) corresponding to a filling ratio of 46%. The LTS was tested for heat loads between 100 and 700 W (heat fluxes of 6.3-43.8 W/cm^2) for three levels of air volumetric flow rates: 89, 133 and 178 CFM (150, 225 and 300 m^3/h). The goal was to evaluate the performance of the LTS and its operational limits using a filling ratio that yields the minimum thermal resistance.

The following points describe the main results obtained from this set of tests. The main test parameters are listed in Table 4.

Table 4 - Main parameters for testing at 46% filling with R1233zd(E).

Copper block cross-section (cm^2)	16
Filling ratio (%)	46
Working fluid	R1233zd(E)
Applied pressure (bar/psi)	2.4/34
Heat load (W)	100-700
Air volumetric flow rates (CFM)	89-178
Thermal grease resistance (°C/W) [18]	0.00325
k_{Paste} (W/mK)	11
k_{Cu} (W/mK)	398
L_{Block} (mm)	2
TIM resistance (>30 psi) (°C/W)	0.00375

5.2.1.1 Inlet temperature

The temperatures of the inlet air passing through the thermosyphon fins are shown in Figure 42. The locations of the thermocouples in the system are shown in Figure 17.

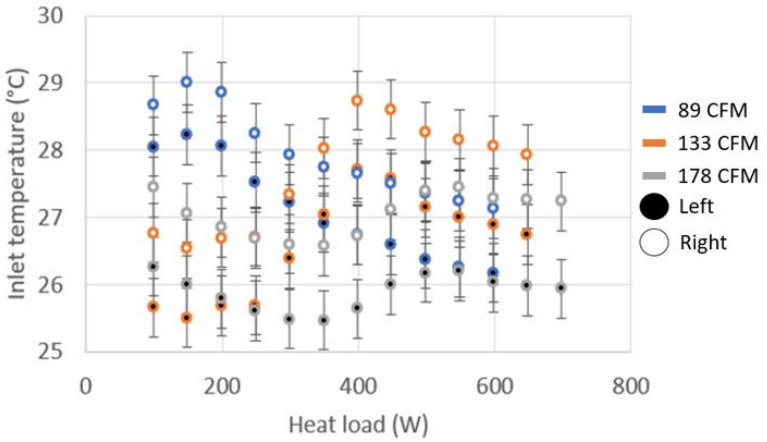

Figure 42 - Inlet air temperature for testing at 46% filling ratio and R1233zd(E) charge (left). Schematic of the front of the LTS showing the thermocouple locations (right).

5.2.1.2 Pressure and saturation temperature

The measured pressure, as well as the corresponding saturation temperature, are shown in Figure 43. The saturation temperature is obtained from the pressure through the working fluid's vapour pressure curve in the CoolProp database [17].

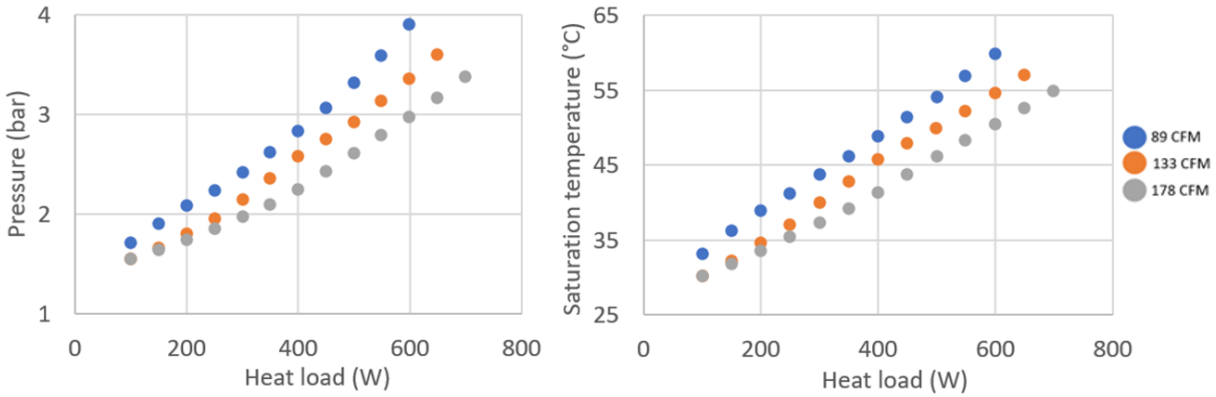

Figure 43 - Pressure and saturation temperature for testing at 46% filling ratio and R1233zd(E) charge.

As expected, with increasing heat load, the system's pressure increases. Assuming similar values of thermal resistance and inlet air temperature, the junction temperature and, by extension, the evaporator and all the temperatures inside the LTS, increase with increasing heat load:

$$T_{Junction} = TR_{LTS+Paste} * q_{cond} + T_{Air,in} \quad (18)$$

Therefore, in order to reach thermodynamic equilibrium, there is also a pressure increase.

5.2.1.3 Junction temperature

The junction temperature, whose calculation procedure and concept are described in point 5.1.1.3, is plotted as a function of the filling ratio in Figure 44.

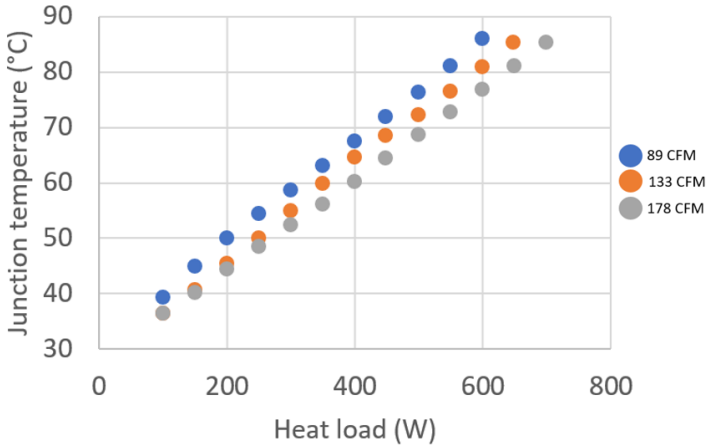

Figure 44 - Measured junction temperatures for testing at 46% filling ratio and R1233zd(E) charge.

The system was operated up until the point when the junction temperature reached 90°C. For practical applications, higher temperatures are not desirable. With the highest air volumetric flow rate (178 CFM), it was possible to transfer up to 700 W of heat, or 43.8 W/cm^2 of heat flux. The junction temperature increases almost linearly with increasing heat load, suggesting a similar thermal resistance throughout the tests (Eq. 18).

The junction temperature is also smaller for higher air volumetric flow rates, as heat transfer is more efficient in the condenser for higher air volumetric flow rates, which decreases the overall thermal resistance.

5.2.1.4 Thermal resistance

The concept and calculation process of the thermal resistance are described in point 5.1.1.4. The thermal resistance values are shown in Figure 45.

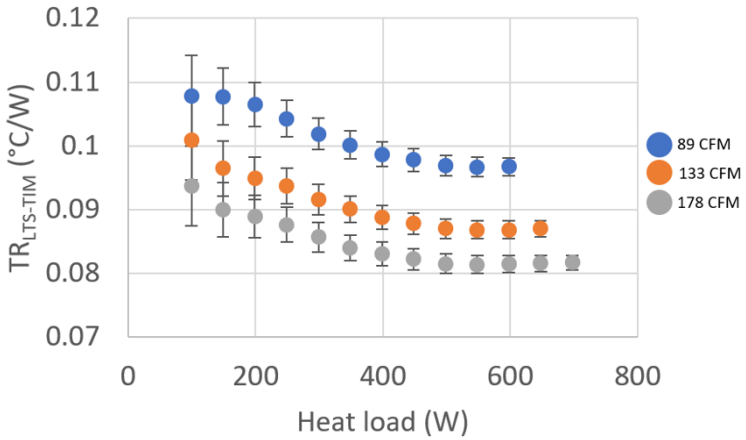

Figure 45 - Thermal resistance for testing at 46% filling ratio and R1233zd(E) charge.

The thermal resistance decreases gradually with increasing heat load, until it stabilises for heat loads greater than 500 W (31.3 W/cm^2). It stays within a range of 0.08-0.11°C/W. This narrow range explains the relative linearity of the junction temperature (point 5.2.1.3).

The decrease in thermal resistance can be explained by the increase in the mass flow rate which increases the fluid-side heat transfer coefficient and consequently lowers the thermal resistance. The flattening of the thermal resistance curve to a near constant value at the higher heat loads must come from a stabilization of the microchannel boiling heat transfer coefficient, since the other resistances in the evaporator are all conduction and thus already constant. It might also indicate the beginning of the transition from GDR to FDR.

5.2.1.5 LTS air side (left and right side increase in temperatures)

In order to verify the symmetry of the LTS performance, the increase in air temperature on each side of the LTS was determined, as well as the difference between these two, as mentioned in point 5.1.1.5. The thermocouples' location is shown in Figure 22, and the results are shown in Figure 46.

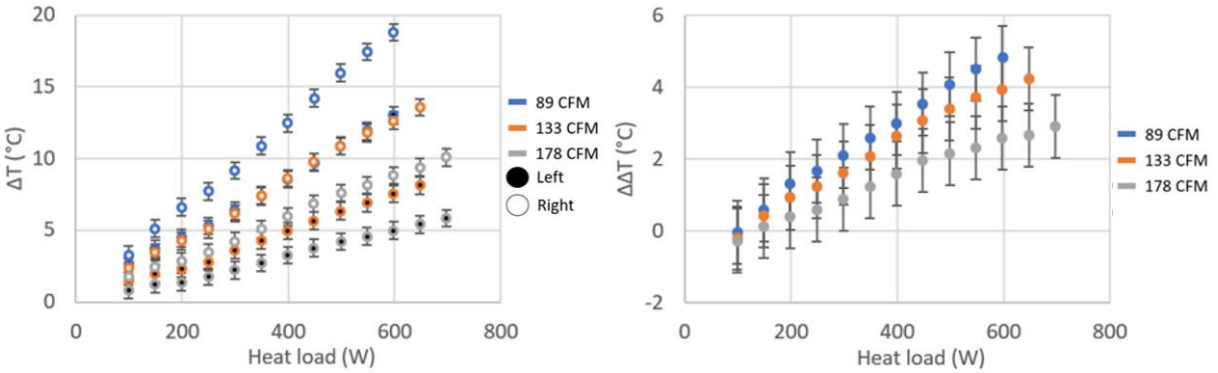

Figure 46 - Right and left side temperature increase (left plot), and right minus left side difference of the temperature increase (right plot), for testing at 46% filling ratio and R1233zd(E) charge.

As seen in Subsections 5.1.1 and 5.1.2, the air heats up more on the right side of the LTS. It had been observed that the difference was more moderate for the optimum filling ratio, between 1-5°C of difference in heating between the right and left side, for heat loads and air volumetric flow rates ranging from 150-500 W and 59-178 CFM, respectively (Figure 23 and Figure 36). In this case, testing for a filling ratio of 46%, the observed differences were of the same order, but the operation at a constant FR allowed the effect of the heat load and air volumetric flow rate to be studied: the asymmetry is higher for lower air volumetric flow rates, and for higher heat loads.

Assuming the hypothesis put forward in Subsection 5.1.3, that there is a partial blockage or manufacturing defects in the left-side MPTs (analysed in detail in Chapter 6), since there is more resistance to flow in the left side, the mass flow rate in the right side would increase more than in the left side, for increasing heat loads, leading to a progressively higher difference in heat transfer between the two sides.

The maximum difference in heating between the two sides is around 5°C, even at junction temperatures close to 90°C, while for other filling ratios (Figure 23 and Figure 36), this difference can reach 15°C. This clearly shows the better performance of a filling ratio of 46%.

5.2.1.6 Risers

The thermocouples' location and the measured riser temperatures are shown in Figure 25 and Figure 47.

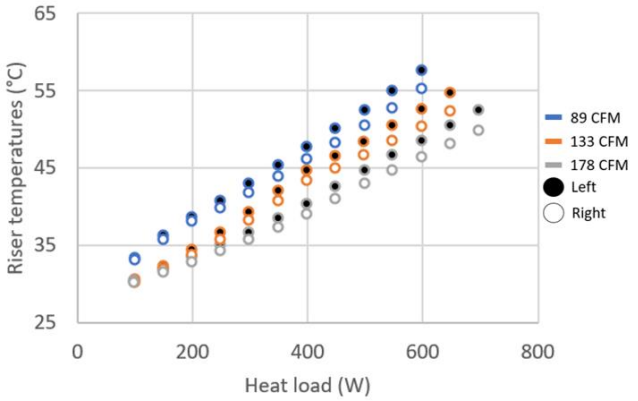

Figure 47 - Right and left side bottom riser temperatures (left), and right minus left side bottom riser temperatures (right), for testing at 46% filling ratio and R1233zd(E) charge.

Similar to the air temperature increase, the difference in temperature between the two sides increases with increasing heat load, although this difference is at most 4°C. But unlike the air temperature increase, the left riser's temperature is higher than the right side's. In the filling ratio analysis, it was concluded that circulation stopped in the left side, causing the temperature values to drop abruptly in the left riser. However, this only happened for filling ratios around 60-70%. For the range between 40-50% FR, the left side riser is actually slightly warmer than the right side (*viz.* Figure 25 and Figure 37).

5.2.1.7 Bottom fins

The thermocouples' location and the measured temperatures of the bottom fins are shown in Figure 26 and Figure 48, respectively.

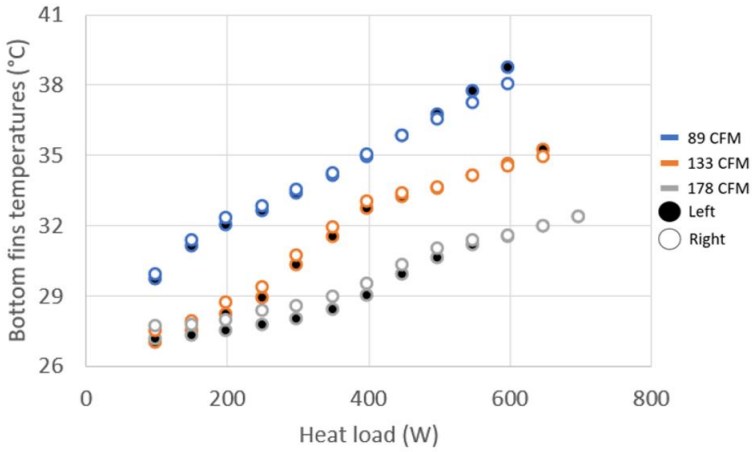

Figure 48 - Right and left side bottom fin temperatures (left), and right minus left side bottom fin temperatures (right), for testing at 46% filling ratio and R1233zd(E) charge.

As shown in the filling ratio analyses (Figure 26 and Figure 38), the bottom fins' temperature is uniform on both sides of the LTS, and is always below 40°C, which suggests some level of subcooling.

As expected, higher heat loads (and hence higher junction temperature for the same thermal resistance) and lower air volumetric flow rates (higher thermal resistance) increase the fins' temperatures because they increase the overall temperature of the LTS.

5.2.1.8 Top fins

The thermocouples' location and the measured temperatures of the top fins of the LTS are shown in Figure 28 and Figure 49, respectively.

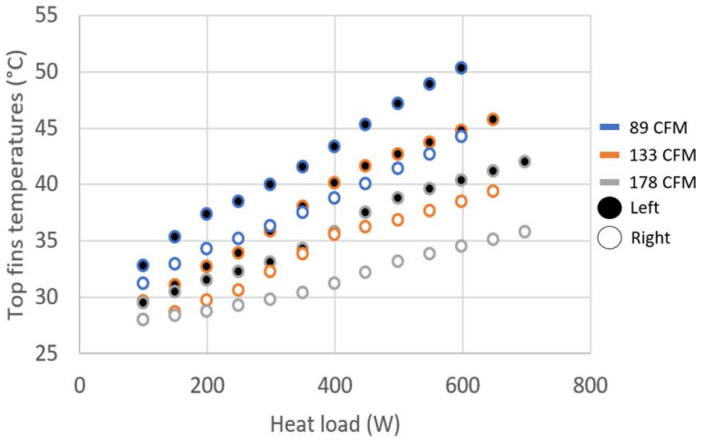

Figure 49 - Right and left side top fin temperatures (left), and right minus left side top fin temperatures (right), for testing at 46% filling ratio and R1233zd(E) charge.

The left-side top fins are warmer than the right-side ones, the same way as the risers. Like in that case, the difference increases with increasing heat load, while the air volumetric flow rate does not seem to have an influence.

Both left and right-side fins steadily increase their temperature with increasing heat load, also similar to the risers.

5.2.1.9 Downcomer

The downcomer temperature values and the corresponding saturated temperature values (calculated from the pressure) are plotted in Figure 50. The location of the thermocouple used for the temperature measurement is shown in Figure 30.

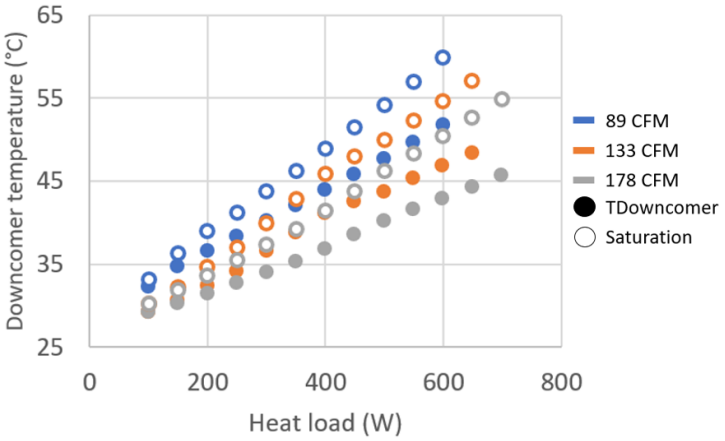

Figure 50 - Downcomer and saturation temperatures for testing at 46% filling ratio and R1233zd(E) charge (left). Schematic of the front of the LTS showing the thermocouple location (right).

As previously noted (Section 5.1), the downcomer is significantly subcooled and the subcooling does not seem to be influenced by the air volumetric flow rate. However, the level of subcooling increases with increasing heat load. This is probably the result of flooding due to liquid accumulation in the condenser MPTs, caused by the increased circulation inside the LTS.

5.2.1.10 Evaporator

The thermocouple locations are shown in Figure 31 and the measured evaporator temperatures and corresponding saturation temperatures are shown in Figure 51. The thermocouples are attached with tape to the cover plate of the evaporator.

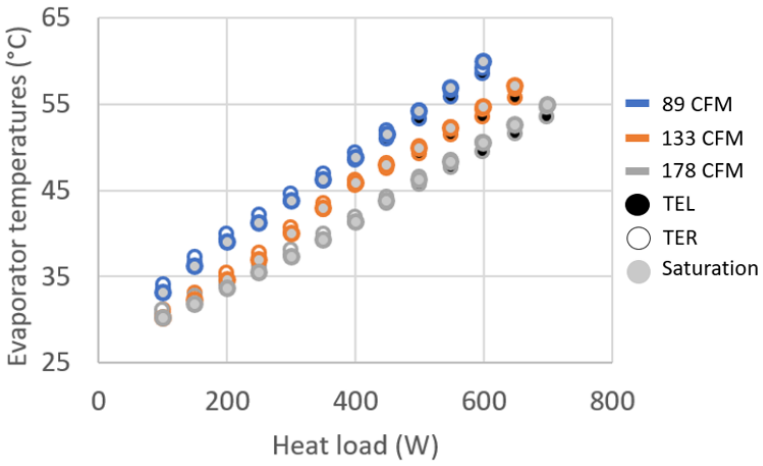

Figure 51 - Evaporator and saturation temperatures for testing at 46% filling ratio and R1233zd(E) charge (left). Schematic of the front of the LTS showing the thermocouple locations (right).

The evaporator temperature is generally uniform, and close to the saturation temperature, and changes in heat load or air volumetric flow rate do not seem to cause any asymmetry. This had already been observed in Section 5.1 for filling ratios in the 40-50% range.

5.2.2 LTS Thermal Performance Comparison: R1233zd(E) versus R1234ze(E)

This Subsection compares the test results for a charge of R1233zd(E) at 41%, with the results for a charge of R1234ze(E) at 51%, which followed the filling ratio analyses described in Subsection 5.1.2. Other than the charge, all other test parameters were the same (Table 5) for both sets of tests.

Table 5 - Main parameters for testing with the R2133zd(E) and R1234ze(E) charges at optimum filling ratio.

Working fluid	R1233zd(E)	R1234ze(E)
Copper block cross-section (cm^2)	16	
Filling ratio (%)	41	51
Applied pressure (bar/psi)	2.4/34	
Heat load (W)	100-500	50-500
Air volumetric flow rates (CFM)	40-118	
Thermal grease resistance (°C/W) [18]	0.00325	
k_{Paste} (W/mK)	11	
k_{Cu} (W/mK)	398	
L_{Block} (mm)	2	
TIM resistance (>30 psi) (°C/W)	0.00375	

5.2.2.1 Inlet air temperature

The inlet air temperature through the thermosyphon fins for all filling ratios (FR), as well as the location of the thermocouples, are shown in Figure 52.

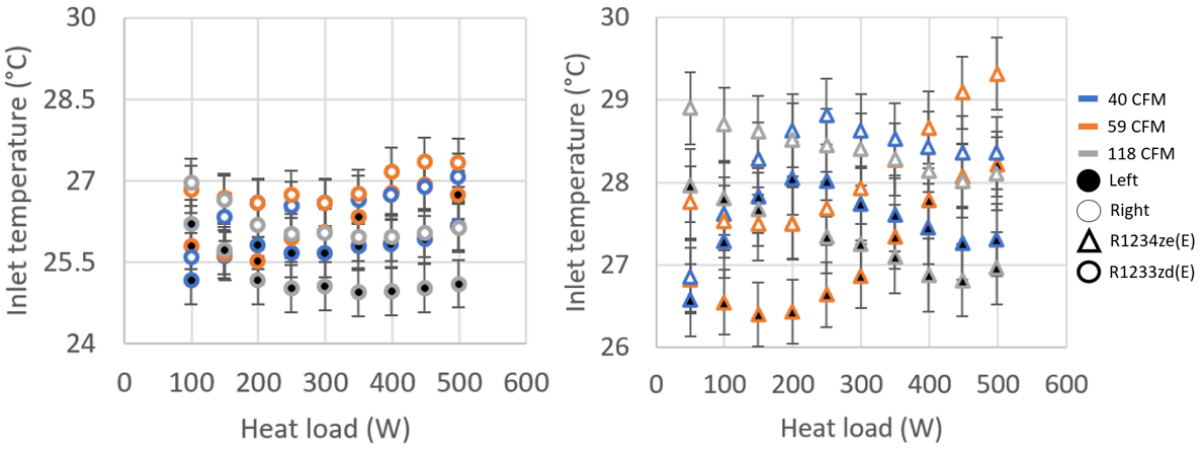

Figure 52 - Inlet air temperature values for all experimental campaign under optimum filling ratio with the R2133zd(E) and R1234ze(E)..

5.2.2.2 Pressure and saturation temperature

The measured pressure, as well as the corresponding saturation temperature for each of the working fluids, are shown in Figure 53. The saturation temperature was back calculated from the pressure through the working fluid saturation pressure curve in the CoolProp database [17].

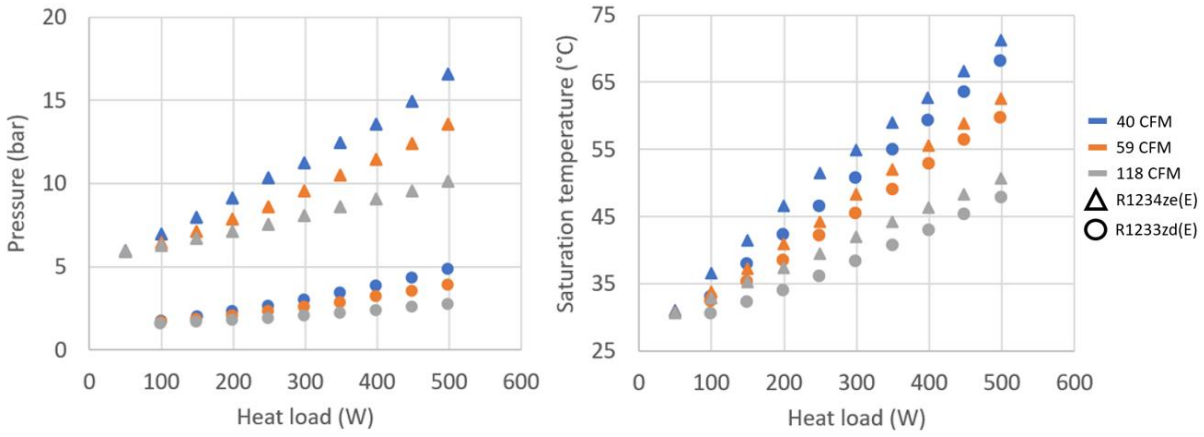

Figure 53 - Comparison of the pressure and saturation temperature values for testing at optimum filling ratio with the R2133zd(E) and R1234ze(E) charges.

The saturation temperatures are similar, with the saturation temperature for R1234ze(E) about 3-5°C higher. This appears to be in contradiction with the results presented in the filling ratio analysis (Subsection 5.1.2), which showed a lower saturation temperature for this fluid. However, this is easily explained by the different inlet air temperatures for the tests performed with R1234ze(E): while both tests for R1233zd(E) (*viz.* Figure 33 and Figure 53) were performed at about the same ambient temperature (26.5°C), the filling ratio analysis tests for R1234ze(E) (Figure 33) was performed at 24.7°C, while the test at constant FR (Figure 53) was performed at 28.7°C. The latter will naturally have a higher junction temperature, and therefore higher overall temperatures in the LTS. In fact, if the thermal resistance is the same, a higher inlet air temperature results in a higher junction temperature by about the same difference:

$$T_{Junction} = q_{cond} * TR_{LTS+TIM} + T_{Air,in} \tag{19}$$

Comparing Figure 53 with Figure 33, for the same conditions (*e.g.* 51% FR, 59 CFM, 500 W), it is easy to verify that the saturation temperature is the same for R1233zd(E), but is about 4ºC higher for R1234ze(E) (coherent with the 4°C higher ambient temperature).

5.2.2.3 Junction temperature

The junction temperature, whose calculation procedure and concept are described in point 5.1.1.3, is plotted, for each of the working fluids, as a function of the filling ratio in Figure 54.

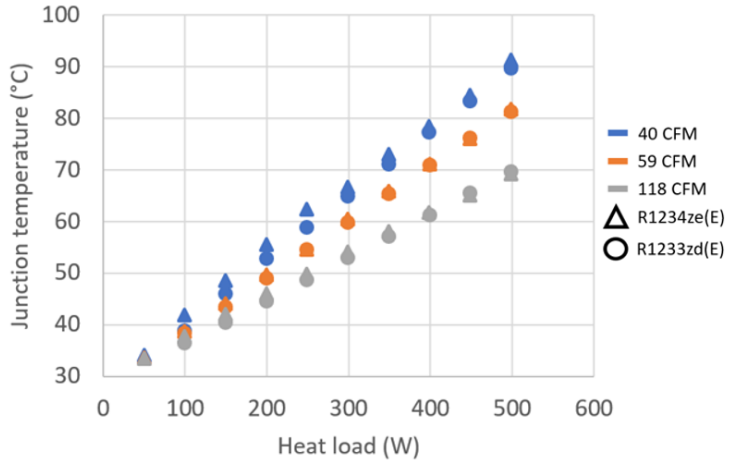

Figure 54 - Comparison of the junction temperature values for testing at optimum filling ratio with the R2133zd(E) and R1234ze(E) charges.

The junction temperature appears to be similar for both fluids. However, as mentioned in the previous point, the ambient temperature is about 4°C higher for the R1234ze(E) test, indicating that the junction temperature would likely be lower for this fluid if the tests had been performed at that ambient temperature. A proper comparison can only be done with the thermal resistance (next point).

5.2.2.4 Thermal resistance

The concept and calculation process of the thermal resistance are described in point 5.1.1.4. The thermal resistance values are shown, for both working fluids, in Figure 55.

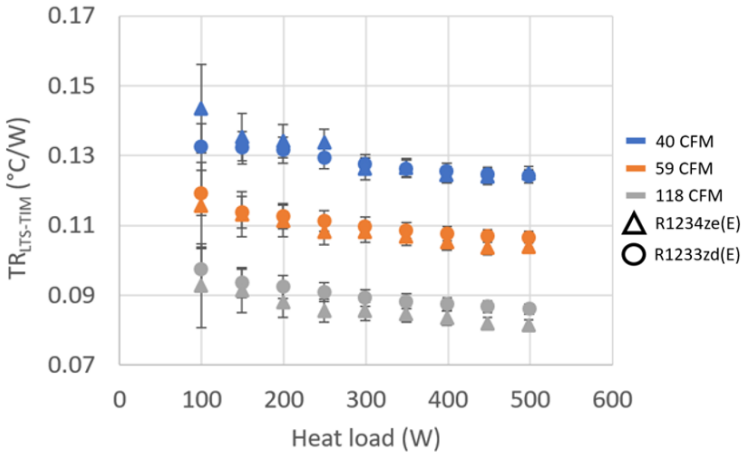

Figure 55 - Comparison of thermal resistance values for testing at optimum filling ratio with the R2133zd(E) and R1234ze(E) charges.

The thermal resistance is generally lower for R1234ze(E), at least for 59 and 118 CFM of air volumetric flow rate. For lower air volumetric flow rates (40 CFM), the value seems to be the same, or slightly higher. This might be due to several factors, one of which is the lower viscosity of R1234ze(E), resulting in less flow resistance. However, the liquid density of R1234ze(E) is lower than R1233zd(E), which would also reduce the driving force for fluid circulation inside the LTS (Eq. 20), reducing the

mass flow rate and hindering the heat transfer. And, as discussed in Chapter 1, the heat transfer in the evaporator is not only dependent on the mass flow rate, but also on the vapour quality, among other factors. Therefore, a detailed analysis of all these factors would be necessary in order to explain why the thermal resistance is lower for one of the fluids in some cases, and higher in others.

The thermal resistance decreases with increasing heat load. Additionally, for an air volumetric flow rate of 40 CFM, the thermal resistance plateaus above 300 W of heat load. This might indicate the beginning of transition from GDR to FDR.

5.2.2.5 LTS air side (left and right side increase in temperatures)

The increase in air temperature on each side of the LTS, as well as the difference between these two, as mentioned in point 5.1.1.5, are shown in Figure 56 for both working fluids. The thermocouples' location is shown in Figure 22.

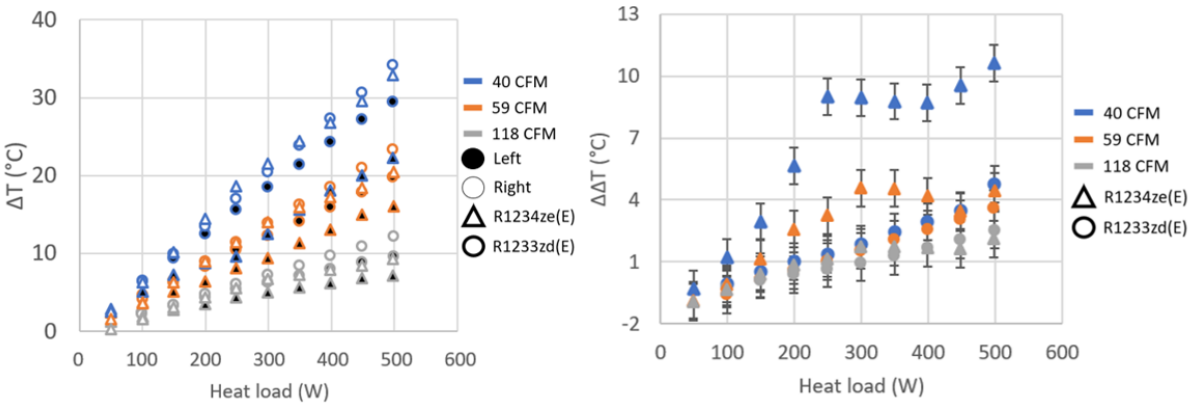

Figure 56 - Comparison of the right and left side temperature increase (left plot), and right minus left side difference of the temperature increase (right plot), for testing at optimum filling ratio with the R2133zd(E) and R1234ze(E) charges.

The results are generally similar and expected, with the right side heating the air more than the left side. However, for 40 CFM of air volumetric flow rate, the air heats much less on the left side, for R1234ze(E) (about 5-7°C less). Similarly, for 40 and 59 CFM of air volumetric flow rate, and unlike all other previous test results, the difference between the right and left sides stops increasing around 250 W.

Clearly the results show a higher thermal performance for the right side of the LTS, as was observed in the working fluid charge determination analysis.

5.2.2.6 Risers

The thermocouples' location and the measured temperatures for the two working fluids are shown in Figure 25 and Figure 57, respectively.

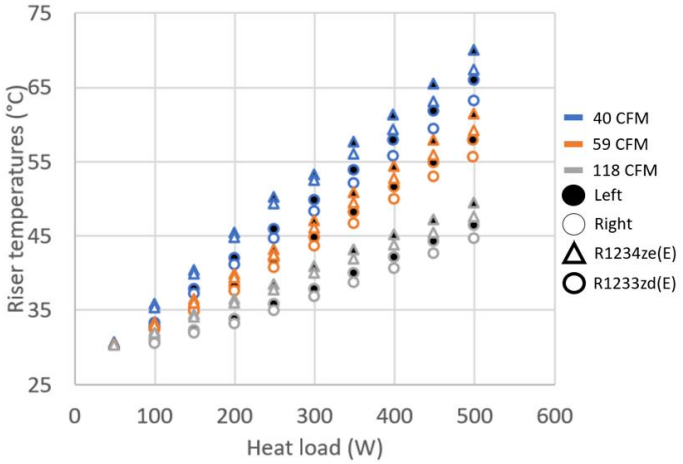

Figure 57 - Comparison of the bottom riser temperature values for testing at optimum filling ratio with the R2133zd(E) and R1234ze(E).

The behaviour is approximately the same for both fluids, with the risers about 3-4°C warmer for R1234ze(E), in line with the other temperatures of the LTS. Also, it can be observed a higher left side riser temperature, which means a lower mass flow rate in that direction.

5.2.2.7 Bottom fins

The thermocouple locations and the measured temperatures of the bottom fins, for each of the working fluids, are shown in Figure 26 and Figure 58, respectively.

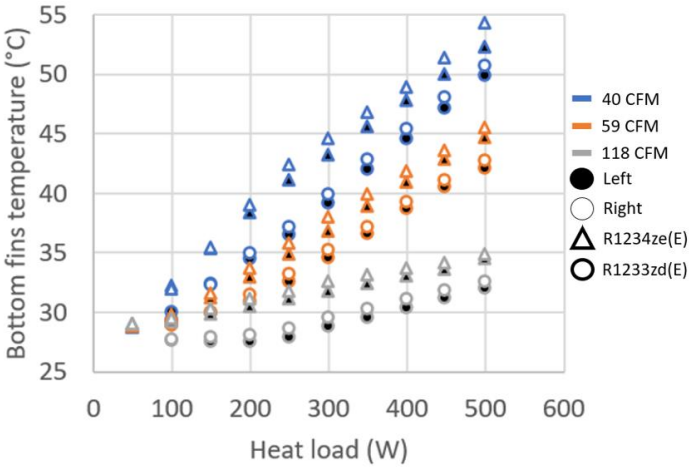

Figure 58 - Comparison of the bottom fins temperature values for testing at optimum filling ratio with the R2133zd(E) and R1234ze(E) charges.

It can be clearly observed higher temperatures for R1234ze(E) (4°C). Also, left side of the LTS shows lower temperatures, which means lower heat being transferred due to non-uniform flow distribution of working fluid between right and left sides.

5.2.2.8 Top fins

The thermocouple locations and the measured temperatures of the top fins of the LTS, for the two working fluids, are shown in Figure 28 and Figure 59, respectively.

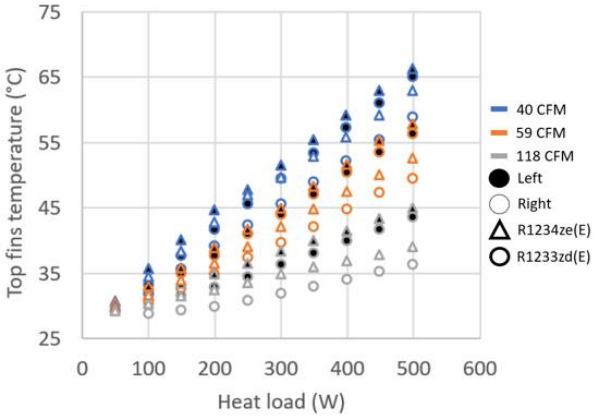

Figure 59 - Comparison of the top fins temperature values for testing at optimum filling ratio with the R2133zd(E) and R1234ze(E).

Again, as was for the bottom fins, higher temperatures are observed for R1234ze(E). Also, left side of the LTS shows lower temperatures, which means lower heat being transferred due to non-uniform flow distribution of working fluid between right and left sides.

5.2.2.9 Downcomer

The downcomer temperature values and the corresponding saturated temperature values (calculated from the pressure) are plotted in Figure 60, for the two working fluids. The location of the thermocouple used for measurement is shown in Figure 30.

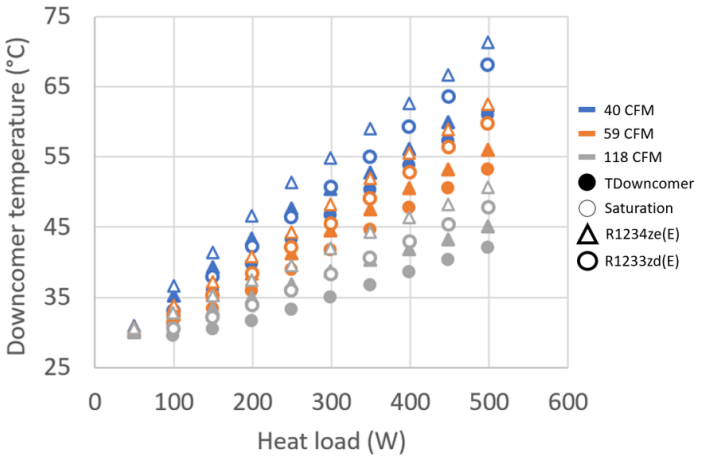

Figure 60 - Comparison of the downcomer and saturation temperature values for testing at optimum filling ratio with the R2133zd(E) and R1234ze(E).

It can be observed a certain level of subcooling for all tests performed (between 1ºC to 10ºC, increasing behaviour with the heat load). Also, higher temperatures for R1234ze(E).

5.2.2.10 Evaporator

The thermocouples' location and the measured evaporator temperatures and corresponding saturation temperatures, for each working fluid, are shown in Figure 61. The thermocouples are attached with tape to the cover plate of the evaporator.

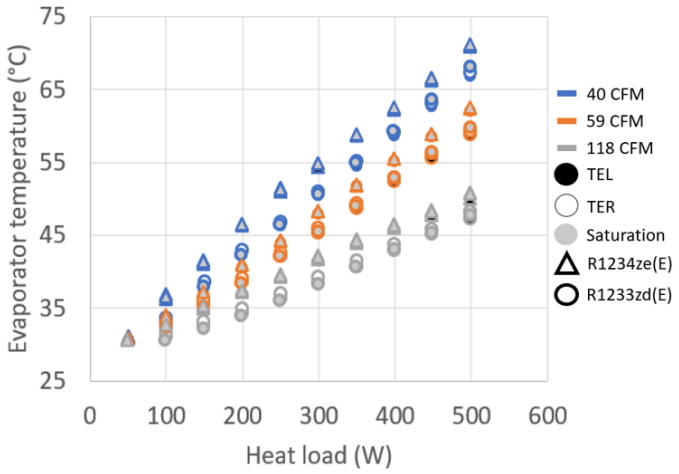

Figure 61 - Comparison of the evaporator and saturation temperature values for testing at optimum filling ratio with the R2133zd(E) and R1234ze(E).

As was already observed in the previous analysis, R1234ze(E) is showing higher temperatures, which means lower thermal performance. Here, also, it can be clearly seen that the working fluid is under saturation conditions for all performed tests.

5.2.3 Results summary

For the analysis presented in Subsection 5.2.1, of the tests performed with a charge of R1233zd(E) at 46% FR, with heat loads up to 700 W and air volumetric flow rates between 89-178 CFM, it was concluded that the saturation temperature, and therefore the pressure, increases with increasing heat load, and the junction temperature increases almost linearly under constant inlet air volumetric flow rate. This is due to the fact that the thermal resistance remains within a relatively narrow range, between 0.08 and 0.11°C/W. The higher end of this range is for lower heat loads, while the lower end of this range applies to heat loads above 500 W (31.3 W/cm^2). The reason for a lower thermal resistance for higher heat loads is probably related to the increase of internal mass flow rate.

The riser temperatures are similar on both sides of the LTS, with a slightly higher temperature (3°C) on the left side.

The top fins' temperatures are warmer than the bottom ones. This might be either due to the fact that the bottom fins' temperatures are measured much closer to the downcomer than the top fins' temperatures. The left-side top fins are also consistently warmer (up to 6-7°C) than the right-side ones, and follow a behaviour similar to the risers'.

The air appears to heat more on the right side of the LTS, although the difference is modest

(up to 4-5°C). This difference also increases for increasing heat loads. A possible explanation is that blockages in the left side of the LTS cause the mass flow rate inside the LTS to increase more in the right side than in the left, for increasing heat loads.

Finally, the downcomer is subcooled as had been previously observed, but now it was possible to determine that the higher the heat load, the greater the subcooling. This is likely due to condenser flooding, resulting from the accumulation of liquid in the condenser MPTs in order to accommodate the higher mass flow rate in the system at higher heat loads. The relatively low asymmetry in air heating and the low thermal resistance, coupled with a uniform temperature in the evaporator, point to a good, uniform performance of the LTS at 46% filling ratio.

For the other two tests performed within the ideal filling ratio range (Subsection 5.2.2), comparing the two working fluids, the results and trends were similar to the tests performed at 46% FR and a charge of R1233zd(E), regardless of the working fluid or air volumetric flow rate. The air also appears to heat more on the right side of the LTS, with this unbalance increasing for increasing heat loads. At 40 CFM of air volumetric flow rate, however, the difference is modest for the tests performed with R1233zd(E) (4-5°C), but is much higher for R1234ze(E) (up to 11°C), unlike what had been observed in the filling ratio analysis (Subsection 5.1.2), and contradicting the overall slightly better performance of R1234ze(E) for other air volumetric flow rates.

The evaporator temperature is uniform and very similar in all cases. All thermal resistances are within 0.08-0.15°C/W, with lower values for higher heat loads and air volumetric flow rates. The saturation and junction temperatures are essentially the same, resulting in a much higher pressure for R1234ze(E). For this fluid, the decrease in thermal resistance for 40 CFM of air volumetric flow rate reaches a plateau after 300 W, which might indicate the beginning of transition from GDR to FDR.

In order to better analyse the difference in performance between the two fluids, it is necessary to know their thermophysical properties (Table 6).

Table 6 - Thermophysical properties for R1233zd(E) and R1234ze(E), at 55ºC and saturation *[17].*

Fluid	**R1233zd(E)**	**R1234ze(E)**
$\boldsymbol{\rho_l\ (kg/m^3)}$	1186.4	1053.7
$\boldsymbol{\rho_g\ (kg/m^3)}$	18.1	61.3
$\boldsymbol{C_{p,l}\ (Jkg^{-1}K^{-1})}$	1272.2	1523.3
$\boldsymbol{C_{p,g}\ (Jkg^{-1}K^{-1})}$	911.0	1156.0
$\boldsymbol{\Delta h_{vap}\ (J/kg)}$	174327	140747
$\boldsymbol{\mu_l\ (Pa.s)}$	0.00032	0.00013
$\boldsymbol{\mu_g\ (Pa.s)}$	0.000012	0.000014

The two fluids have mostly similar properties, except for the liquid phase density (ρ_l), which is lower for R1234ze(E), the gaseous phase density (ρ_g), which is much higher for R1234ze(E), and the liquid viscosity, which is much lower for this same fluid. The higher density of the gaseous phase and lower density of the liquid phase may imply a smaller driving force to maintain the circulation in the thermosyphon:

$$\Delta P_{driver} = (\rho_{downcomer} - \rho_{riser})gh = \Delta P_{friction} + \Delta P_{momentum} \quad (20)$$

Since $\rho_{downcomer}$ is the same as the liquid density, this lowers the driving force for R1234ze(E). On the other hand, the viscosity of R1234ze(E) is about three times smaller than for R1233zd(E), which would reduce the frictional pressure drop, $\Delta P_{friction}$, increasing the circulation. There are, therefore, several factors that might cause the performance for R1234ze(E) to be superior to R1233zd(E) in some cases and worse in others. For example, there is a generally more uniform behaviour of the LTS with the R1234ze(E) charge, with less loss of performance in the left side for filling ratios of 60-70% (see Subsection 5.1.2). There is also, generally, a lower thermal resistance for this fluid (see Subsection 5.2.2), especially for higher air volumetric flow rates (Figure 55). On the other hand, for lower air volumetric flow rates (40 CFM), there seems to be a more asymmetrical heating of the air for R1234ze(E) (Figure 56), while the thermal resistance becomes slightly higher for this fluid (Figure 55).

A detailed analysis of all these factors, as well as other factors (such as the vapour quality and type of regime) would be necessary in order to explain the differences in performance between the two fluids.

5.3 Energy balance

In order to have reliable analysis of the results, it is important to have not only calibrated instruments for temperature and pressure measurements, but also accurate values for heat load applied to the system. It is important for a correct calculation of thermal resistance.

The heat load can be estimated by three different methods: i) applied voltage and current of a power supply; ii) vertical temperature gradient in the copper block (Fourier's Law) and iii) energy balance on the air flow. In the first case, the power is given by:

$$q_{power\ supply} = UI \tag{21}$$

where *U* and *I* are the voltage and current applied by the power supply to the cartridge heaters.

In the second case, the heat load can be estimated byFourier's law for unidirectional conduction along the copper block (Figure 62):

$$q_{copper\ block} = k_{Cu} A_{block} \frac{TBot - TTop}{L_{cond}} \tag{22}$$

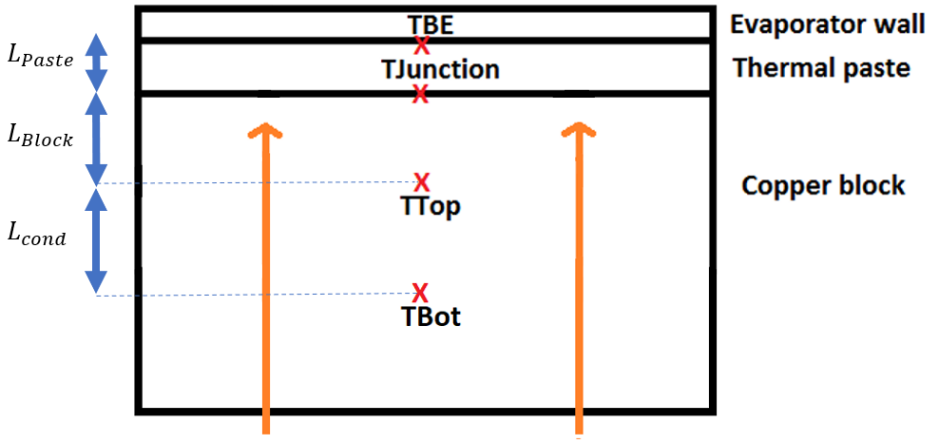

Figure 62 - Scheme of the temperatures inside the copper block used to compute the heat flow.

Finally, through the air side energy balance:

$$q_{air} = \dot{m} C_p (\bar{T}_{out} - \bar{T}_{in}) = v_{air} * \rho_{air,out} * A_{anem.} * C_p (\bar{T}_{out} - \bar{T}_{in}) - P_{fan} \tag{23}$$

The air velocity (v_{air}) is acquired by an anemometer (Testo T480 probe), the density ($\rho_{air,out}$) and the isobaric heat capacity C_p are computed using the CoolProp database. The cross-section area ($A_{anem.}$) of the anemometer is 78.5 cm^2.

Figure 63, Figure 65 and Figure 64 show, for each set of performed tests at a fixed filling ratio, the difference between $q_{copper\ block}$ and $q_{power\ supply}$, as well as between q_{air} and $q_{power\ supply}$.

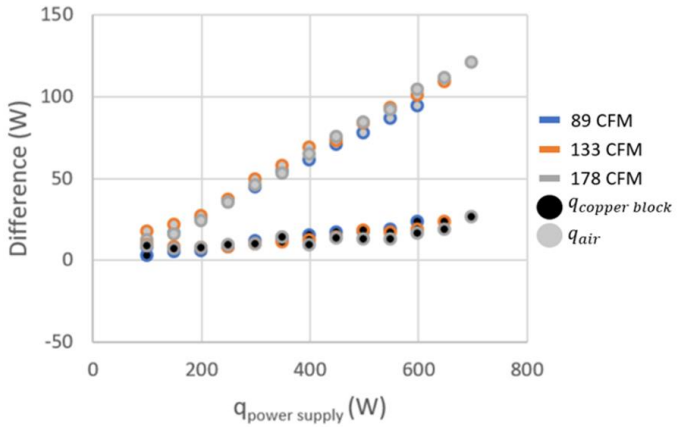

Figure 63 - Values of $q_{copper\ block} - q_{power\ supply}$ (black-filled circles), and $q_{air} - q_{power\ supply}$ (grey-filled circles) for tests with R1233zd(E) at 46% FR.

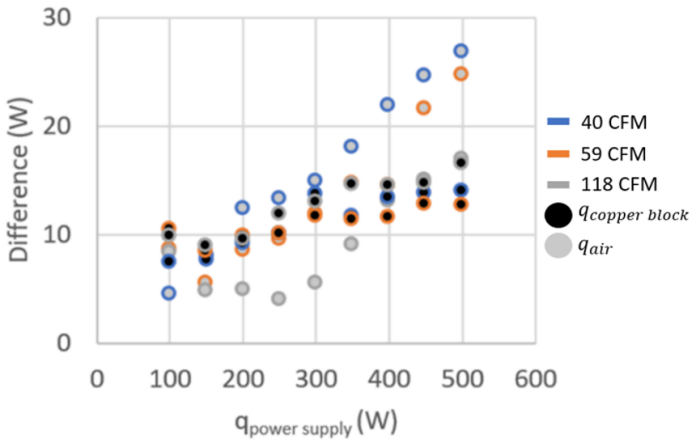

Figure 64 - Values of $q_{copper\ block} - q_{power\ supply}$ (black-filled circles), and $q_{air} - q_{power\ supply}$ (grey-filled circles) for tests with R1233zd(E) at 41% FR.

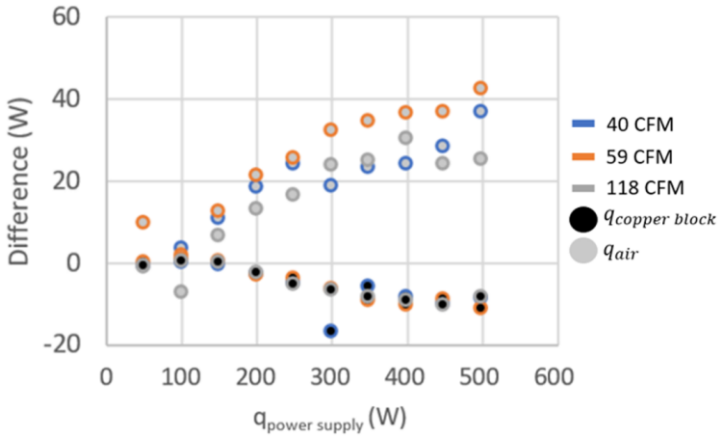

Figure 65 - Values of $q_{copper\ block} - q_{power\ supply}$ (black-filled circles), and $q_{air} - q_{power\ supply}$ (grey-filled circles) for tests with R1234ze(E) at 51% FR.

The heat load calculated from the copper block vertical gradient ($q_{copper\ block}$) shows small differences relative to the power supply (below 5% of the applied values, which can be due to overall system heat losses). However, the heat load values calculated through the air-side energy balance (q_{air}) show considerable larger differences, which increases with increasing heat load. Thus, it clearly seems that air velocity measured by the anemometer is overestimated.

Although this overestimation seems to show a linear behaviour for the tests performed for R1233zd(E) at 46% FR, which were performed at higher air volumetric flow rates (Figure 63), the behaviour does not seem as predictable for other tests (Figure 64 and Figure 65), which were performed at lower air volumetric flow rates. which were performed at lower air volumetric flow rates. Thus, a more detailed analysis including the influence of other factors, like air temperature and filling ratio, would be necessary to accurately characterise this error.

5.4 Copper block temperature distribution

A total of seven thermocouples were located 2 mm below the surface of the heated copper block which mimics a CPU surface (*viz.* Figure 14). There was, in addition, a thermocouple in the centre of the copper block, 8 mm below the surface (*TBot,* Figure 8 and Figure 62). Throughout the testing campaign, the central thermocouples *TTop* and *TBot* were considered to compute the junction temperature (vertical 1-dimensional heat flux is assumed through the copper block). In order to confirm this assumption, an analysis of the surface temperatures of the copper block was performed (Figure 66).

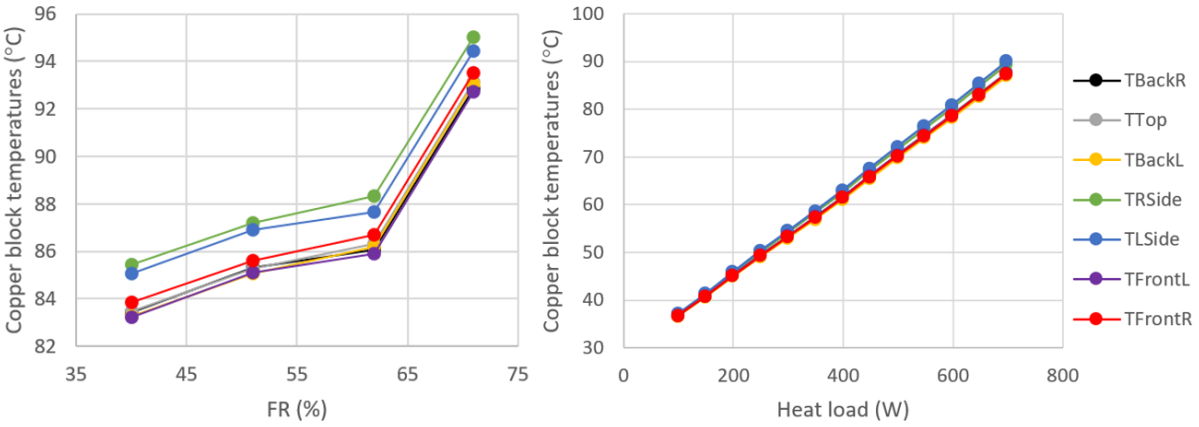

Figure 66 - Copper block footprint temperatures (legend names correspond to the thermocouples under the copper block surface, *viz.* Figure 14). Left plot: filling ratio analysis for R1233zd(E), 500 W and 59 CFM. Right plot: R1233zd(E) at 46% FR and 178 CFM, from 0 to 700 W of heat load

It was verified that the lateral thermocouples (*TRSide* and *TLSide*) of the copper block present slightly higher temperatures (1-2°C) than the remaining thermocouples, for all filling ratios, air volumetric flow rates and heat loads. Therefore, the temperature distribution of the copper block is similar for all test conditions. Slightly different temperatures near the junction are normal, since the vapour quality varies along the evaporator, changing the local heat transfer coefficient in different parts of the evaporator.

5.5 Transient behaviour

In addition to the previous analyses, which aimed to evaluate the behaviour of the LTS at different steady-states, an analysis of its transient behaviour was also performed. In this subsection, several cases are analysed and discussed, namely instants when the heat load was increased and/or the air volumetric flow rate reduced.

5.5.1 Cold start-up

A cold start-up from 0 to 600 W was performed under the conditions of the first optimum charge test (Subsection 5.2.1), for 89 CFM of inlet air flow. The LTS and copper block temperatures, pressure/saturation temperature and the transient heat load (calculated from Eq. 22) are shown in Figure 67, Figure 68 and Figure 69.

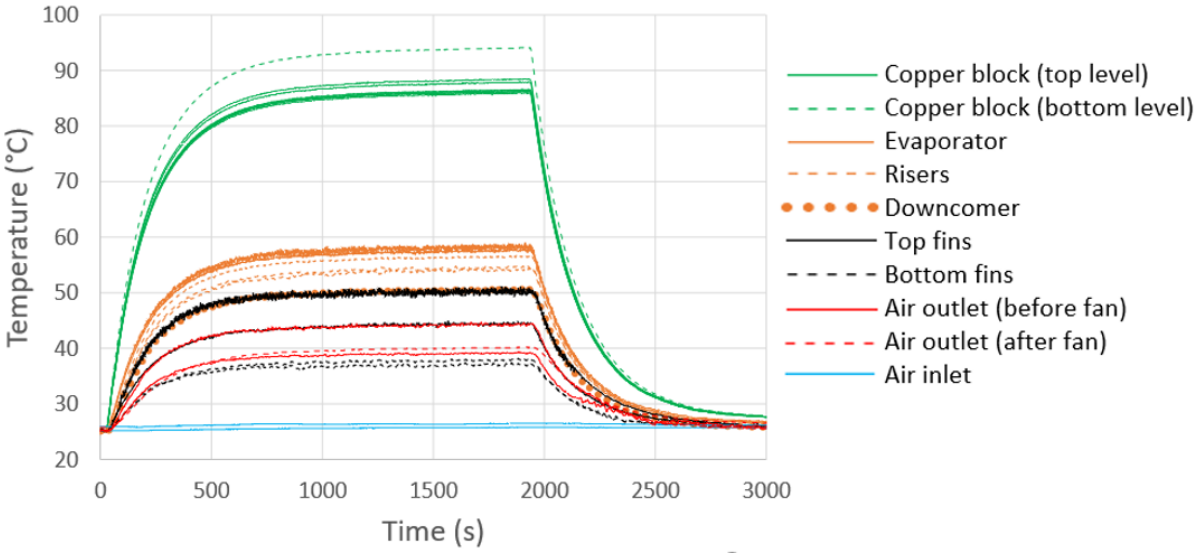

Figure 67 - Copper block and LTS temperatures for a cold start-up to 600 W, 89 CFM of inlet air volumetric flow rate and a charge of R1233zd(E) at 46% FR.

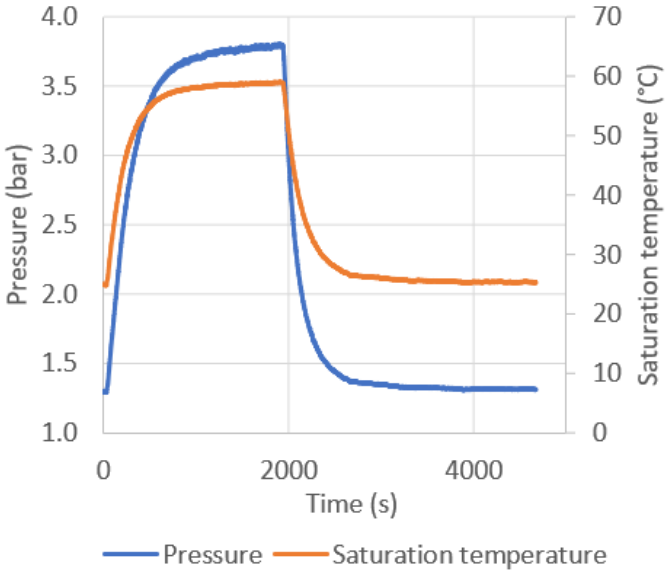

Figure 68 - Pressure and saturation temperature for a cold start-up to 600 W, 89 CFM of inlet air volumetric flow rate and a charge of R1233zd(E) at 46% FR.

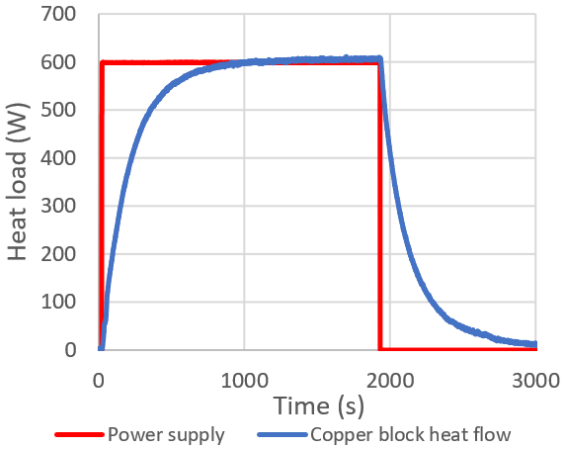

Figure 69 - Transient heat load inside the copper block for a cold start-up to 600 W, 89 CFM of inlet air volumetric flow rate and a charge of R1233zd(E) at 46% FR.

It can be observed that the temperatures in the different locations of the LTS increase steadily until they reach a stationary state, without major disturbances, trend reversals or instabilities. Thus, showing the optimal thermal behaviour of the LTS (behaviour observed for filling ratios below 60%). The behaviour above 60% FR, as well as other exceptions are analysed in the next Subsections.

5.5.2 Drop in left side performance

Figure 70 shows the measured temperatures of the LTS (*viz.* Figure 8 and Figure 9) for a cold start-up with a charge of 70% FR, for each of the working fluids tested.

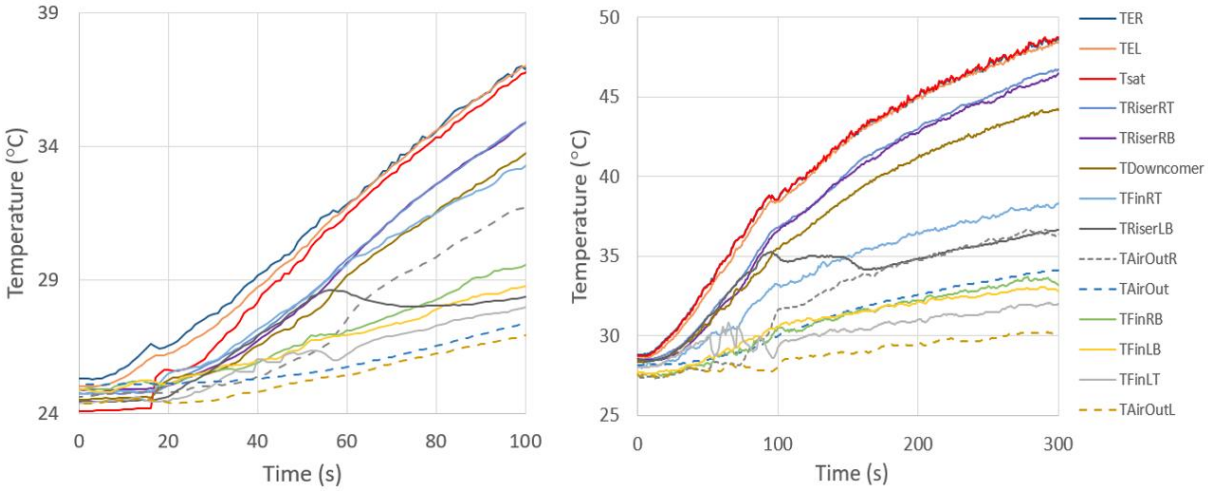

Figure 70 - LTS temperatures (legend tags are the thermocouples in Figure 8 and Figure 9) for a cold start-up from 0 W to 500 W of heat load and 70% FR. Left plot: R1233zd(E) at 59 CFM air volumetric flow rate. Right side: R1234ze(E) and 40 CFM air volumetric flow rate.

For both fluids, under very similar conditions, there is an abrupt drop in the left riser temperature in the early stages of the start-up (between 60-100 s). This indicates that the circulation of the fluid has stopped or decreased in the left side, as had been previously suggested from the filling ratio analysis (Section 5.1). However, for R1233zd(E), this drop occurs when the transient heat load (calculated from Eq. 22) is around 150 W, while for R1234ze(E) this happens at 250 W.

5.5.3 Instabilities and oscillations

Figure 71 shows the LTS temperatures (*viz.* Figure 8 and Figure 9) for a step increase from 0 to 150 W of heat load, and then to 300 W, for a charge of R1233zd(E) at 80% FR and an inlet air volumetric flow rate of 95 CFM.

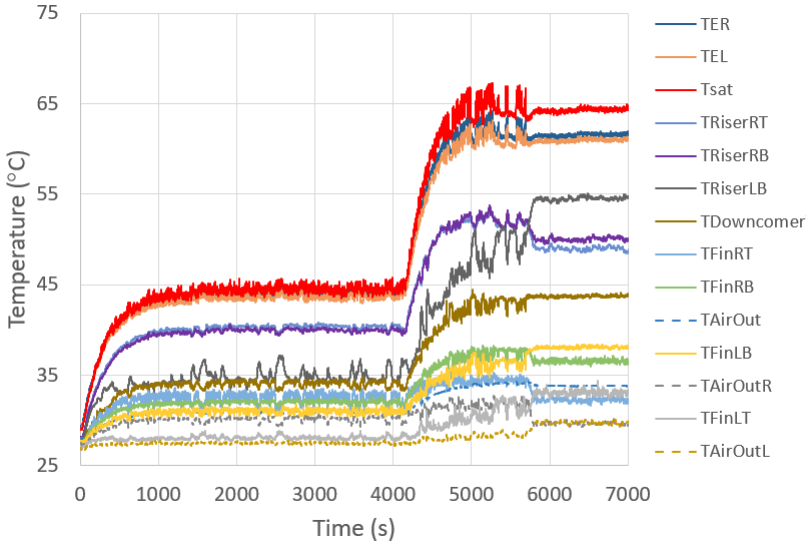

Figure 71 - LTS temperatures (legend names are thermocouples, viz. Figure 8 and Figure 9) for a cold start-up to 150 W, and then an increase to 300 W, for a charge of R1233zd(E) and 95 CFM of inlet air volumetric flow rate, for a filling ratio of 80%

For a heat load of 150 W, and especially for the transition to 300 W, a much more unstable behaviour is observed than for the steady state at 300 W. There is a clear increase in instability when increasing the heat load from 150 W to 300 W. There are also more oscillations at the 150 W power level than at 300 W. These instabilities are mild, however, and do not impact the overall performance of the system.

6. X-Ray microtomography analysis

As highlighted along of this study, a lower thermal performance of the LTS was observed in his left side. It was basically due to the lower increasing in air temperature on that side, and consequently a potential partial clogging of the MPT channels in that side (lower working fluid mass flow rate). Thus, to evaluate and justify such differences, an x-ray microtomography scan of the whole LTS was performed using the *UltraTom Ultra High Performant 3D CT System* [19], with a resolution of 585 *μm*. The working principle of the X-ray microtomography is schematically shown in Figure 72.

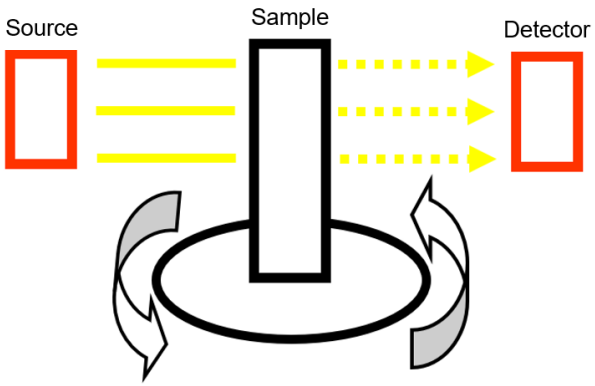

Figure 72 - Schematic of the working principle of x-ray microtomography.

An X-ray source of 130-260 kV beams the radiation through the sample (LTS), which is then captured by a detector. The sample is continuously rotated in order to allow for a 3D-image to be generated by computing together all the 2D prints captured by the detector. The results are three sets of slices, along the three axes, showing the inside of the LTS.

The orientation of the axes considered for this analysis is shown in Figure 73.

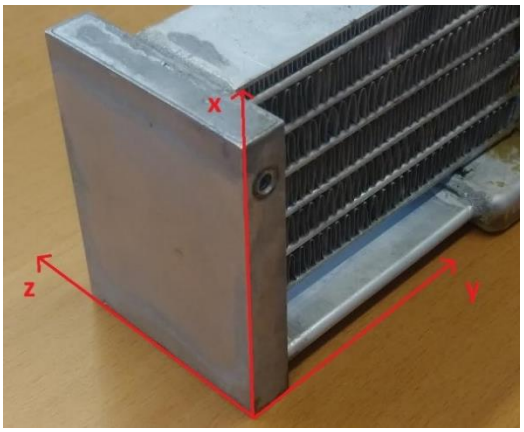

Figure 73 - Axis system used for the microtomography analysis.

The visualisation along the *z* axis showed that the bottom MPTs, on both sides, are blocked. An example of blockages and restrictions in the MPTs, along the *y* axis, is shown in Figure 75.

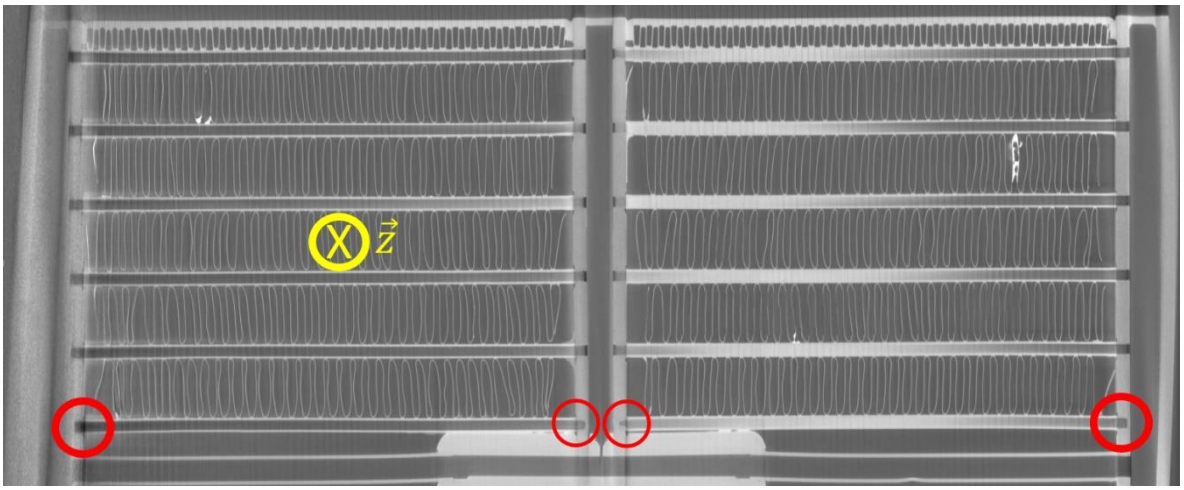

Figure 74 - View along the *z* axis, showing the blockages in the lower multiport tubes (in the red circles).

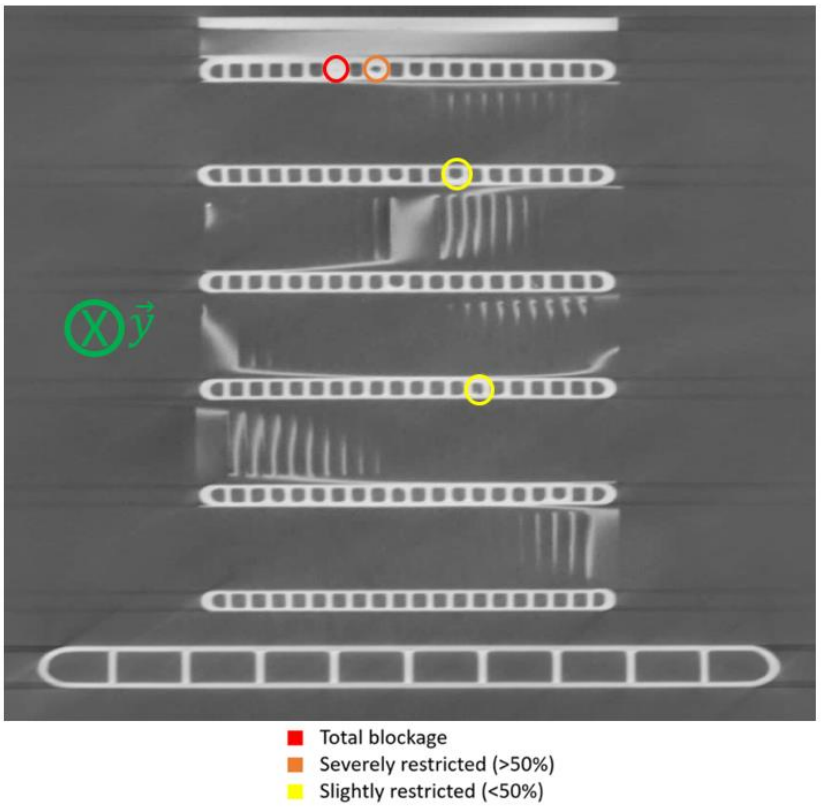

Figure 75 - Slice showing blockages and restrictions along the *y* axis.

When evaluating the LTS through the *y* direction, it was possible to compile all blockages and restrictions in the multiport tubes. These restrictions are schematically shown in Figure 76, through a colour code, to distinguish the severity of the blockage.

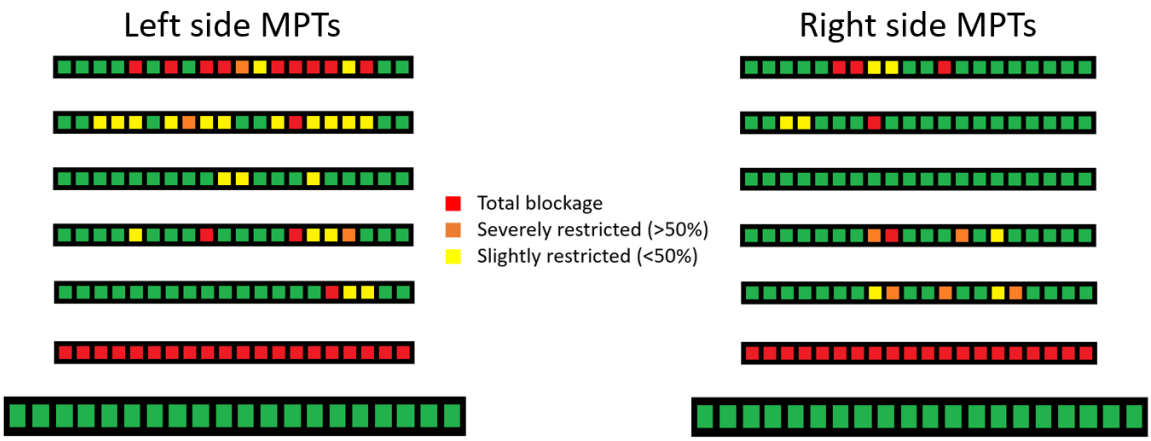

Figure 76 - Compilation of all the blockages and restrictions found after going through the whole LTS in the *y* direction.

In addition to the lower MPTs being completely blocked, it was possible to conclude that the left side MPTs have more blocked channels, especially near the top, than the right side MPTs. The left side also shows more restrictions (without blockage) in lower MPTs. This corroborates the hypothesis, put forward previously, that restrictions in the left side, causing a lower effective thermosyphon height and higher pressure drop, caused a decrease in performance of the LTS in the left side. As this is the first-ever prototype of this newly developed thermosyphon cooling unit, in the future steps can be made to eliminate the blockage of the microchannels during the fabrication process; this portends to even better thermal performance (higher possible heat loads) and lower thermal resistances in the future.

Thus, it can be concluded that a much higher thermal-hydraulic performance LTS system can be obtained if no clogging is to be observed.

7. Conclusions and recommendations

The experimental evaluation of the prototype loop thermosyphon cooling device allowed to confirm its ability to dissipate up to 700 W of power (43.8 W/cm^2), without reaching temperatures above 90°C in the copper block surface (pseudo-chip surface). A thermal resistance as low as 0.081°C/W was reached for the optimal working fluid charge (40-60% FR) and highest values of heat load. In fact, it was observed that the thermal resistance decreased with increasing heat load, which potentially indicates the increasing of working fluid mass flow rate with heat load and thus that the LTS is in GDR mode. Additionally, for low heat loads, a more abrupt decreasing in thermal resistance was noted, which might be related with the transition from slug flow to annular flow [15].

It was also possible to verify that the downcomer temperature was significantly below than the saturation temperature, meaning a desired subcooling at the inlet of evaporator which helps to avoid issues of instabilities and backflow in this component.

The transient analysis of the LTS under an increased step in heat load showed a fast and stable response. Negligible instabilities were observed only for low levels of heat load and high filling ratios.

Throughout the experimental campaign, in addition to determining the optimum working fluid charge (between 40 and 60% FR), it was possible to verify significant asymmetries in the performance of the LTS. That is, for certain filling ratios (including the optimum working fluid charge), the temperatures on the left side of the LTS showed to drop abruptly. It was also observed that the right side of the LTS transferred more heat to the air than the left side, with the difference increasing for higher heat loads. Thus, the thermal results suggested partial working fluid flow blockages in the MPTs at the left side of the LTS, which was verified through an X-ray microtomography test.

In summary, the results showed that a compact, small-footprint, passive thermosyphon system is able to cool up to 700 W of power, even with some prototype manufacturing defects that impacted its performance. Furthermore, in addition to savings in electrical power consumption (when compared with heavy heat spreaders using high power consumption fans), the temperatures involved are relatively high (up to 80°C), which could allow for some degree of heat recovery.

Finally, based on the energy efficiency potential of these emerging cooling systems, it is expected a significant growth over the next decade, both in new novel prototyping and development of simulation and prediction tools. Thus, further experimental work, with different working fluids and improved prototypes, is expected as a continuation of the present study. In addition to the already developed simulation tools for the LTS, updates could be considered to evaluate the effects of flow restrictions and filling ratios on the LTS thermal-hydraulic performance.

8. References

[1] N. Lamaison, C. L. Ong, J. B. Marcinichen and J. R. Thome, “Two-phase mini-thermosyphon electronics cooling: Dynamic modeling,experimental validation and application to 2U servers,” *Applied Thermal Engineering,* vol. 110, pp. 481-494, 2017.

[2] E. Costa-Patry, “Cooling High Heat Flux Micro-Electronic Systems using Refrigerants in High Aspect Ratio Multi-Microchannel Evaporators,” École Polytechnique Fédérale de Lausanne, 2011.

[3] Y. Taltel and D. Barnea, “Modelling of Gas Liquid Flow in Pipes,” in *Encyclopedia of Two-Phase Heat Transfer and Flow I - Fundamentals and Methods*, vol. 1, World Scientific, 2016.

[4] R. Revellin, V. Dupont, T. Ursenbacher, J. R. Thome and I. Zun, “Characterization of diabatic two-phase flows in microchannels: Flow parameter results for R-134a in a 0.5 mm channel,” *International Journal of Multiphase Flow,* vol. 32, pp. 755-774, 2006.

[5] N. Kattan, J. R. Thome and D. Favrat, “Flow Boiling in Horizontal Tubes: Part 1 – Development of a Diabatic Two-Phase Flow Pattern Map,” *Journal of Heat Transfer,* vol. 120, pp. 140-147, 1998.

[6] N. Lamaison, C. L. Ong, J. B. Marcinichen and J. R. Thome, “Two-Phase Thermosyphon Cooling of Datacenters,” in *Encyclopedia of Two-Phase Heat Transfer and Flow III - Macro and Micro Flow Boiling and Numerical Modeling Fundamentals*, Vols. 3 - Micro-Two-Phase Cooling Systems, World Scientific, 2018.

[7] J. Bieliński and H. Mikielewicz, “Natural Circulation in Single and Two Phase Thermosyphon Loop with Conventional Tubes and Minichannels,” in *Heat Transfer - Mathematical Modelling, Numerical Methods and Information Technology*, vol. 19, InTech, 2011, pp. 475-496.

[8] S. Manova, L. G. Asirvatham, R. Nimmagadda, J. R. Bose and S. Wongwises, “Cooling of high heat flux electronic devices using ultra-thin multiportminichannel thermosyphon,” *Applied Thermal Engineering,* vol. 169, 2020.

[9] A. A. M. Junior and M. B. H. Mantelli, “Thermal performance of a novel flat thermosyphon for avionics thermal management,” *Energy Conversion and Management,* vol. 202, 2019.

[10] Y. Liu, Z. Li, Y. Li, Y. Jiang and D. Tang, “Heat transfer and instability characteristics of a loop thermosyphon withwide range offilling ratios,” *Applied Thermal Engineering,* vol. 151, pp. 262-271, 2018.

[11] C. Tecchio, J. Oliveira, K. Paiva, M. Mantelli, R. Galdolfi and L. Ribeiro, “Geyser boiling phenomenon in two-phase closed loop-thermosyphons,” vol. 111, no. International Journal of Heat and Mass Transfer, pp. 29-40, 2017.

[12] P. T. Garrity, J. F. Klausner and R. Mei, “Instability phenomena in a two-phase microchannel thermosyphon,” *International Journal of Heat and Mass Transfer,* vol. 52, pp. 1701-1708, 2009.

[13] A. Chauhan and S. G. Kandlikar, “Characterization of a dual taper thermosiphon loop for CPU cooling in data centers,” *Applied Thermal Engineering,* vol. 146, pp. 450-458, 2019.

[14] M. M. Ohadi, S. V. Dessiatoun, K. Choo, M. Pecht and J. V. Lawler, “A Comparison Analysis of Air, Liquid, and Two-Phase Cooling of Data Centers,” in *28th Annual IEEE Semiconductor Thermal Measurement and Management Symposium (SEMI-THERM)*, 2012.

[15] R. L. Amalfi, F. Cataldo and J. R. Thome, “The Future of Data Center Cooling: Passive Two-Phase Cooling,” *Electronics Cooling,* pp. 16-21, Summer 2020.

[16] Keysight Technologies, “Keysight N5700 Series Data Sheet,” 2017.

[17] CoolProp, “CoolProp database,” 2020. [Online]. Available: http://www.coolprop.org/.

[18] Thermal Grizzly, “Thermal Grizzly High Performance Cooling Solutions - Kryonaut,” 2020. [Online]. Available: https://www.thermal-grizzly.com/en/products/16-kryonaut-en. [Accessed December 2020].

[19] RX Solutions, “UltraTom,” 2020. [Online]. Available: https://easytom-ct.com/ultratom/.

[20] Thermometrics, “Type J thermocouple,” 2011. [Online].

[21] YANTRIKA, “YANTRIKA pneumatic dead weight tester,” August 2020. [Online]. Available: http://www.deadweighttester.com/pneumatic-dead-weight-tester.html.

[22] Keller, “Keller PA 33X Pressure transducers datasheet,” 2020. [Online]. Available: https://download.keller-druck.com/api/download/AwGTU9f2z3japojFiKuMSi/en/2020-06.pdf.

[23] J. R. Thome, Encyclopedia of Two-Phase Heat Transfer and Flow III - Vol. 3 Ch. 7, vol. 3, Singapore: World Scientific, 2018, pp. 287-289.

[24] Honeywell, “PTM7000 Series data sheet,” 2016.

[25] F. P. Incropera, Fundamentals of Heat and Mass Transfer, 7th ed., John Wiley and Sons, 2011, pp. 154-161.

[26] Testo, “testo 480 - testo 480 instrumento de medição de alta qualidade para VAC,” 2020. [Online]. Available: https://www.testo.com/pt-PT/testo-480/p/0563-4800.

[27] J. Cao, Z. Zheng, M. Asim, M. Hu, Q. Wang, Y. Su, G. Pei and M. Leung, “A review on independent and integrated/coupled two-phase loop thermosyphons,” *Applied Energy,* vol. 280, 2020.

[28] C. Sarno, C. Tantolin, R. Hodot, Y. Maydanik and S. Vershinin, “Loop thermosyphon thermal management of the avionics of an in-flight entertainment system,” *Applied Thermal Engineering,* vol. 51, pp. 764-769, 2013.

[29] S. M. Mahmoud, R. K. Al-Dadah and A. A. Alammar, “Effect of inclination angle and fill ratio on geyser boiling phenomena in atwo-phase closed thermosiphon–Experimental investigation,” *Energy Conversion and Management,* vol. 156, pp. 150-166, 2018.

[30] J. B. Marcinichen, J. A. Olivier and J. R. Thome, “On-chip two-phase cooling of datacenters: Cooling system and energy recovery evaluation,” *Applied Thermal Engineering,* vol. 41, pp. 36-51, 2012.

9. Appendices

9.1 Appendix A – Thermocouples calibration

Most of the thermocouples used to make the temperature measurements of the loop thermosyphon have been used previously. As such, they needed to be recalibrated against an accurate, known reference for the present tests. These calibrations were then used, in subsequent tests, to convert the real-time measured temperature values into the final temperature values.

9.1.1 Experimental set-up

The thermocouples were separated into bundles and set into place by taping them to an overhead board; the same was done for the Testo T480 reference probe. The thermocouple tips were then inserted into a copper block inside the LAUDA Proline AP885 thermal bath, to reduce the influence of thermal fluctuations (Figure 77).

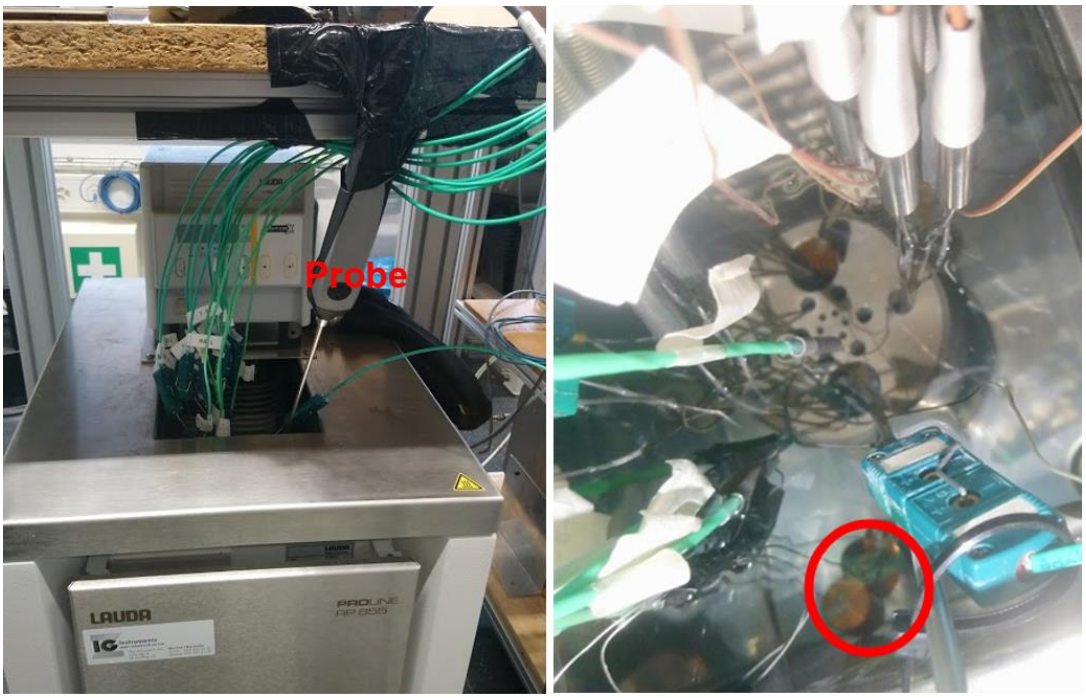

Figure 77 - Overall view of the thermocouple calibration set-up, showing the thermocouples (green wires) and the reference probe inserted into the thermal bath (left). Insertion of the thermocouples/probe into a metal block inside the bath, with the thermocouples soldered to copper blocks outside, in the red circle (right).

Throughout the calibration process, it was verified that the thinner thermocouples, whose tips are covered in an adhesive tape, should not be calibrated in water, as they lose these adhesive properties; it also happened, in some cases, that the thermocouples were damaged and stopped working entirely. On the other hand, using tape to fix the thermocouple wires to the overhead board

has proven not to be adequate, as the steam produced during the calibration condensates in contact with it and causes it to lose its adhesive properties.

9.1.2 Data acquisition and post-processing

The calibration procedure was automated via LabVIEW and NI DAQ system. The thermocouples were connected to the NI SCXI380 Terminal Module, which performs automatic compensation for the effect of the Module's temperature on the voltage generated by the thermocouple. The signal, converted by the DAQ system into a temperature value, is then acquired into the LabVIEW VI, which allows the experimentalist to save the data.

The temperatures of the thermal bath was set in advance in the LabVIEW VI, as well as the time it stays at each temperature within a defined tolerance, and the time it saves the data. The defined thermal bath temperatures followed a scheme such as 90-85-90-80-85-80-75°C, down to 5°C, in order to take into account eventual hysteresis effects; a tolerance of 0.1°C, a settling time of 30 minutes and a measurement time of 1 minute were used for each temperature step. In order for the signals to start being saved, both a fluctuation of less than the tolerance and a time greater than the settling time must have had passed. The water evaporation rate of the thermal bath was particularly high above 75°C. Thus, to avoid issues with low level of water in the thermal bath, the calibration was started at 90°C in the afternoon, being under on-site supervision until it reached 75°C, and was allowed to run overnight, while continuously monitored remotely.

The result was a file with the temperature values of all thermocouples, the reference probe and the bath's own sensor, for each of the temperature steps. This file was then post processed by a MATLAB script: the values for each thermocouple, as well as the reference probe, corresponding to a temperature step were averaged, and, using a least-squares approximation, a linear regression for the temperature probe values as a function of each thermocouple's temperature values was performed, as explained in *Appendix C - Least squares approximation*.

9.1.3 Results

An example of a linear regression for one of the thermocouples is shown in Figure 78. The dashed lines correspond to ±2.2°C, the uncertainty for a type K thermocouple [20].

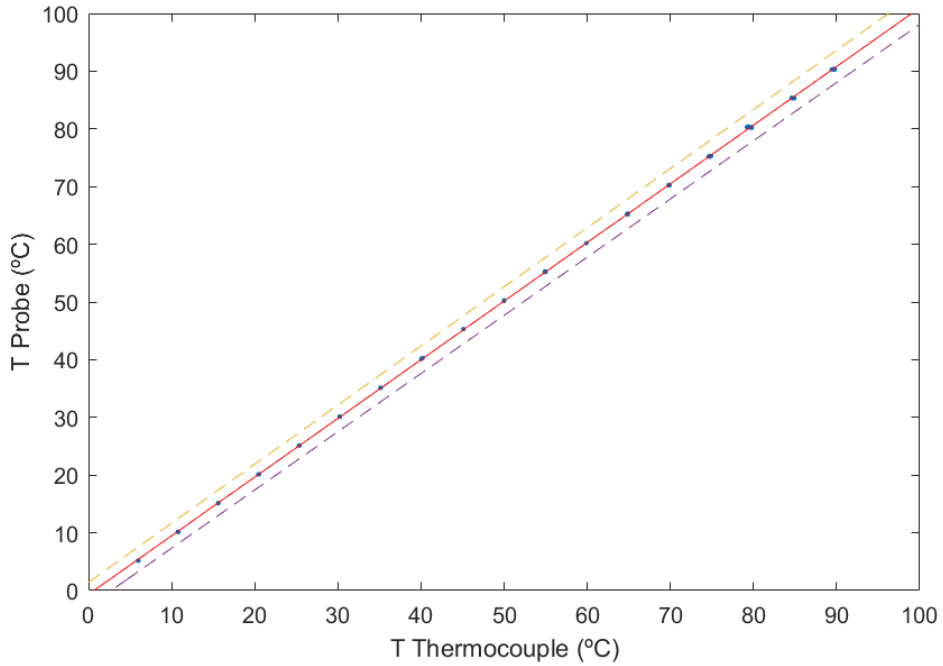

Figure 78 - Example of a thermocouple calibration: the reference probe's temperature as a function of the thermocouple's, showing the linear trendline. The dashed lines correspond to a long-term drift error of ±2.2°C.

This calibration has an accuracy of around ±0.25°C, as setting all the thermocouples at the same temperature and applying the calibration, the difference between them, as well as the probe, was always within ±0.2°C, with the probe itself having an accuracy of ±0.1°C:

$$\varepsilon_{calibration} = \sqrt{\varepsilon_{difference}^2 + \varepsilon_{probe}^2} = \sqrt{0.2^2 + 0.1^2} = 0.25°C \quad (24)$$

In this plot, the dashed lines corresponding to the error assume that the thermocouple can, over time (months/years), indicate a value up to ± 2.2ºC different due to changes in homogeneity [20].

The correlation coefficients for all the calibrated thermocouples are shown in the following table.

Table 7 - Coefficient values for the thermocouples calibration.

Thermocouple	a (slope)	b (intercept)
TAirInL	1.0056	0.07
TAirInR	1.0050	-0.06
TAirOutL	1.0080	-0.04
TAirOutR	1.0083	0.24
TAirOut	1.0110	-0.17
TFinLT	1.0048	0.17
TFinRT	1.0068	0.12
TFinLB	1.0044	0.15
TFinRB	1.0051	0.20
TDowncomer	1.0019	-0.30
TRiserRT	1.0020	-0.05
TRiserRB	1.0022	0.05
TRiserLB	1	0
TEL	1.0016	-0.03
TER	1	0
TBackL	1.0102	-0.03
TBackR	1.0104	-0.08
TLSide	1.0096	0.09
TRSide	1.0093	0.18
TFrontL	1.0085	0.03
TFrontR	1.0080	0.13
TTop	1.0103	0.05
TBot	1.0099	0.05

9.2 Appendix B – Pressure transducer calibration

The pressure transducers were recalibrated for their use in the present tests. Therefore, by saving the output signals of the pressure transducers for known pressures, it was possible to establish a linear relation between the voltage output and the real pressure being measured, for each pressure transducer.

This step was performed after the main tests on the loop thermosyphon, and the pressure signals from those tests were post-processed afterwards.

In order to verify the influence of external variables and troubleshoot problems, several calibrations were done by changing the power supply and the DAQ channels.

9.2.1 Experimental set-up

9.2.1.1 Assembly and leak-proofing

The first step of setting up the calibration system was to properly assemble a structure that could simultaneously hold several pressure transducers and connect them to a single tube.

After assembling this apparatus, it was connected to the YANTRIKA pneumatic dead weight tester (Figure 79), and then the system was leak-proofed using a nitrogen gas bottle at 15 bar.

Figure 79 - Structure for holding the pressure transducers connected to the dead weight tester with the pressure transducers connected to the channels for the data acquisition.

The pressure was then monitored in the LabVIEW VI through the channel connected to one of the transducers. If the pressure seemed to be decreasing slightly, it was checked if the temperature was also decreasing. If it remained inconclusive whether the drop in pressure was due to a leak or not,

the system was left closed for 12 hours and checked for the pressure and temperature in the end.

The weights, cylinder and priming pump (Figure 80) were cleaned with isopropyl alcohol. All debris from the priming pump and excess oil on the cylinder were cleaned as well. Then it was checked, using a level, if the cylinder was perfectly horizontal, making corrections by adjusting the support screws of the dead weight tester.

A leak was found in the cylinder. It was disassembled, cleaned and the oil changed, but the problem could not be completely solved. However, the leak was small, and as it will be mentioned later, by closing the cut-off valve immediately it was possible to avoid the error induced by this leak.

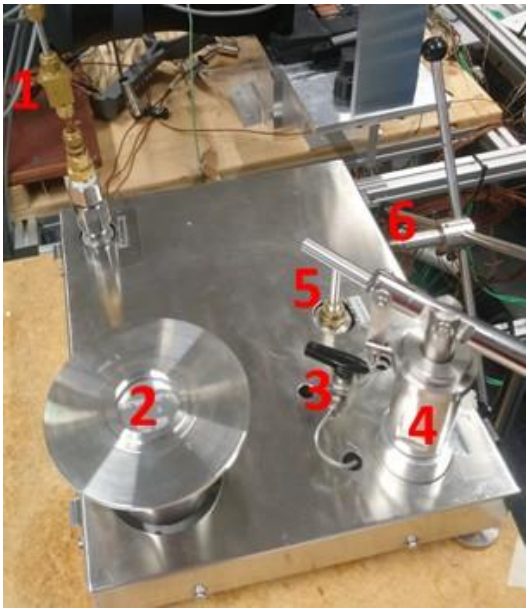

Figure 80 - Dead weight tester used for the pressure transducer calibration: 1. Cut-off valve between weight tester and pressure transducers. 2. Cylinder with 1 bar weight on top. 3. Bypass valve. 4. Priming pump.

9.2.1.2 Calibration procedure

After all leaks were fixed, a 1 bar-equivalent weight was placed on top of the cylinder. Following Figure 80, the procedure is hereby described. First, the cut-off valve (1) and the bypass valve (3) were opened, and the pressure was increased inside the system by using the priming pump (4). While this was done, the weight was kept spinning on the cylinder (2) to avoid friction losses. Once the weight was lifted (when the cylinder "jumped"), the bypass valve (3) was closed and the screw pump (6) rotated counter-clockwise to decrease the pressure. Once the weight came down again, the screw pump (6) was spun clockwise, slowly, while spinning the weight (2), following the procedure illustrated in Figure 81.

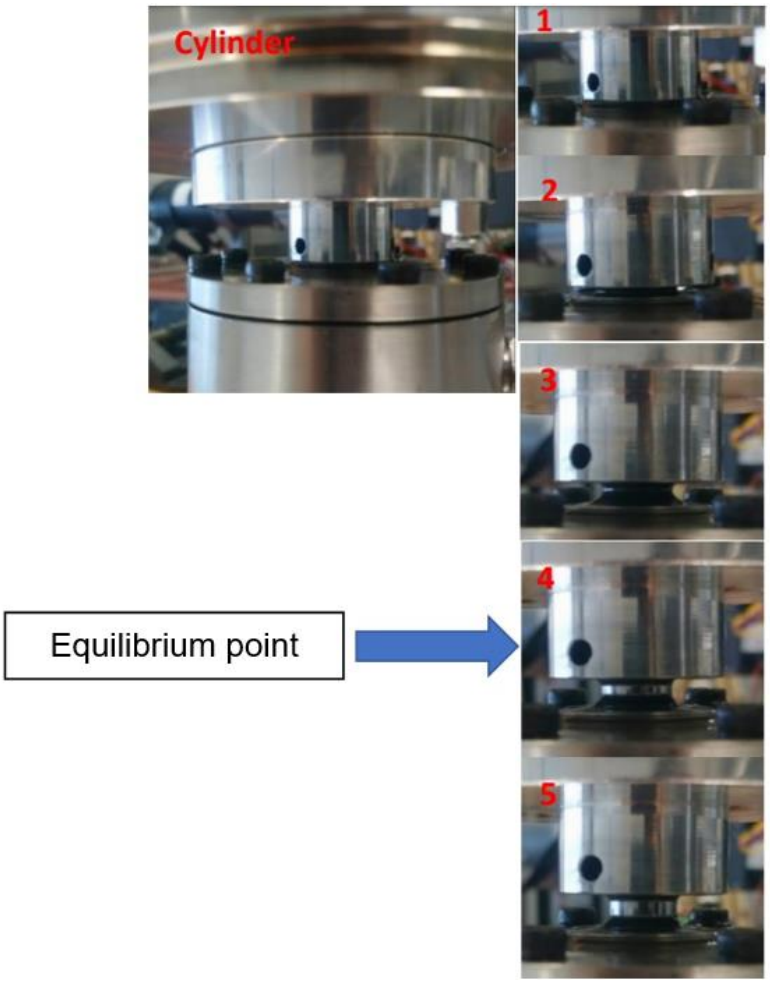

Figure 81 - Steps of weight detachment from the cylinder of the dead weight tester, following increasing pressure.

Figure 81 illustrates the determination of the equilibrium point at which the weights are suspended by the internal pressure of the system: 1. The weight is fully down; 2. The weight starts to detach; 3. The weight detaches but there's still a continuous film of oil; 4. The weight fully detaches and there's no longer influence of the oil's surface tension; 5. The piston reaches the top, and any further increases in pressure won't lift the weight further. As long as the piston did not reach the top, and there was no continuous oil film (4), the measured pressure was always the same.

When the situation in Figure 81 was reached, the cut-off valve was closed after at least 5 seconds, to allow for the weight and the pressure to stop oscillating. The cut-off valve was closed to ensure any leaks in the weight tester did not significantly influence the results. The signals were saved using the LabVIEW VI. This is ensured because the identified leak in the dead weight tester is in the cylinder interface, and therefore any eventual pressure drop caused by the movement of air from the inside of the dead weight tester to the atmosphere is mostly confined to the location between the internal base of the cylinder (where it is known that the air pressure balances the weight placed on top of the cylinder) and the external cylinder interface, and therefore there would not be any pressure gradient between the base of the cylinder and the pressure transducers.

Then, the LabVIEW VI saved the data (60 seconds), and the process was repeated for the next system pressure. After adding all the weights corresponding to the maximum pressure (usually 30

bar), the whole process was repeated for decreasing pressures until no more weights were left on the cylinder.

9.2.2 Post-processing

In order to post-process the results, a MATLAB post-processing script was developed. Besides showing the plots with the calibrations themselves, its main output is a file that contains the slopes, intercepts, and slope and intercept uncertainties. The script calculates the actual pressure measured, for each point:

$$P = P_{weights} + P_{atm} + P_{cylinder} \tag{25}$$

The weights' equivalent pressure is known, and the atmospheric pressure measured and saved in the files. $P_{cylinder}$ is the pressure resulting from the weight of the cylinder itself, which corresponds to 0.2 bar. For each number of weights placed on the cylinder, the LabVIEW VI saved the pressure transducers' output signal. The measured signal for each of the transducers was averaged for each pressure tested using the post-processing script, resulting in an array with the average values of the output signals of each transducer.

The final output was, for each transducer, the average output signals for each corresponding pressure. For each transducer, using a least-squares approximation, a linear regression was done for the pressure as a function of the measured transducer output signal, as explained in *Appendix C - Least squares approximation*.

At the same time, the uncertainties associated with the calibration were estimated (*Appendix D - Uncertainty propagation in least squares approximation*). The dead weight tester has an accuracy of 0.015% of each measurement [21]. In addition, the Testo T480 probe (for the atmospheric pressure measurement) has an accuracy of 3 hPa (0.003 bar). This means that the accuracy of each pressure (y_i) measurement was:

$$\varepsilon_{y_i}^2 = \varepsilon_{YANTRIKA,\%}^2 * y_i^2 + \varepsilon_{T480}^2 = 0.00015^2 y_i^2 + 0.003^2 \tag{26}$$

The Keller PA-33X pressure transducers [22] have an accuracy of 0.02% (accounting only for pressure measurement linearity, repeatability and hysteresis, not including temperature effects) and a further 0.05% must be added because of the signal conversion. This makes a total of 0.07%, which corresponds to $\pm$0.035%. For an output of 0-10 V, the accuracy of the transducers (x_i) is within 0.0035 V.

9.2.3 Results

Several calibrations were done, with differing power supplies, voltages and channel orders, in order to assess their influence on the results. The maximum acceptable difference for two calibrations,

as calculated by the uncertainty propagation, is around 0.015-0.02 bar (1.5-2 kPa) for 20 bar transducers and 0.03-0.04 bar (3-4 kPa) for 50 bar transducers. These values are consistent with the accuracy considered in previous tests (1.5 kPa) [6]. This error is, however, underestimated, because it does not take into account temperature effects or loss of accuracy with time (which can imply a further 0.01-0.02 bar of error). The uncertainty in the output voltage that was considered only takes into account hysteresis, non-linearity and non-repeatability, and its value is 0.02% of the total range (0.02%FS). However, the total error cited by the manufacturer is 0.1%, and this includes both the hysteresis/non-linearity/non-repeatability, but also errors due to temperature changes; furthermore, the long-term drift corresponds to an extra 0.1%FS of error [22]. Therefore, the total uncertainty, assuming a wide range of temperatures and that the transducers are several years old, can be estimated as 0.1%+0.1%+0.05% = 0.25%FS, or ±0.125%FS (a further 0.05%FS were added due to the signal conversion). This compares with the ±0.035%FS used for the calculations in Section 9.2.2. The reason why this smaller error was used in the calculations was to have more demanding tolerance criteria during troubleshooting, and also because the calibrations were all performed at similar temperatures.

No influence of significance was found, except for a case where the system was connected only to a particular DAQ module, which would result in a very significant difference. Upon investigation, it was concluded that his was caused by a grounding problem in that particular module, which was easily corrected by ensuring contact of the system to another DAQ module. The data points from all the valid calibrations were combined, in order to do a linear regression including data from all calibrations.

For the whole data, a plot of the pressure as a function of the voltage output of a pressure transducer is shown in Figure 82. The results of the linear regression including all measured data points are shown in Table 8.

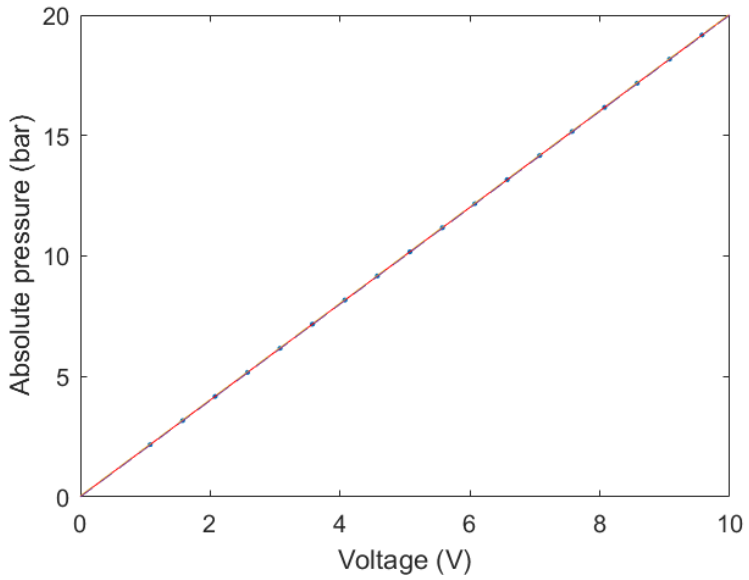

Figure 82 - Linear regression results for one of the pressure transducers.

Table 8 - Linear regression coefficients for all the pressure transducers.

Transducer	a (slope)	b (intercept)	ε_a	ε_b
PA	5.003	0.016	0.005	0.008
PB	2.000	0.008	0.001	0.003
PC	2.001	0.008	0.001	0.003
PD	2.001	0.004	0.001	0.003
PE	2.000	0.002	0.001	0.003
PF	2.000	0.027	0.001	0.003
PG	5.003	0.025	0.004	0.007
PH	1.999	0.007	0.001	0.003
PI	5.003	0.030	0.005	0.008
PJ	2.001	0.021	0.001	0.004
PK	1.999	0.048	0.001	0.004

9.3 Appendix C - Least squares approximation

For each transducer, using a least-squares approximation, a linear regression was done for the pressure as a function of the measured transducer output signal.

The result is a linear polynomial, which approximates the relation between the measured signal and the calibration:

$$y = ax + b \tag{27}$$

where y_i are the pressure values and x_i are the measured signals of the pressure transducer. The parameters a and *b* are given by:

$$a = \frac{\sum x_i y_i - n\bar{x}\bar{y}}{\sum x_i^2 - n\bar{x}^2} \tag{28}$$

$$b = \bar{y} - a\bar{x} \tag{29}$$

where $\bar{x}$ and $\bar{y}$ are the average values of all measured signals and pressures, respectively.

9.4 Appendix D - Uncertainty propagation in least squares approximation

The uncertainty associated with the slope *a* is:

$$\varepsilon_a^2 = \sum \left(\frac{\partial a}{\partial x_i}\right)^2 \varepsilon_{x_i}^2 + \sum \left(\frac{\partial a}{\partial y_i}\right)^2 \varepsilon_{y_i}^2 \tag{30}$$

where ε_{x_i} and ε_{y_i} are the uncertainties associated to each measured signal and each pressure.

The coefficient *a* is given by (*Appendix C - Least squares approximation*):

$$a = \frac{\sum x_i y_i - n\bar{x}\bar{y}}{\sum x_i^2 - n\bar{x}^2} = \frac{\sum x_i y_i - \frac{1}{n}\sum x_i \sum y_i}{\sum x_i^2 - \frac{1}{n}(\sum x_i)^2} \tag{31}$$

Differentiating with respect to each measured x_i:

$$\frac{\partial a}{\partial x_i} = \frac{\left(y_i - \frac{1}{n}\sum y_i\right)\left(\sum x_i^2 - \frac{1}{n}(\sum x_i)^2\right) - \left(2x_i - \frac{1}{n} * 2\sum x_i\right)\left(\sum x_i y_i - \frac{1}{n}\sum x_i \sum y_i\right)}{\left(\sum x_i^2 - \frac{1}{n}(\sum x_i)^2\right)^2} \tag{32}$$

$$\Leftrightarrow \frac{\partial a}{\partial x_i} = \frac{(y_i - \bar{y})(SS - n\bar{x}^2) - 2(x_i - \bar{x})(SC - n\bar{x}\bar{y})}{(SS - n\bar{x}^2)^2} \tag{33}$$

With SC and SS defined as:

$$SS = \sum x_i^2 \tag{34}$$

$$SC = \sum x_i y_i \tag{35}$$

Differentiating with respect to y_i:

$$\frac{\partial a}{\partial y_i} = \frac{x_i - \frac{1}{n}\sum x_i}{\sum x_i^2 - \frac{1}{n}(\sum x_i)^2} = \frac{x_i - \bar{x}}{SS - n\bar{x}^2} \tag{36}$$

The uncertainty associated with the slope can now be calculated by:

$$\varepsilon_a^2 = \sum \left(\frac{(y_i - \bar{y})(SS - n\bar{x}^2) - 2(x_i - \bar{x})(SC - n\bar{x}\bar{y})}{(SS - n\bar{x}^2)^2}\right)^2 \varepsilon_{x_i}^2 + \sum \left(\frac{x_i - \bar{x}}{SS - n\bar{x}^2}\right)^2 \varepsilon_{y_i}^2 \tag{37}$$

The intercept *b* is given by:

$$b = \bar{y} - a\bar{x} = \frac{1}{n}\sum y_i - \frac{a}{n}\sum x_i \tag{38}$$

The uncertainty associated with the intercept *b* is given by:

$$\varepsilon_b^2 = \sum \left(\frac{\partial b}{\partial x_i}\right)^2 \varepsilon_{x_i}^2 + \sum \left(\frac{\partial b}{\partial y_i}\right)^2 \varepsilon_{y_i}^2 + \left(\frac{\partial b}{\partial a}\right)^2 \varepsilon_a^2 \tag{39}$$

$$\frac{\partial b}{\partial x_i} = -\frac{a}{n} \tag{40}$$

$$\frac{\partial b}{\partial y_i} = \frac{1}{n} \tag{41}$$

Finally, having both ε_b and ε_a:

$$\varepsilon_b^2 = \frac{a^2}{n^2}\sum \varepsilon_{x_i}^2 + \frac{1}{n^2}\sum \varepsilon_{y_i}^2 + \frac{1}{n^2}\left(\sum x_i\right)^2 \varepsilon_a^2 = \frac{a^2}{n}\varepsilon_{x_i}^2 + \frac{1}{n^2}\sum \varepsilon_{y_i}^2 + \bar{x}^2\varepsilon_a^2\,, \tag{42}$$

the overall uncertainty for the estimated pressure, *y*, corresponding to the measured voltage x_i is:

$$\varepsilon_y^2 = \left(\frac{\partial y}{\partial x_i}\right)^2 \varepsilon_{x_i}^2 + \left(\frac{\partial y}{\partial a}\right)^2 \varepsilon_a^2 + \left(\frac{\partial y}{\partial b}\right)^2 \varepsilon_b^2 = a^2\varepsilon_{x_i}^2 + x_i^2\varepsilon_a^2 + \varepsilon_b^2 \tag{43}$$

9.5 Appendix E – Charges and filling ratios

The measured charges and corresponding filling ratios, for all the tests, are listed in Table 9.

Table 9 - Measured charges and corresponding filling ratios for each performed test.

Working fluid	Test	Mass (g)	FR (%)
R1233zd(E)	FR Analysis 1	33.68	30
		46.22	41
		56.90	50
		70.68	62
		80.98	71
		91.75	81
	FR Analysis 2	33.18	29
		45.23	40
		57.66	51
		67.89	60
		80.38	71
	Test at 46% FR	52.29	46
	Test at 41% FR	46.47	41
R1234ze(E)	FR Analysis	42.35	41
		52.21	50
		62.96	60
		73.31	70
		83.82	80
	Test at 51%	53.79	51